SUPER-CONFORMAL COATING AND FILLING OF HIGH ASPECT RATIO RECESSED STRUCTURES BY TWO-MOLECULE CVD

BY

WENJIAO WANG

DISSERTATION

Submitted in partial fulfillment of the requirements
for the degree of Doctor of Philosophy in Materials Science and Engineering
in the Graduate College of the
University of Illinois at Urbana-Champaign, 2014

Urbana, Illinois

Doctoral Committee:

Professor John R. Abelson, Chair
Professor Gregory S. Girolami
Professor J. Gary Eden
Professor Paul V. Braun
Professor Lane W. Martin

ABSTRACT

Complete filling of a deep recessed structure with a second material is a challenge in many areas of nanotechnology fabrication, including MEMS devices, metallization and shallow trench isolation (STI) in integrated circuits. For structures with straight sidewalls, uniform coating methods – including chemical vapor deposition (CVD) or atomic layer deposition (ALD) – typically form a void or region of low density (seam) along the centerline of the feature because the transport of precursor molecules to the bottom becomes rate limiting. These defects undermine device properties and methods are needed to afford complete filling. One approach is to taper the two sidewalls slightly inwards. However, the requirement for tapering is an undesirable constraint both for device design and fabrication. A more general approach is to develop a process for superconformal film growth, in which the growth rate increases with depth. Previously, only specialized processes, including iodine catalyzed Cu growth or high-density plasma CVD, have provided super-conformal coating and complete filling.

In this dissertation, I report a newly discovered and general method to achieve super-conformal coating suitable for two-molecule CVD at low temperatures, which makes use of the difference in diffusivities in combination with the competition for surface adsorption sites between the molecules involved. The partial pressures above the opening are set such that the slower diffusing species is in excess, which reduces the growth rate below the peak value. Within the structure, film growth on the sidewalls

reduces the partial pressures; the pressure drop is greater for the slower diffusing species, such that the ratio of partial pressures progressively shifts towards a larger growth rate. However, the position at which the peak rate occurs must not be above the bottom of the structure, otherwise the growth rate will fall at greater depths, leading to incomplete filling.

We demonstrate and quantify the superconformal coating effect for the CVD of MgO films using $Mg(DMADB)_2$ as the precursor and H_2O as the co-reactant at 220 °C. The growth kinetics on planar substrates fit to a first-order adsorption-reaction model. We use a diffusion-reaction formalism to derive a general theory of superconformal growth as a function of AR, species diffusivities, and variation of growth rate vs. partial pressures. The theory predicts, for the MgO system, the possibility of superconformal growth in trenches with AR $\leq$ 20. We demonstrate the effect experimentally for a macroscopic trench with AR = 18, and for a microscopic trench of AR = 9. We also identify other systems that are promising candidates for superconformal growth.

Filling is a dynamic process where the trench progressively narrows with depth; this reduces species transport and may eventually move the partial pressure ratio out of the regime for superconformal coating. We therefore derive two theoretical models that can model and predict the possibility for filling in a V-shaped structure. First, we recast the diffusion-reaction equation for the case of a sidewall with variable taper angle. This affords a definition of effective AR, which is larger than the nominal AR due to the reduced species transport. This model shows that the critical (most difficult) step in the filling process occurs when the sidewalls merge at the bottom to form the V shape trench.

For $Mg(DMADB)_2$ / H_2O system and a starting AR = 9, this model predicts that complete filling will *not* be possible, whereas experimentally we *do* obtain complete filling. We then hypothesize that glancing-angle, long-range transport of species may be responsible for the better than predicted filling. To account for the variable range of species transport, we construct a ballistic transport and reaction model. This incorporates the incident flux from outside the structure, cosine law re-emission from surfaces, and line-of-sight transport between internal surfaces. We cast the transport probability between all positions into a matrix that represents the redistribution of flux after one cycle of collisions. Matrix manipulation then affords a computationally efficient means to determine the steady-state flux distribution and growth rate for a given taper angle. The ballistic transport model predicts a deeper position for the peak of the super-conformal growth rate than the diffusion-reaction model, and successfully explains the observation of complete filling. These models can be used to predict the behavior of any system given a small set of kinetic coefficients to describe the growth rate.

This dissertation also reports the growth of a variety of oxide thin films on planar substrates using DMADB-based precursors, synthesized by Professor G. S. Girolami, which contain Ti or rare earth (RE) metal centers. Similar to the results for $Mg(DMADB)_2$, these precursors react with water to yield high quality oxide films. $Ti(DMADB)_2$ affords mixed-phase TiO_2 film of high purity at 350 - 450 °C. Y_2O_3 film containing ~ 4 at. % boron is deposited on Si (100) substrates at 230 - 300 °C. Erbium oxide does not nucleate well on silicon, but deposits well over pre-deposited MgO. RE doping, which is important for the fabrication of devices based on luminescence, is

investigated. In-situ Tm doping into MgO and Er doping into Y_2O_3 are achieved. In addition, we explore the use of the $Mg(DMADB)_2$ precursor for film growth in ALD mode with H_2O as the co-reactant. We determine that ALD can be performed in the temperature window 165-210 °C, with a higher growth rate per cycle than has been reported for any other Mg-bearing precursor.

To Parents and Wife

ACKNOWLEDGEMENT

I would like to extend my greatest and sincere appreciation to my advisor John R. Abelson, for his patience, kindness, and thoughtful guidance throughout my doctoral study. This piece of work is not possible without his constant support during the years. I also need to thank Gregory S. Girolami, for in-depth discussions about experiments, his critical thinking, and his efforts in the improvement of manuscripts. Besides, I thank all my other thesis committee members, J. Gary Eden, Paul V. Braun, and Lane W. Martin, for all your insightful comments and encouragement in my research.

I appreciate all my co-workers, lab mates, and staff members in MRL for their assistance in my research, especially:

- Noel N. Chang, Tracey A. Codding and Brian Trinh's synthesis or loading of precursor molecules for my research
- Pengyi Zhang, Shaista Barber, and Tony Li's help in sample analysis with Auger, SEM, AFM, and TEM; Kristof Darmawikarta's assistance in repairing the right chamber
- Angel Yanguas-Gil, Navneet Kumar, Andy Cloud, Teresa Spicer, Bong-Sub Lee, Elham Mohimi, and Tushar K. Talukdar's discussions about projects
- Rick Haasch, Scott MacLaren, Julio A. Soares, Mauro Sardela, Vania Petrov, and Jeffers A. Douglas's tutoring and assistance in sample analysis in XPS, AFM, VASE and photoluminescence, XRD, SEM and RBS.

Of course, my great thanks also go to my family, whose love and support is indispensable, especially at difficult times. This work is in memory of my father, who raised and took care of me with his whole life.

This work is supported by National Science Foundation under grants DMR-1005715 and 1410209. *Ex situ* materials characterization was carried out in part in the Frederick Seitz Materials Research Laboratory Central Facilities, University of Illinois.

TABLE OF CONTENTS

CHAPTER 1: INTRODUCTION 1

1.1 Motivation – Complete Filling in Straight Wall Structures 1
1.1.1 Integrated Circuits 1
1.1.2 MEMS Devices 2

1.2 Overview of Filling Methods 3
1.2.1 Analysis of Filling Challenge 3
1.2.2 A Promising Method: Super-conformal Coating 4
1.2.3 Reported Filling Methods 5

1.3 Novel Precursors with DMADB Ligand 6

1.4 Reaction System 7

1.5 References 9

1.6 Figures 13

CHAPTER 2: SUPER-CONFORMAL CVD OF THIN FILMS IN DEEP FEATURES 14

2.1 Introduction 14
2.1.1 Background 14
2.1.2 Approach 15

2.2 Experiment 17

2.3 Growth Results 18

2.4 Model 19
2.4.1 General Reaction Kinetics for Two-molecule CVD 20
2.4.2 Diffusivities and Pressure Drop Relationship 23
2.4.3 Prediction of Conformality 25

2.5 Analysis and Discussion 27
2.5.1 Effect of Wall Adsorption on the Diffusivity 27
2.5.2 Relationship between GR, AR, SC 28

2.6 Summary 32

2.7 Appendix 33

2.8 References 34

2.9 Tables and Figures 37

CHAPTER 3: CRITICAL CONDITION FOR FILLING: SUPER-CONFORMAL COATING TO AFFORD TAPERED SIDEWALLS 43

3.1 Introduction 43

3.2 Model Assumptions 45

3.3 Diffusion-reaction Model 47
3.3.1 Model Description 47
3.3.2 Analysis of Critical Condition for Filling 51
3.3.3 Diffusion-reaction Model of Filling 52

3.4 Ballistic Transport 53
3.4.1 Model Description 54
3.4.2 Direct Flux 54
3.4.3 Re-emitted Flux 56
3.4.4 Matrix Notation and Calculation for Steady-state Distribution 57
3.4.5 Constant Sticking Probability Case 58

3.5 Comparison Between the Diffusion and Ballistic Models 59
3.5.1 For a Constant Sticking Probability 59
3.5.2 For Super-conformal Coating Conditions 60

3.6 Conclusions 63

3.7 References 64

3.8 Figures 67

CHAPTER 4: RE OXIDE CVD WITH RE(DMADB)$_3$ PRECURSORS AND WATER 77

4.1 Introduction 77

4.2 Experiment 78

4.3 Result and Discussion 79
4.3.1 Growth Kinetics 79
4.3.2 Film Morphology 79
4.3.3 Film Composition 80
4.3.4 RE Doping 80

4.4 Conclusion 81

4.5 References 82

4.6 Figures 87

CHAPTER 5: CVD OF TiO_2 THIN FILMS AT LOW-TEMPERATURE FROM $Ti(DMADB)_2$ AND WATER 90

5.1 Introduction 90

5.2 Experiment 91

5.3 Results and Discussion 92
5.3.1 Composition 92
5.3.2 Growth Kinetics 93
5.3.3 Microstructure and Crystallinity 93

5.4 Conclusion 94

5.5 References 95

5.6 Tables and Figures 99

CHAPTER 6: ATOMIC LAYER DEPOSITION OF MgO WITH $Mg(DMADB)_2$ AND H_2O 104

6.1 Introduction 104

6.2 Experiment 105

6.3 Result and Discussion 107
6.3.1 Growth Kinetics 107
6.3.2 Film Properties 108

6.4 Conclusion 109

6.5 References 110

6.6 Figures 113

CHAPTER 1

INTRODUCTION

1.1 Motivation – Complete Filling in Straight Wall Structures

As the manufacturing technology has improved to nanometer size, an increasing number of applications requires filling of desired material into pre-defined structures of this dimension. Interesting and useful properties of nanoscale devices often arise when two or more materials with contrasting physical properties are arranged in a 3-dimensional structure that enhances the optical, electronic, mechanical or thermal response [1]. For example, infiltration of a second material into SiO_2 opal structures is able to form complete photonic crystals, and strong photoluminescence is achieved when doped with luminescent centers during filling [2,3]; inside trench, waveguide made of alternating deposition of two kinds of material with different refractive indices till complete filling allows the fine tuning of the refractive index of the whole device [4]. To achieve filling for nanometer size structures, conformal gas phase coating techniques, like Chemical Vapor Deposition (CVD) or Atomic Layer Deposition (ALD) are typically applied, due to the much lower sticking probability compared with Physical Vapor Deposition (PVD) [5,6]. However, filling is still a challenge for high aspect ratio (AR) structures.

1.1.1 Integrated Circuits

Microelectronic devices have continuously been reduced in size and increased in packing density on the chip, essentially following Moore's Law. However, this trend

involves significant challenges in materials fabrication. To achieve a higher packing density, the aspect ratio (AR) of structures must be increased; uniform coating and complete filling are difficult to achieve in such deep structures. Leading examples include Cu metallization and shallow trench isolation [7]. Filling defects include trapped void space or the formation of a low density “seam” along the centerline [8]. Alternating CVD and plasma etching has been employed to eliminate pinch off and achieve filling [9], but this method is only good for shallow ARs of 2 - 4 [10]. According to the ITRS roadmap, a process is needed for ARs approaching 20; complete filling with an oxide is cited as a “major challenge” [7].

1.1.2 MEMS Devices

High aspect-ratio combined poly and single-crystal silicon technology is widely applied in manufacturing MEMS devices; examples include the micro-gyroscope and the resonant beam strain gauge [11]. The shape of the devices is firstly patterned and defined by dry etching on a Si wafer; a sacrificial oxide layer is deposited; the remaining opening is then filled with poly-Si using CVD; finally the sacrificial oxide layer is etched away to retrieve the device by lift-off. The crucial step is the complete filling of poly-Si into a rectangular trench of AR ~20. There are reports for void space or seam forming inside, which undermines the mechanical and thermal transport properties of the device [12,13]. As one important energy dissipation mechanism, thermal transport greatly affects the quality factor of the device.

1.2 Overview of Filling Methods

1.2.1 Analysis of Filling Challenge

Filling of high aspect ratio recessed features is difficult because the internal surface area is very large compared to the area of the opening, and because transport is limited by molecular diffusion. As the precursor moves down the axis of a recessed feature, it is continuously consumed by reaction on the walls. When the deposition rate is proportional to the local partial pressure of precursor, as is usually the case with CVD, the film thickness is greatest near the opening and tapers to a small or zero value at depth. Carried to completion under these conditions, the opening ultimately closes (pinches) off, leaving an unfilled void underneath.

This outcome can be partially mitigated if the deposition is carried out under conditions of very low surface reaction rate with respect to the transport rate. This regime is routinely achieved using atomic layer deposition (ALD) or chemical vapor deposition (CVD) in the limit of saturated growth rate; under these conditions the drop in precursor pressure inside the feature is minimized and has almost no effect on the resulting film growth rate or thickness [14].

However, perfect filling is generally not achieved by these approaches. In features that have complex shapes, or in which the feature width increases with depth, even perfectly conformal growth cannot eliminate the formation of a void below the pinched-off opening. Such shapes are a common, but not inevitable, result of reactive ion etching or particle assembly processes [12]. In addition, even in features that have parallel walls, conformality tends to degrade as filling proceeds. As coatings build up on the opposite

sides of the feature, the remaining width becomes narrower and narrower; eventually the AR becomes extremely large and the transport rate of the precursor shrinks to tiny values. To preserve conformal conditions in CVD, the growth rate must be reduced to a very low value [14]. The result can be near to complete filling, but a 'seam' of low-density material invariably remains along the centerline of the feature. This seam is undesirable or unacceptable in many applications because it leads to a degradation of performance, including thermal or mechanical properties [12,13] or electrical conductivity [15-17].

1.2.2 A Promising Method: Super-conformal Coating

A different result holds when the feature width decreases steadily with depth, which we will refer to as a 'V' shape. In this case, highly conformal coating produces high quality filling: as the deposit on the walls thickens, the angle at the bottom of the V remains constant and the position of the bottom point moves progressively toward the opening. The crucial role of the V shape has been described previously [4,18]. However, it is undesirable (and potentially infeasible) to limit the design of nanoscale devices to structures in which all the features have a pre-existing V shape. For example, the MEMS devices requires the angle of the sidewall to be $90 \pm 1°$ [11]. We will show quantitatively in Chapter 3 that neither conformal CVD nor ALD can fill high AR features with such a slight taper.

To achieve robust filling in the largest variety of features, it has long been a goal to develop super-conformal growth processes in which the film deposition rate is larger at the bottom of the feature than it is near the opening. Such a process will establish a V shape and slowly enlarge the bottom angle such that seam formation is eliminated.

Note that super-conformal growth may not be required for the entire duration of a filling process: it can suffice to establish an inward-inclined sidewall shape of the feature, then change to growth conditions that are highly conformal [19,20]. Such a procedure will reduce the process time if the deposition rate is higher using the conditions for conformal coating [20].

1.2.3 Reported Filling Methods

At least four methods have been employed to achieve filling of high aspect ratio features. We summarize these methods to provide a basis for comparison.

(i) Superfill: In the CVD of copper and manganese, the growth rate can be enhanced using a pre-deposited catalyst (iodine), which remains segregated on the film surface [21-23]. As deposition proceeds, the concave regions lose surface area and the concentration of catalyst increases at the bottom of the feature, thus increasing the growth rate there relative to the feature sidewalls.

(ii) Electrodeposition: Liquid phase additives, which can serve either to inhibit growth near the feature opening or enhance growth at greater depths, have been demonstrated. The 'curvature enhanced accelerator coverage' method [24] has been developed for Cu, Au [25], Ag [26], Co and Co-Fe [1] and applied for Cu metallization [27,28].

(iii) High density plasma CVD: Features can be filled using a competitive process of film deposition and plasma etching [9]. For example, high density plasma chemical vapor deposition [10] is suitable for aspect ratios of ~ 2-4.

(iv) Atomic Layer Deposition: ALD can be used to fill or partially fill structures via highly conformal coating. Reports of nominally complete filling include SiO_2 / Al_2O_3 nanolaminates in vias [29] with *AR* = 35 and in trenches [30] with *AR* = 12-14; TiO_2 in V-shaped Si slot waveguides [4]; and Al_2O_3 in multiwall C nanotubes [31]. Reports of incomplete filling include TiO_2 [32] or GaP [33] in opal templates with *AR* ~ 4000 using pulsed gas injection, and Al_2O_3 filling in via with AR of 10 [34].

We report in this dissertation a new method to afford super-conformal coating in CVD using two molecular reactants at relatively low temperatures (Chapter 2). This method can transform a high AR structure that originally has straight sidewalls into one with taped walls, called a V-shape. We also report two theoretical approaches that can predict the conditions under which the V-shape can be completely filled without the formation of a void or seam (Chapter 3). An important new concept is that of effective AR, which is higher than the nominal AR due to the nature of diffusive transport in a tapered structure.

1.3 Novel Precursors with DMADB Ligand

A modified borohydride ligand, N, N-dimethylaminodiboranate (DMADB), has been invented by Prof. G. S. Girolami and his group. Using this ligand, they synthesized a series of new CVD precursors of the form $M(DMADB)_x$, where M stands for the metal center. These include Mg [35], Ti, Y, and the whole series of lanthanide elements, except Eu and Yb [36]. The chemical structure of this group of precursors is similar to that of $Mg(DMADB)_2$ (Fig. 1.1). The $Mg(DMADB)_2$ precursor has an exceptionally high room temperature vapor pressure (0.8 Torr, the highest for any reported Mg-bearing molecule)

and exhibits a clean reaction pathway with H_2O to afford MgO film and liberate H(DMADB) products [37]. It is reasonable to expect that other precursors with the same ligand, including $Ti(DMADB)_2$, $Y(DMADB)_3$ and other $Ln(DMADB)_3$, would behave similarly, and that oxide host doping with rare earth elements should be straightforward [38]. We have evaluated and report the CVD behavior of selected members of this group to afford oxide materials (Chapter 4).

TiO_2 is an important oxide material due to its photocatalytic properties [39], and dielectric constant [40,41]. We report an initial set of film growth experiments (Chapter 5).

Due to the favorable properties of the Mg(DMADB)2 precursor, we also investigate its behavior in the ALD of MgO, and report preliminary results (Chapter 6).

1.4 Reaction System

All films in this work, except for TiO_2, are deposited with a thermal CVD system equipped with in-situ spectroscopic ellipsometry (SE) (J. A. Woollam M-88). This system has been described in Brent A. Sperling's Ph.D. dissertation for hot-wire CVD [42]. Minor changes have been made to render the system suitable for thermal CVD (Fig. 1.2). Two sets of parallel tubes are used to inject the precursor and co-reactant (water). One set points towards the chamber walls, so that the molecules experience multiple reflections before they reach the substrate; under these conditions the partial pressures above the substrate are equal to the average values measured by the capacitance manometer elsewhere on the chamber. This set of inlets are used for MgO CVD, for which both molecules have high vapor pressures and accurate pressure values are needed

to evaluate the growth kinetics. The other set is 7 cm away from, and perpendicular to the substrate, in order to concentrate the molecule fluxes onto the growth surface. This set of inlets is used for RE oxide growth and doping due to the lower vapor pressures of those molecules. SE is used to measure the film thickness during growth, based on Cauchy optical models for different films. TiO_2 growth is performed in the two-chamber system, previously described in the Ph.D. dissertation of Navneet Kumar [43]. Ex-situ sample analyses of morphology, composition, crystallinity, and optical properties are done in the Center for Microanalysis of Materials, Material Research Laboratory at UI.

1.5 References

1. H. Kim, H. B. R. Lee, and W. J. Maeng, "Applications of atomic layer deposition to nanofabrication and emerging nanodevices", *Thin Solid Films* **517,** 2563-80 (2009).

2. J. S. King, C. W. Neff, C. J. Summers, W. Park, S. Blomquist, E. Forsythe, and D. Morton, "High-filling-fraction inverted ZnS opals fabricated by atomic layer deposition", *Applied Physics Letters* **83,** 2566-8 (2003).

3. A. Stein and R. C. Schroden, "Colloidal crystal templating of three-dimensionally ordered macroporous solids: materials for photonics and beyond", *Current Opinion in Solid State & Materials Science* **5,** 553-64 (2001).

4. A. Säynätjoki, T. Alasaarela, A. Khanna, L. Karvonen, P. Stenberg, M. Kuittinen, A. Tervonen, and S. Honkanen, "Angled sidewalls in silicon slot waveguides: conformal filling and mode properties", *Opt. Express* **17,** 21066-76 (2009).

5. M. Ohring, *Materials Science of Thin Films*, 2nd ed. (Academic Press, 2002).

6. J. E. Crowell, "Chemical methods of thin film deposition: Chemical vapor deposition, atomic layer deposition, and related technologies", *Journal of Vacuum Science & Technology A* **21,** S88-S95 (2003).

7. *International Technology Roadmap for Semiconductors* (2009).

8. B. Kim, C. Sharbono, T. Ritzdorf, and D. Schmauch, "Factors affecting copper filling process within high aspect ratio deep vias for 3D chip stacking," 2006, p. 6 pp.

9. D. R. Cote, S. V. Nguyen, A. K. Stamper, D. S. Armbrust, D. Tobben, R. A. Conti, and G. Y. Lee, "Plasma-assisted chemical vapor deposition of dielectric thin films for ULSI semiconductor circuits", *IBM J. Res. Dev.* **43,** 5-38 (1999).

10. H. Nishimura, S. Takagi, M. Fujino, and N. Nishi, "Gap-fill process of shallow trench isolation for 0.13 mu m technologies", *Japanese Journal of Applied Physics Part 1-Regular Papers Short Notes & Review Papers* **41,** 2886-93 (2002).

11. F. Ayazi and K. Najafi, "High aspect-ratio combined poly and single-crystal silicon (HARPSS) MEMS technology", *Journal of Microelectromechanical Systems* **9,** 288-94 (2000).

12. R. Abdolvand, H. Johari, G. K. Ho, A. Erbil, and F. Ayazi, "Quality factor in trench-refilled polysilicon beam resonators", *Journal of Microelectromechanical Systems* **15,** 471-8 (2006).

13. H. Schenk, P. Durr, D. Kunze, H. Lakner, and H. Kuck, "A resonantly excited 2D-micro-scanning-mirror with large deflection", *Sensors and Actuators a-Physical* **89,** 104-11 (2001).

14. A. Yanguas-Gil, Y. Yang, N. Kumar, and J. R. Abelson, "Highly conformal film growth by chemical vapor deposition. I. A conformal zone diagram based on kinetics", *Journal of Vacuum Science & Technology A* **27,** 1235-43 (2009).

15. C. C. Chen, I. C. Kao, H. C. Kuo, and H. J. Chien, "Studying of physical characteristics and optimizing of gap filling for tungsten", *Mater. Sci. Semicond. Process* **14,** 235-40 (2011).

16. A. Kubo, T. Homma, and Y. Murao, "An SiO_2 film deposition technology using tetraethylorthosilicate and ozone for interlayer metal dielectrics", *Journal of the Electrochemical Society* **143,** 1769-73 (1996).

17. X. F. Lin, X. Ma, and J. J. He, "Void-filling and loss reduction in PECVD silica waveguide devices using boron-germanium codoped upper cladding", *IEEE Photonics Technol. Lett.* **22,** 1491-3 (2010).

18. J. H. Yun and S. K. Park, "Theoretical-study of step coverage and comparison with experimental results from low-pressure chemical-vapor-deposition process of tungsten film", *Japanese Journal of Applied Physics Part 1-Regular Papers Short Notes & Review Papers* **34,** 3216-26 (1995).

19. C. H. Lee, J. E. Bonevich, J. E. Davies, and T. P. Moffat, "Superconformal electrodeposition of Co and Co-Fe alloys using 2-mercapto-5-benzimidazolesulfonic acid", *Journal of the Electrochemical Society* **156,** D301-D9 (2009).

20. Y. Yang, Thesis, University of Illinois at Urbana-Champaign, 2007.

21. Y. Au, Y. B. Lin, and R. G. Gordon, "Filling narrow trenches by iodine-catalyzed cvd of copper and manganese on manganese nitride barrier/adhesion layers", *Journal of the Electrochemical Society* **158,** D248-D53 (2011).

22. S. G. Pyo, S. Kim, D. Wheeler, T. P. Moffat, and D. Josell, "Seam-free fabrication of submicrometer copper interconnects by iodine-catalyzed chemical vapor deposition", *J. Appl. Phys.* **93,** 1257-61 (2003).

23. D. Josell, S. Kim, D. Wheeler, T. P. Moffat, and S. G. Pyo, "Interconnect fabrication by superconformal iodine- catalyzed chemical vapor deposition of copper", *Journal of the Electrochemical Society* **150,** C368-C73 (2003).

24. T. P. Moffat, D. Wheeler, M. D. Edelstein, and D. Josell, "Superconformal film growth: Mechanism and quantification", *IBM J. Res. Dev.* **49,** 19-36 (2005).

25. D. Josell, D. Wheeler, and T. P. Moffat, "Gold superfill in submicrometer trenches: Experiment and prediction", *Journal of the Electrochemical Society* **153,** C11-C8 (2006).

26. D. Josell, C. Burkhard, Y. Li, Y. W. Cheng, R. R. Keller, C. A. Witt, D. R. Kelley, J. E. Bonevich, B. C. Baker, and T. P. Moffat, "Electrical properties of superfilled sub-micrometer silver metallizations", *J. Appl. Phys.* **96,** 759-68 (2004).

27. B. C. Baker, C. Witt, D. Wheeler, D. Josell, and T. P. Moffat, "Superconformal silver deposition using KSeCN derivatized substrates", *Electrochem. Solid State Lett.* **6,** C67-C9 (2003).

28. T. P. Moffat, J. E. Bonevich, W. H. Huber, A. Stanishevsky, D. R. Kelly, G. R. Stafford, and D. Josell, "Superconformal electrodeposition of copper in 500-90 nm features", *Journal of the Electrochemical Society* **147,** 4524-35 (2000).

29. D. Hausmann, J. Becker, S. L. Wang, and R. G. Gordon, "Rapid vapor deposition of highly conformal silica nanolaminates", *Science* **298,** 402-6 (2002).

30. J. J. Wang, X. G. Deng, R. Varghese, A. Nikolov, P. Sciortino, F. Liu, L. Chen, and X. M. Liu, "Filling high aspect-ratio nano-structures by atomic layer deposition and its applications in nano-optic devices and integrations", *Journal of Vacuum Science & Technology B* **23,** 3209-13 (2005).

31. J. S. Lee, B. Min, K. Cho, S. Kim, J. Park, Y. T. Lee, N. S. Kim, M. S. Lee, S. O. Park, and J. T. Moon, "Al_2O_3 nanotubes and nanorods fabricated by coating and filling of carbon nanotubes with atomic-layer deposition", *Journal of Crystal Growth* **254,** 443-8 (2003).

32. S. K. Karuturi, L. J. Liu, L. T. Su, Y. Zhao, H. J. Fan, X. C. Ge, S. L. He, and A. T. I. Yoong, "Kinetics of stop-flow atomic layer deposition for high aspect ratio template filling through photonic band gap measurements", *Journal of Physical Chemistry C* **114,** 14843-8 (2010).

33. E. Graugnard, V. Chawla, D. Lorang, and C. J. Summers, "High filling fraction gallium phosphide inverse opals by atomic layer deposition", *Applied Physics Letters* **89** (2006).

34. K.-K. Choi, J. Kee, S.-H. Kim, M.-S. Park, C.-G. Park, and D.-K. Kim, "Filling performance and electrical characteristics of Al_2O_3 films deposited by atomic layer deposition for through-silicon via applications", *Thin Solid Films* **556,** 560-5 (2014).

35. D. Y. Kim and G. S. Girolami, "Highly volatile magnesium complexes with the aminodiboranate anion, a new chelating borohydride. synthesis and characterization of $Mg(H_3BNMe_2BH_3)_2$ and Related Compounds", *Inorg. Chem.* **49,** 4942-8 (2010).

36. S. R. Daly, D. Y. Kim, and G. S. Girolami, "Lanthanide N,N-dimethylaminodiboranates as a new class of highly volatile chemical vapor deposition precursors", *Inorg. Chem.* **51,** 7050-65 (2012).

37. W. B. Wang, Y. Yang, A. Yanguas-Gil, N. N. Chang, G. S. Girolami, and J. R. Abelson, "Highly conformal magnesium oxide thin films by low-temperature chemical vapor deposition from $Mg(H_3BNMe_2BH_3)_2$ and water", *Applied Physics Letters* **102** (2013).

38. W. Chen, J. Z. Zhang, and A. G. Joly, "Optical properties and potential applications of doped semiconductor nanoparticles", *Journal of Nanoscience and Nanotechnology* **4,** 919-47 (2004).

39. A. Enesca, L. Andronic, A. Duta, and S. Manolache, "Optical properties and chemical stability of WO_3 and TiO_2 thin films photocatalysts", *Romanian Journal of Information Science and Technology* **10,** 269-77 (2007).

40. S. K. Kim, W. D. Kim, K. M. Kim, C. S. Hwang, and J. Jeong, "High dielectric constant TiO_2 thin films on a Ru electrode grown at 250 degrees C by atomic-layer deposition", *Appl. Phys. Lett.* **85,** 4112-4 (2004).

41. D. A. Deen, J. G. Champlain, and S. J. Koester, "Multilayer HfO_2/TiO_2 gate dielectric engineering of graphene field effect transistors", *Appl. Phys. Lett.* **103,** - (2013).

42. B. A. Sperling, Thesis, University of Illinois at Urbana-Champaign, 2006.

43. N. Kumar, Thesis, University of Illinois at Urbana-Champaign, 2009.

1.6 Figures

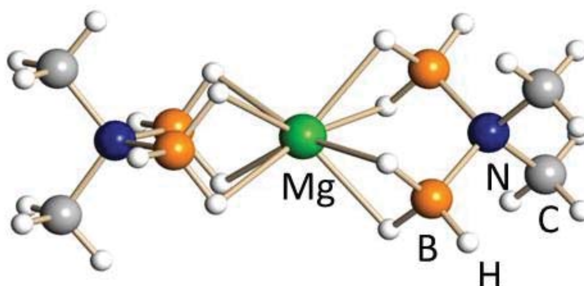

Figure 1.1. Molecular structure for $Mg(DMADB)_2$.

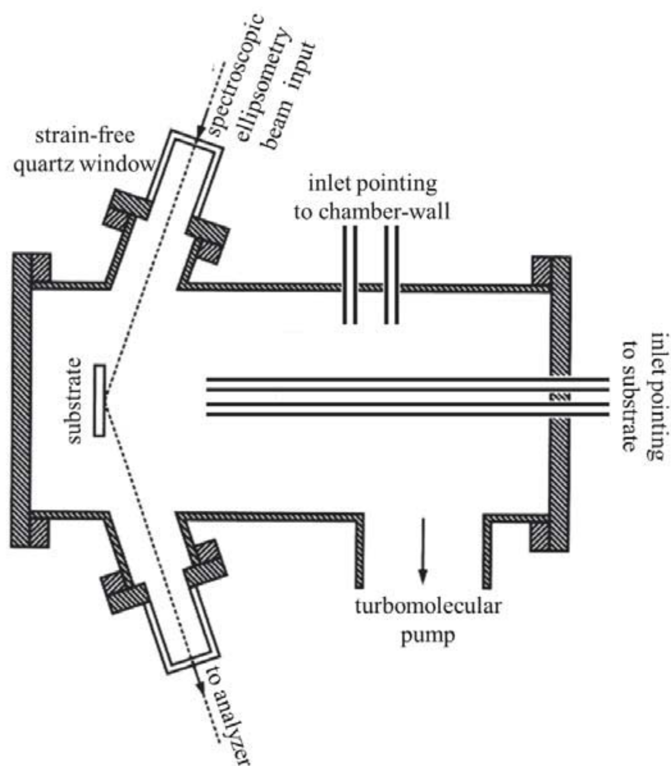

Figure 1.2. Schematic showing of the chamber structure and positions of inlet tubes. One pair of tubes point perpendicularly towards the substrate, used for CVD with precursors with low vapor pressures. The other pair point towards the chamber side-wall, used for high vapor pressure molecules.

CHAPTER 2

SUPER-CONFORMAL CVD OF THIN FILMS IN DEEP FEATURES

2.1 Introduction

2.1.1 Background

Interesting and useful properties of nanoscale devices often arise when two or more materials with contrasting physical properties are arranged in a 3-dimensional structure that enhances the optical, electronic, mechanical or thermal response [1]. Such structures can be fabricated by removing material in a patterned and directional manner [2], typically to create a high aspect ratio (AR) opening, and then to fill that feature with a desired material. This last method is a crucial capability for several important technologies: for example, the International Technology Roadmap for Semiconductors specifies filling as a key challenge for low-*k* dual damascene structures, shallow trench isolation, and DRAMs [3]. In addition, for MEMS device manufacturing, trenches must be completely filled [4,5] without internal voids [6].

The challenge and current methods for filling has been addressed in Chapter 1, and the key characteristic to achieve complete filling is super-conformal growth, that is, to have the film growth rate increase from feature opening to bottom. Below, I will introduce the newly discovered super-conformal coating based on two-molecule CVD process.

2.1.2 Approach

Our new method of super-conformal growth in two-molecule CVD is based on the theory of highly conformal coating by single-molecule CVD, which we have described previously [7]. This latter theory, which assumes a Langmuirian relationship between surface concentration and precursor partial pressure, predicts that conformal films will be obtained when the precursor pressure is high, because the surface coverage is near saturated and therefore depends very weakly on precursor pressure. A key mechanistic aspect that leads to conformal growth is site blocking by adsorbed species that reduces the reactivity of the surface. When the boundary condition is assumed to be steady-state growth on all surfaces regardless of depth, the diffusion-reaction equation can be solved analytically. The calculated drop in precursor pressure from the top to the bottom of the feature is then used to determine the step coverage (*SC*) to first order [8]:

$$SC = 1 - \frac{\partial GR}{\partial p} \frac{c\rho k_B T}{2D_0} (AR)^2 \tag{1}$$

where c is a geometrical constant (2 for a trench and 4 for a via), ρ is the atomic density of the film, and D_0 is the molecular diffusion coefficient divided by the trench (or via) width. The step coverage in CVD is always less than unity, but can approach unity when the pressure-dependence of the growth rate is made very small.

The diffusion-reaction equation can be extended to two-molecule CVD systems using the same boundary condition. A new first order solution obtains:

$$SC = 1 - \left(\frac{\partial GR}{\partial p_A} \frac{\rho_A}{D_{0A}} + \frac{\partial GR}{\partial p_B} \frac{\rho_B}{D_{0B}} \right) \frac{c k_B T}{2} (AR)^2 \tag{2}$$

where A and B denote the two molecular reactants. However, *for two-molecule systems, the growth rate differential with respect to pressure need not be positive*. The explanation is qualitatively simple: if the growth rate depends directly on the fractional surface coverages of both co-reactants, and the two co-reactants compete for available surface sites in a Langmuirian way, then the rate must have a maximum at some ratio of component partial pressures and be smaller on either side of that peak; hence, there exists a regime in which the growth rate increases as the pressure of one component falls. As a result, under some circumstances the term in parentheses in Eq. (2) can be negative, in which case the *SC* is larger than unity, i.e., the coating is super-conformal. As we will show below, that regime emerges when the pressures of the components in the gas feed are chosen to take advantage of different molecular diffusion rates in the high *AR* feature.

In two-molecule CVD, there are several reports of decreasing growth rates vs. increasing component pressure: ZnO growth vs. oxygen pressure at a fixed pressure of DEZn[9]; TiN growth vs. $TiCl_4$ pressure at fixed NH_3 pressure [10]; and Si_3N_4 growth vs. NH_3 pressure [11]. A first order model that accounts for competitive adsorption and reaction on the growth surface was described by Cobianu and applied to the SiH_4/O_2 system, which displays a negative growth rate differential vs. SiH_4 pressure [12]. None of these studies, however, reported or discussed the possibility of super-conformal growth. Perfect conformality was reported for TiN growth using high $TiCl_4$ and low NH_3 pressures [10]; the authors of that work attributed the result to growth rate saturation at high $TiCl_4$ pressures, but did not consider the role of the low NH_3 pressure. The theory given here affords a general explanation.

To demonstrate and explore super-conformal coating for two-molecule CVD, we have investigated the following system: MgO growth from $Mg(DMADB)_2$ and H_2O, where DMADB = $H_3BNMe_2BH_3$. A complete kinetic model is reported.

2.2 Experiment

The CVD system is a turbo-pumped, cold-wall stainless steel chamber with a base pressure of 5×10^{-8} Torr, most of which is hydrogen [13]. In-situ spectroscopic ellipsometry is mounted at a 70° incidence angle. The $Mg(DMADB)_2$ precursor is prepared in the laboratory of Professor G. S. Girolami [14] DI water is used as the co-reactant. Precursor and water are kept in separate Pyrex containers adapted to stainless steel fittings, and fed into chamber through needle valves and separate 0.4 cm i.d. stainless steel tubes. Inside the chamber, the inlets of these tubes point towards the sidewall of the chamber in order to homogenize the flux, so the pressures reported are the average values inside the chamber. The substrate is heated radiatively by a tungsten wire mounted behind the substrate holder. The temperature is measured with a K type thermocouple clamped to the surface of substrate holder. For planar growth rate measurements, the substrate is a 0.5×0.5 inch silicon wafer with native oxide, cleaned using standard solvents without removing the oxide. For conformal coating studies, we use a lithographically defined microtrench with SiN walls, or a 'macro' trench-substrate with 25 or 100 μm width and ~ 1 cm depth, taken from n-type Si wafer with resistivity of 10-20 ohm-cm, covered with native oxide, as previously described [15]. Gas transport within the macrotrench is in the molecular flow regime; hence, the results can be rescaled to those in a microtrench with the same *AR*.

The refractive indices of MgO films are derived from *ex situ* spectroscopic ellipsometry data acquired at incident angles of 50, 60 and 70° under atmospheric pressure, and fit to the Cauchy equation [16]. The film thickness during growth is determined from *in situ* spectroscopic ellipsometry data using the derived indices and a multilayer optical model. In calibration experiments, the film thickness measured by ellipsometry is found to be within ± 5% of that determined from SEM cross-sectional images. The growth rate is derived by dividing the thickness increment by the time increment. The physical thickness of the MgO coating on macro-trench is measured with RBS at different depths; the profile is similar to that obtained from SEM cross-sectional images. A nearly constant film density, 63 ± 3% of the bulk value, is observed for the coating throughout the trench. The low density of the film is due to the low deposition temperature; at higher temperatures, e.g., 275°C, the film density is ~ 93% of the bulk value [17]. The temperature-dependent film density is accounted for in the analytical model below.

2.3 Growth Results

The MgO growth kinetics on planar substrates at 220°C have been measured to identify regimes of $Mg(DMADB)_2$ and H_2O partial pressures that may afford negative growth rate differentials with respect to pressure (Fig. 2.1). At partial pressures between 0.5 and 10 mTorr, the maximum MgO growth rate increases monotonically with increasing H_2O pressure, but the growth rate rises and then falls with increasing $Mg(DMADB)_2$ pressure. The data can be fit well to a kinetic model (next section) with

the parameters given in Table 2.1. A significant finding is that, for a H_2O pressure of 3.2 mTorr, the deposition rate decreases as the $Mg(DMADB)_2$ pressure is increased above 4.0 mTorr. Thus, under these conditions, we expect to see super-conformal growth. This expectation was confirmed by the following experiments.

MgO growth in a 25 μm wide macrotrench at 220°C is carried out with a fixed $Mg(DMADB)_2$ pressure of 7.5 mTorr, and H_2O pressures of either 3.0 or 10.0 mTorr. Growth using the higher water pressure affords a sub-conformal thickness profile with no coating past a normalized depth (depth divided by the aperture width, z/d) of ~ 25 (Fig. 2.2a). Remarkably, however, using the lower water pressure, the thickness *increases* with depth to a peak value at z/d ~ 18, then falls with no coating past z/d ~ 35.

In a microtrench with AR = 9:1, for a growth time of 10 minutes, the same conditions afford super-conformal growth all the way to the trench bottom (Fig. 2.2b, left). When deposition is continued for 20 minutes, the feature is completely filled (Fig. 2.2b, right).

At a higher temperature, 300°C, we find that super-conformal growth of MgO in a feature with AR = 5 can be achieved, but a lower water pressure is required (0.05 mTorr). This result is also consistent with the analytical model we now describe.

2.4 Model

In this section, we describe a model for surface reaction kinetics and the diffusion-reaction equation for two-molecule CVD systems. Taken together, these

formalisms quantitatively fit the observed coating profiles and can be used to predict the operating parameters that afford super-conformal coating in high aspect ratio features. The model has two main features. First, a kinetic competition between the two components occurs on the growth surface. Second, the component molecules have different molecular diffusivities and thus different pressure drops down the axis of the feature.

2.4.1 General Reaction Kinetics for Two-molecule CVD

The reaction pathways for two-molecule CVD are complex, involving competitive adsorption, surface transport and reaction, and byproduct removal steps. However, the overall kinetic behavior for film growth can be represented using a model based on the Langmuir-Hinshelwood formalism, with rate coefficients that represent the equilibrium between species adsorption and desorption, combined with the assumption that the rate-limiting step for film growth is the reaction of the adsorbates.

The two reactant molecules A and B undergo adsorption, desorption and surface reaction [18]:

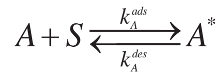

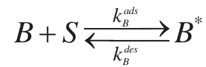

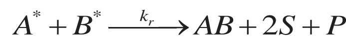

where S represents a surface absorption site, AB represents the deposited binary phase, P represents a reaction byproduct that desorbs from the surface and plays no further role, and the asterisk indicates an adsorbed state. Atomistic details such as the decomposition of the component molecules, and the formation and desorption of byproduct species are assumed to be fast and are therefore neglected. The slowest step will determine the rate of reaction:

$$R = k_r \theta_A^m \theta_B^n \qquad (3)$$

where θ_A and θ_B are the fractional surface coverages for the adsorbed species, m and n are the reaction orders, respectively, and k_r is the reaction coefficient per lattice site (in terms of formula units). When the reaction is first order in both A and B, that is, when both m and n equal unity, and the total fractional surface coverage is 1, the maximum growth rate occurs when $\theta_A = \theta_B = 0.5$. (The component partial pressures that afford this maximum growth condition will depend on the relative surface binding abilities of the two components, which is described by the four kinetic terms k^{ads} and k^{des} for adsorption of A and B on surface sites.) The present data can be fit adequately using the first-order model, and for the rest of this discussion, we will make this assumption. For a system that exhibits higher reaction orders, super-conformal coating can still be obtained, but the kinetic terms in the model must be recast accordingly.

From this model, we have derived the exact solution for the surface coverage terms as a function of the partial pressures and adsorption/desorption rates of the co-reactants [7] (Supplemental Material). The solution is more complex than the Langmuir-Hinshelwood equation because the latter neglects the surface reaction rate [12]; in the

limit where the reaction rate is negligibly small compared with adsorption/desorption rates, the solutions are identical.

We have fit the experimental data for MgO growth as a function of the component partial pressures to this model. The best-fit rate coefficients (Table 2.1) afford predicted growth rates that are in reasonable agreement with the data (Fig. 2.1). These parameters correspond to desorption energies of 0.99 and 1.05 eV for H_2O and $Mg(DMADB)_2$, respectively. This desorption energy for H_2O differs from the energy of 0.69 eV reported on clean MgO (100) surface [19]. We cannot determine from the present data whether this difference is due to the nature of the amorphous growth surface compared with the crystalline surface, to different lateral interactions between neighboring molecules in the mixed monolayer, or to other assumptions in the model, but even so the agreement is not bad.

The calculated rate of reaction *R* per surface site is related to the growth rate in film thickness via the factor *C*, defined as

$$C = N_{\text{surface}} / N_{\text{bulk}} \times 10^7 \text{ nm / cm} \times 60 \text{ sec / min} \qquad (4)$$

For crystalline MgO, $C = 15.9$. If the growing film has a lower density than the bulk, the effective value of *C* will be larger than this value; if not all surface sites are available for adsorption, then the effective value of C will be smaller than this value. We chose to consider *C* as a variable parameter along with the other adjustable parameters in the model. We find that the best-fit value is $C = 14.0$. We interpret this to indicate that not all surface sites are available for adsorption, due to one or more of the mechanisms that are possible under CVD growth conditions – lateral steric blocking by adsorbates,

slow desorption of reaction products, or site passivation. Even larger steric blocking effects are known to occur in atomic layer deposition, hence the best-fit C value is physically plausible.

We will show in the next sections that the parameters derived from the fits of the model to the experimental growth rate can be used to predict the conditions that should lead to super-conformal growth in recessed features.

2.4.2 Diffusivities and Pressure Drop Relationship

Transport of molecules of both co-reactants inside a deep feature occurs by molecular (Knudsen) flow, i.e., the diffusivity of each component is determined by wall collisions and is independent of the partial pressure [20]. For depths less than ~ 4 times the width, the diffusivity formalism is inaccurate due to directional flux in and out of the opening. It is possible to rescale the diffusion coefficient to correct for this effect [21] but we will not rescale here because we are concerned with super-conformal growth at greater depths, where the diffusion equation is accurate.

In a rectangular trench in steady state:

$$\frac{d\left(J_{A,B}/\rho_{A,B}\right)}{dz} = \frac{2R}{d_0} \tag{5}$$

$$J_{A,B}(z) = \frac{D_k^{A,B}}{kT}\frac{dP_{A,B}}{dz} \tag{6}$$

where $J(z)$ is the flux as a function of depth z, D_k is Knudson diffusivity, R is the reaction rate on the sidewalls, and d_0 is the width of the trench. The reaction consumes the component molecules at a fixed ratio ρ_A/ρ_B, which is merely the stoichiometric ratio of the

reaction. For our $Mg(DMADB)_2/H_2O$ system, this ratio is 1. Therefore, the ratio of pressure drops is a constant everywhere inside the feature:

$$\frac{\partial P_A}{\partial P_B} = \frac{\rho_A}{\rho_B} \times \frac{D_k^B}{D_k^A} \tag{7}$$

On a plot with axes P_A and P_B, the pressures of the two components as they change down the axis of the trench will trace out a straight line, beginning with the partial pressures outside of the feature and ending with those at the bottom.

For the MgO CVD system, Eq. (2) requires values for the diffusion coefficients for the reactant molecules and the densities of Mg and O atoms inside the film. In molecular flow, the diffusivities of the two molecules are inversely proportional to the square root of their molecular masses, hence:

$$D_k^{H_2O} / D_k^{Mg(DMADB)_2} = \sqrt{M_{Mg(DMADB)_2} / M_{H_2O}} \ . \tag{8}$$

Interestingly, fits to data (below) afford significantly lower values of the diffusivity than predicted from simple theory. Most likely, wall adsorption adds a residence time to the flight time for transport. For the MgO system, the ratio of experimental diffusivities, 4.5, is slightly larger than the ratio of 3 given by Eq. (8). The stoichiometry ratio for MgO is unity. Therefore the $Mg(DMADB)_2$ partial pressure drops 4.5 times more rapidly with depth than does the H_2O partial pressure.

For the majority of oxide, nitride, or carbide CVD systems, the metal-containing precursor has a significantly larger mass than that of the co-reactant. The resulting large

difference in the molecular diffusivities of the two co-reactants is what makes it possible to find conditions favorable for super-conformal growth, as we show next.

2.4.3 Prediction of Conformality

The regime of super-conformal growth can be represented graphically. The equilibrium adsorption coefficient [18] for each component, K^{eq}, is equal to the ratio k^{ads}/k^{des}. On a plot of the growth rate with axes $K_A^{eq}P_A$ and $K_B^{eq}P_B$, the pressures of the two components as they change down a recessed feature will trace a straight line. The line has a slope of $K_A^{eq}\rho_A D_k^B / K_B^{eq}\rho_B D_k^A$ and the peak growth rate occurs along the diagonal where $\theta_A = \theta_B$. The reaction rate constant k_r has a symmetric effect on the surface coverage of A and B molecules and does not influence this slope. *Provided that the slope of the line describing the pressure drop in this plot is not unity, super-conformal growth is possible if the partial pressures of the component species in the gas feed are chosen correctly.*

In the two-component CVD reaction, let us define species A to be the component that diffuses the most rapidly (for example, because it has the lower molecular mass). The partial pressures of the components outside of the trench opening, $P_A{}^0$ and $P_B{}^0$, are set experimentally via the gas injection rates. We will consider three cases, corresponding to points (1)-(3) in Fig. 2.3a. In case (1), $K_A^{eq}P_A{}^0$ is much smaller than $K_B^{eq}P_B{}^0$; in case (3) $K_A^{eq}P_A{}^0$ is equal to $K_B^{eq}P_B{}^0$; and case (2) is intermediate between cases (1) and (3). In the plots of how $K_A^{eq}P_A$ and $K_B^{eq}P_B$ evolve down the trench, the three cases trace separate parallel lines that correspond to different variations in the growth rate (Fig. 2.3b). Case

(1) is predicted to afford conformal coating. Although the drop in partial pressures does move towards the line of equal surface coverage ($\theta_A = \theta_B$), in a deep feature component A becomes exhausted, which reduces the growth rate ($\theta_A + \theta_B$ falls below 1). Note that for a finite *AR* – such that *A* is not fully exhausted – these conditions can give excellent conformality. Case (3) gives bad conformality because the drop in partial pressures is away from the $\theta_A = \theta_B$ line, so the growth rate falls rapidly. Case (2) affords super-conformal coating from the starting point to the depth at which the partial pressures cross the $\theta_A = \theta_B$ line. Therefore, the aspect ratio must be chosen so that the pressures never move past the diagonal.

Substrate temperature affects the regime of super-conformal coating primarily through the temperature dependence of the equilibrium adsorption coefficients, K^{eq} , and secondarily through the molecular diffusivities. The latter may include a wall adsorption term (next section) that enhances the temperature dependence over that predicted by the kinetic theory of gases. Therefore, the slopes of the lines in the $K_A^{eq}P_A$ vs. $K_B^{eq}P_B$ plot change with temperature. In addition, the scale factor *C* will be temperature dependent (because of the changing film and surface site density) and must be accounted for. Each precursor-film system will exhibit a different regime of super-conformality depending on the kinetic coefficients of the species involved. In general, higher temperatures will narrow the process conditions in which super-conformal growth can be achieved because the higher growth rate increases the depletion of reactants within the structure.

2.5 Analysis and Discussion

2.5.1 Effect of Wall Adsorption on the Diffusivity

The diffusion coefficient in the trench can be determined by comparing the actual and calculated pressure drops. For steady-state growth, the continuity equation relates the molecular flux *J(z)* to the integrated growth rate *GR* below that depth:

$$J(z) = \int_z^L GR(z)\rho dz \tag{9}$$

where *L* is the trench depth, chosen large enough that the coating thickness tapers to zero before the bottom. We analyze the MgO growth profile of Fig. 2.2, for a H_2O pressure of 3.0 mTorr. At the growth temperature of 220°C, the atomic density is 3.4×10^{22} at/cm^3, which is 63 % of the bulk value (it is 93% for growth at 275°C[17]). The stoichiometry of MgO is measured to be 1:1, hence, *the consumption rates of* $Mg(DMADB)_2$ *and* H_2O *on the walls at any particular depth are always equal*. Integrating from the bottom up affords the profile of flux down the axis of the feature (Fig. 2.4a).

Fick's law relates the flux to the pressure profiles of each component. The bottom boundary condition is zero pressure for the component that is fully depleted, the $Mg(DMADB)_2$ precursor in this case. For the component that is not fully depleted, H_2O in this case, the bottom boundary condition is a zero pressure gradient. Integrating the flux profile from the bottom up affords a prediction of the pressure that must exist at the trench opening. However, inserting the Knudsen diffusivity affords a predicted pressure which is smaller by a factor of ~ 10 than the experimental pressure. These values can be brought into agreement (Fig. 2.4b) by assuming that the molecular components adsorb on the walls, which adds a characteristic residence time τ_0 to the flight time [20] and reduces

the diffusivity (for H_2O, the residence time is estimated through the known starting pressure, the flux profile, and the best fit to the coating profile):

$$D^k = \frac{d^2}{3\left(\frac{d}{v} + \tau_0\right)} \tag{10}$$

We obtain a best-fit for residence times of 2.5×10^{-6} and 5.6×10^{-7} s for $Mg(DMADB)_2$ and H_2O, respectively. If we further assume that the prefactor for desorption [22] is 10^{13} s^{-1} , then these residence times correspond to binding energies of about 0.72 and 0.66 eV, respectively. For H_2O, the estimate is comparable to the value of 0.69 eV determined by TPD [19] for desorption on MgO(100), which lends credence to the postulate of wall adsorption.

We note, for completeness, that the angular distribution of emission events from the wall can also modify the value of the diffusivity via the mean transport distance. This distribution is usually assumed to vary as the cosine with respect to the normal [23].

Combining the pressure distributions of the two components with the kinetic model for growth affords a simulated coating profile in excellent agreement with experiment (Fig. 2.5).

2.5.2 Relationship between GR, AR, SC

The relationship between the aspect ratio, step coverage, and growth rate can be determined from an analytical approximation [8] as follows. For super-conformal coating, the pressure at the bottom of the feature must not fall below the value for the peak growth rate (Figs. 2.2a or 2.3b). This minimum pressure can be determined

experimentally from growth rate measurements on planar substrates. In the trench, the pressure drop down the axis is calculated by means of the diffusion equation. In principle, this equation must be solved numerically because the growth rate depends in a complex manner on the component pressures. However, for aspect ratios up to ~ 20:1 and well-chosen operating conditions, the variation on growth rate is observed experimentally to be nearly linear between the trench opening and bottom (Fig. 2.6); this is because the growth conditions are not too far from being perfectly conformal. If the growth rate is assumed to be linear with depth and defined by the slope *s*:

$$GR(z) = GR_0\left(1 + s \times \frac{z}{d_0}\right), \text{ where } s = \frac{GR_L - GR_0}{AR} \times \frac{1}{GR_0} \tag{11}$$

The gas phase boundary conditions are:

$$P_{A,B}(0) = P_{A0,B0} \text{ and } \frac{D_{A,B}}{kT}\frac{dP_{A,B}}{dx}\bigg|_{x=L} = -\rho_{A,B}GR(L); \tag{12}$$

where *L* is the trench depth.

The diffusion equation can now be solved analytically, such that the slope *s* is self-consistent, to relate the *AR*, *SC*, GR_0 and ΔP from top to bottom of the trench:

$$\Delta P_{A,B} = \frac{\left(\frac{SC}{3} + \frac{1}{6}\right) ckT\rho_{A,B}GR_0}{D_{A,B}^k / d_0}(AR)^2 \tag{13}$$

where $SC = GR_L / GR_0$, and *c* is a geometrical constant, as discussed in the Introduction [8].

If the growth rate differentials as a function of the partial pressures are nearly constant for a certain pressure regime, then the following approximation holds:

$$GR(P_A - \Delta P_A, P_B - \Delta P_B, T) = GR_0 - \frac{\partial GR}{\partial P_A}\Delta P_A - \frac{\partial GR}{\partial P_B}\Delta P_B \qquad (14)$$

Then, the step coverage is:

$$SC = 1 - \frac{1}{GR_0}\frac{\partial GR}{\partial P_A}\Delta P_A - \frac{1}{GR_0}\frac{\partial GR}{\partial P_B}\Delta P_B \qquad (15)$$

Substituting (12) into (14) for ΔP_A and ΔP_B affords:

$$SC = 1 - \left(\frac{\partial GR}{\partial P_A}\frac{\rho_A}{D_A^k/d_0} + \frac{\partial GR}{\partial P_B}\frac{\rho_B}{D_B^k/d_0}\right)\left(\frac{SC}{3} + \frac{1}{6}\right)ckT\left(AR\right)^2 \qquad (16)$$

After being rearranged, the equation for SC is:

$$SC = \frac{1 - \frac{M}{6}}{1 + \frac{M}{3}} \qquad (17)$$

where $M = \left(\frac{\partial GR}{\partial P_A}\frac{\rho_A}{D_A^k/d_0} + \frac{\partial GR}{\partial P_B}\frac{\rho_B}{D_B^k/d_0}\right)ckT\left(AR\right)^2$.

This equation predicts the value of SC for a given set of P_A, P_B, and T conditions, assuming that the growth rate change inside the trench is linear with respect to depth (which is valid according to our data for MgO), and the GR differential with respect to either partial pressure is relatively constant. (It is of course possible to violate these assumptions; the point is to gain insight that applies to a useful range of conditions.) When the M factor – the combined effect of the growth rate differentials – is negative, then the SC is > 1 and the coating is super-conformal. When the M factor is nearly 0, SC is close to 1 and equation (16) reduces to equation (2).

The relationship given by Eq. (13) can be combined with the best-fit parameters for MgO growth at 220°C (Table 2.1) to construct two parametric plots. For a given set of starting pressures, one plot can be used to determine the maximum *AR* that can be coated super-conformally (Fig. 2.7a), and to determine the *SC* that is possible for this *AR* (Fig. 2.7b). If the actual *AR* is larger than this maximum value, the precursor pressure will drop past the growth rate maximum, hence the film thickness will peak and then start to decline before the trench bottom. If the actual *AR* is smaller than the maximum, the pressure drop will be smaller and the step coverage will be less super-conformal. These plots, accurate to first order, provide clear guidance about the coating profile that can be achieved.

When super-conformal coating conditions are used to fill a deep feature, the aspect ratio *AR* increases with time as the coating builds up on the sidewalls. It may be necessary to adjust the component pressures according to the AR chart. Alternatively, it can suffice to employ super-conformal conditions only long enough to establish a V shape on the sidewalls, and then to use conditions that have *SC* ~ 1. This option is analyzed in Chapter 3 below.

A potential complication not discussed above is the possibility that reaction byproducts are not inert, but can adsorb or decompose on the film growth surface. The partial pressure of byproducts can readily be calculated from the steady-state diffusion equation based on the measured film thickness profile (growth rate); the partial pressure increases rapidly with *AR*. Reversible adsorption would contribute site blocking and reduce the film growth rate; decomposition would change the surface reactivity, likely

reducing the growth rate, and introduce unwanted elements (impurities) into the film composition. The systems studied to date achieve super-conformal coating in reasonable agreement with the theory presented here and are stoichiometric with low impurity content. These observations suggest that byproduct adsorption does not play a significant role. Although some candidate systems might suffer from byproduct reactions, we expect that the super-conformal growth method will be applicable to a broad portfolio of useful systems.

2.6 Summary

We demonstrate that super-conformal thin film coatings can be achieved for two-component CVD systems, most simply by supplying a gas feed in which the more slowing diffusing (more massive) molecular co-reactant is in excess. This phenomenon arises from competitive adsorption behavior on the film growth surface and the difference in Knudsen diffusivities between the co-reacting molecules. Super-conformal MgO growth using $Mg(DMADB)_2$ and H_2O is demonstrated. Kinetic data are obtained from growth rate data on planar substrates and film thickness profiles on macro-trench substrates. A predictive theory for super-conformal coating is derived based on a kinetic model for growth in combination with diffusive transport in a deep feature. The diffusion coefficients are modified favorably by adsorption of the components on the sidewalls. Finally, we derive an analytic relationship between the starting pressures of the co-reactants, the feature aspect ratio, and the step coverage for super-conformal growth.

2.7 Appendix

Derivation for equation of surface coverage:

At steady state, the fractional surface coverages θ_A and θ_B for adsorbed species A^* and B^* are constant with time, giving the following equations (18):

$$\frac{\partial\theta_A}{\partial t} = k_A^{ads} P_A (1-\theta_A-\theta_B) - k_A^{des}\theta_A - k_r\theta_A\theta_B = 0;$$
$$\frac{\partial\theta_B}{\partial t} = k_B^{ads} P_B (1-\theta_A-\theta_B) - k_B^{des}\theta_B - k_r\theta_A\theta_B = 0. \quad (18)$$

where k^{ads}, and k^{des} stand for adsorption and desorption rate constants respectively, and k_r is the reaction rate constant for formation of the binary phase. From these two equations, specific equations for θ_A and θ_B based on P_A and P_B and 5 different coefficients can be derived. The equation for θ_A is shown below as equation (19), and the counterpart for θ_B is symmetric, i.e., the A and B subscripts are exchanged [7].

$$\theta_A = \frac{-M \pm \sqrt{M^2 - 4KN}}{2K};$$
$$K = k_r k_B^{ads} P_B - k_r k_A^{ads} P_A - k_r k_A^{des};$$
$$M = k_r k_A^{ads} P_A - k_r k_B^{ads} P_B - k_A^{ads} k_B^{des} P_A - k_A^{des} k_B^{ads} P_B - k_A^{des} k_B^{des};$$
$$N = k_A^{ads} k_B^{des} P_A; \quad (19)$$

All these 5 coefficients follow Arrhenius behavior, with different activation energies,

$$k = Ce^{-E_a/RT}. \quad (20)$$

2.8 References

1. H. Kim, H. B. R. Lee, and W. J. Maeng, "Applications of atomic layer deposition to nanofabrication and emerging nanodevices", *Thin Solid Films* **517,** 2563-80 (2009).

2. W. Lang, "Silicon microstructuring technology", *Mater. Sci. Eng. R-Rep.* **17,** 1-55 (1996).

3. *International Technology Roadmap for Semiconductors* (2009).

4. M. Esashi and T. Ono, "From MEMS to nanomachine", *J. Phys. D-Appl. Phys.* **38,** R223-R30 (2005).

5. F. Ayazi and K. Najafi, "High aspect-ratio combined poly and single-crystal silicon (HARPSS) MEMS technology", *Journal of Microelectromechanical Systems* **9,** 288-94 (2000).

6. R. Abdolvand, H. Johari, G. K. Ho, A. Erbil, and F. Ayazi, "Quality factor in trench-refilled polysilicon beam resonators", *Journal of Microelectromechanical Systems* **15,** 471-8 (2006).

7. A. Yanguas-Gil, N. Kumar, Y. Yang, and J. R. Abelson, "Highly conformal film growth by chemical vapor deposition. II. Conformality enhancement through growth inhibition", *Journal of Vacuum Science & Technology A* **27,** 1244-8 (2009).

8. A. Yanguas-Gil, Y. Yang, N. Kumar, and J. R. Abelson, "Highly conformal film growth by chemical vapor deposition. I. A conformal zone diagram based on kinetics", *Journal of Vacuum Science & Technology A* **27,** 1235-43 (2009).

9. J. D. Ye, S. L. Gu, W. Liu, S. M. Zhu, R. Zhang, Y. Shi, Y. D. Zheng, X. W. Sun, G. Q. Lo, and D. L. Kwong, "Competitive adsorption and two-site occupation effects in metal-organic chemical vapor deposition of ZnO", *Appl. Phys. Lett.* **90** (2007).

10. K. Jun, Y. Egashira, and Y. Shimogaki, "Kinetics of TiN chemical vapor deposition process using $TiCl_4$ and NH_3 for ULSI diffusion barrier applications: Relationship between step coverage and NH_3 partial pressure", *Jpn. J. Appl. Phys. Part 1 - Regul. Pap. Short Notes Rev. Pap.* **43,** 7287-91 (2004).

11. J. M. Grow, R. A. Levy, X. Fan, and M. Bhaskaran, "Growth kinetics and characterization of low-pressure chemically vapor deposited Si_3N_4 films from $(C_4H_9)_2SiH_2$ and NH_3", *Materials Letters* **23,** 187-93 (1995).

12. C. Cobianu and C. Pavelescu, "A theoretical-study of the low-temperature chemical vapor deposition of SiO_2 films", *Journal of the Electrochemical Society* **130,** 1888-93 (1983).

13. D. M. Hoffman, *Handbook Of Vacuum Science and Technology* (Academic Press, San Diego, 1998).

14. D. Y. Kim and G. S. Girolami, "Highly volatile magnesium complexes with the aminodiboranate anion, a new chelating borohydride. synthesis and characterization of $Mg(H_3BNMe_2BH_3)_2$ and related compounds", *Inorg. Chem.* **49,** 4942-8 (2010).

15. Y. Yang, S. Jayaraman, D. Y. Kim, G. S. Girolami, and J. R. Abelson, "CVD growth kinetics of HfB_2 thin films from the single-source precursor $Hf(BH_4)_4$", *Chem. Mat.* **18,** 5088-96 (2006).

16. F. A. Jenkins, H. E. White, *Fundamentals of Optics*, 3rd ed. (McGraw-Hill, Inc., New York, 1957).

17. W. B. Wang, Y. Yang, A. Yanguas-Gil, N. N. Chang, G. S. Girolami, and J. R. Abelson, "Highly conformal magnesium oxide thin films by low-temperature chemical vapor deposition from $Mg(H_3BNMe_2BH_3)_2$ and water", *Appl. Phys. Lett.* **102** (2013).

18. R. I. Masel, *Principles of Adsorption and Reaction on Solid Surfaces* (Wiley-Interscience, 1996).

19. C. Xu and D. W. Goodman, "Structure and geometry of water adsorbed on the MgO(100) surface", *Chem. Phys. Lett.* **265,** 341-6 (1997).

20. J. Schlote, K. W. Schroder, and K. Drescher, "Fundamental conceptions modeling the thickness distribution of low-pressure chemically vapor-deposited films on wafers and within narrow trenches", *Journal of the Electrochemical Society* **138,** 2393-7 (1991).

21. Y. Yang, Thesis, University of Illinois at Urbana-Champaign, 2007.

22. J. E. Mahan, *Physical Vapor Deposition of Thin Films* (John Wiley & Sons, Inc., New York, 2000).

23. R. Feres and G. Yablonsky, "Knudsen's cosine law and random billiards", *Chemical Engineering Science* **59,** 1541-56 (2004).

2.9 Tables and Figures

K_r	$K_{H_2O}^{ads}$	$K_{H_2O}^{des}$	$K_{Mg(DMADB)_2}^{ads}$	$K_{Mg(DMADB)_2}^{des}$	C
7.81	0.13	0.25	0.18	0.26	14

Table 2.1. Best fit values for adsorption, desorption and reaction coefficients for MgO CVD from $Mg(DMADB)_2$ and H_2O at 220°C. "C" is a conversion-factor for K_r from reaction rate per site per second to film growth rate in nm/min.

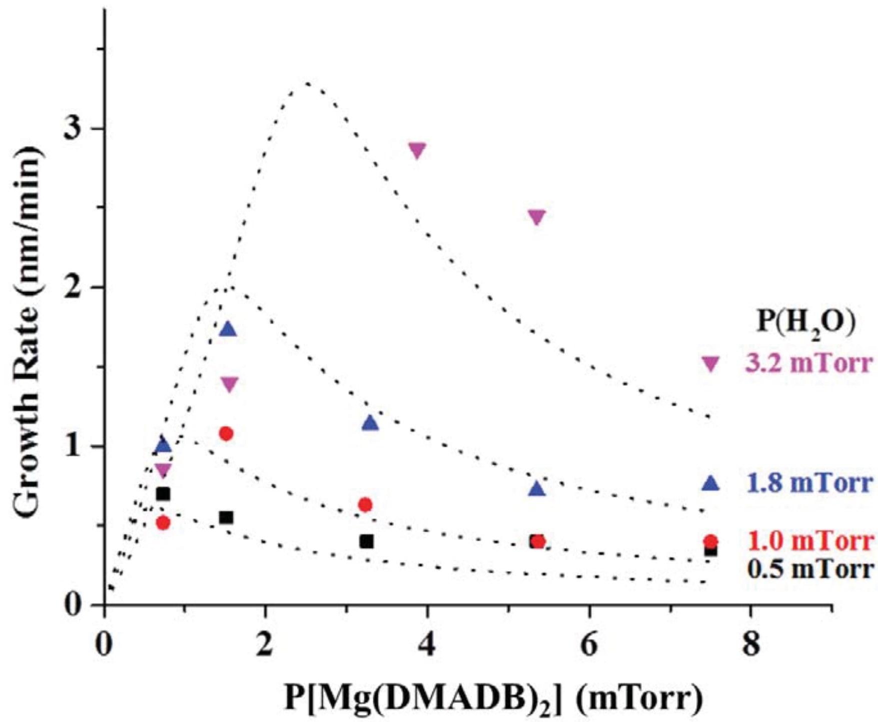

Figure 2.1. Growth rate as a function of $Mg(DMADB)_2$ and H_2O pressures at 220°C, as measured with ellipsometry on Si (100) planar substrates. Fitting lines are based on the kinetic equations discussed in model section; the parameters are given in Table 2.1.

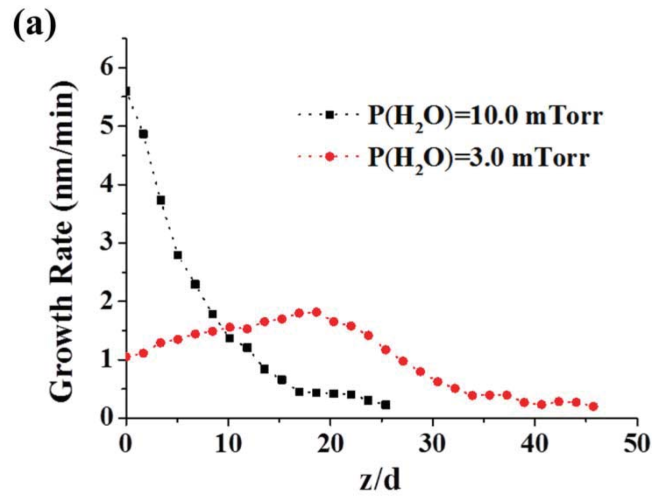

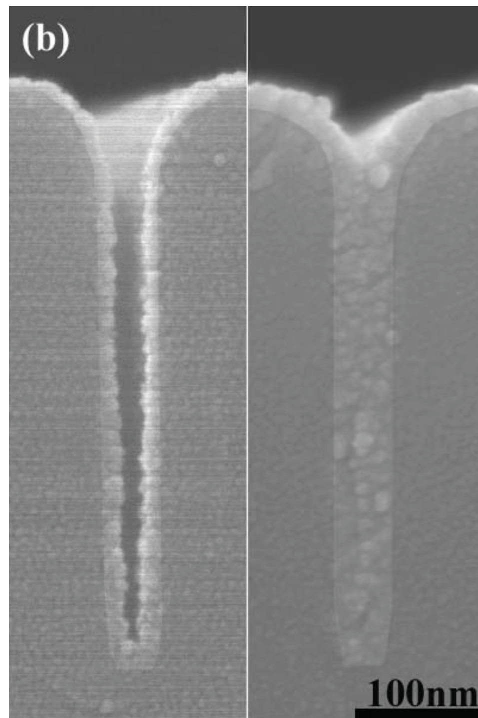

Figure 2.2. (a) Coating profiles for MgO films deposited in macroscopic trenches at 220°C, with P[Mg(DMADB)$_2$] = 7.5 mTorr, and P[H_2O] = 10.0 mTorr or 3.0 mTorr. (b) Left: SEM image of MgO coating with P[Mg(DMADB)$_2$] = 7.5 mTorr and P[H_2O] = 3.0 mTorr for 10 minutes at 220°C in a microscopic SiN/Si trench with AR = 9:1; right: SEM image of a completely filled trench after coating with the same condition for 20 minutes.

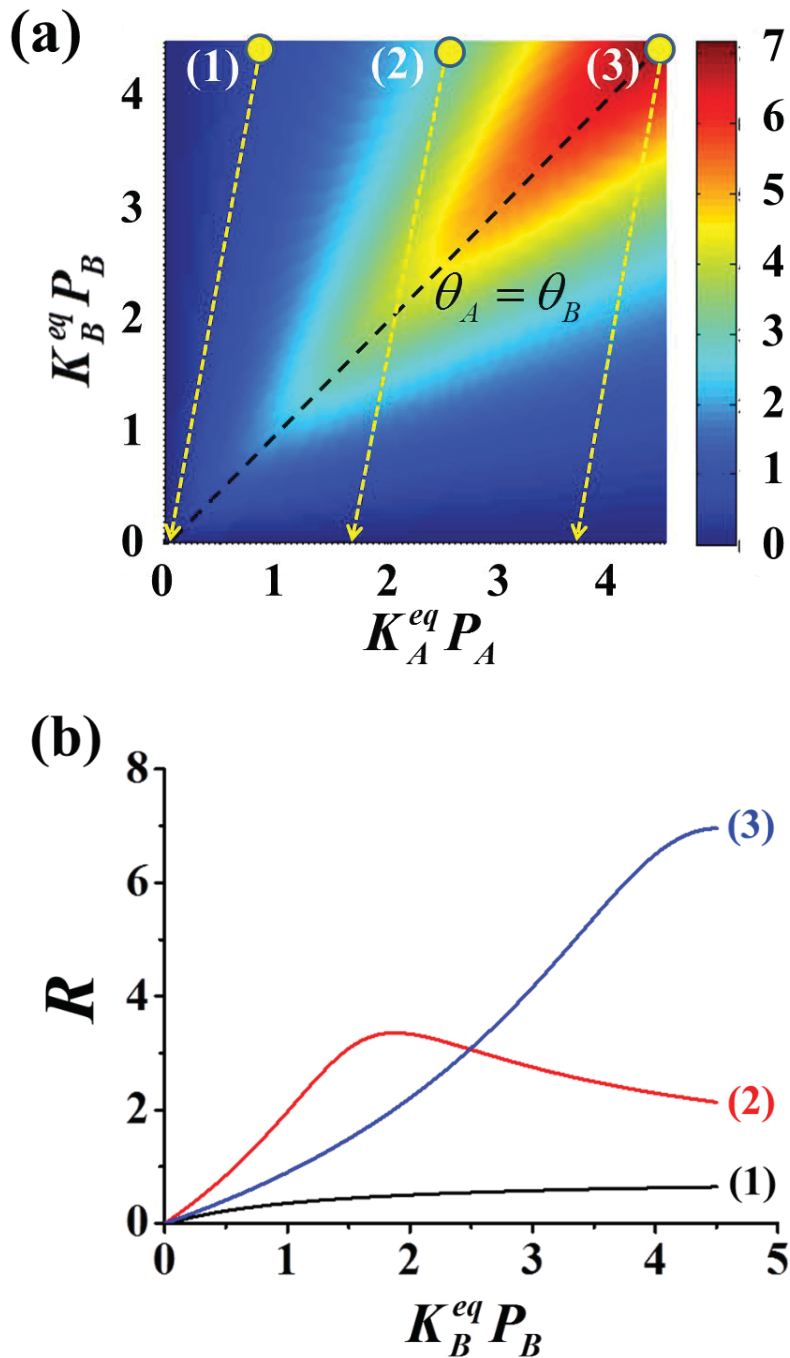

Figure 2.3. (a) Graphic presentation of two-molecule CVD growth rates, with pressure drop profiles (starting from three different pressures) given as yellow broken lines. Relative rates are indicated by the color bar at right. (b) Growth rate along the three different pressure drop lines as a function of $K_B^{eq} P_B$, with starting pressures at the three different points in (a).

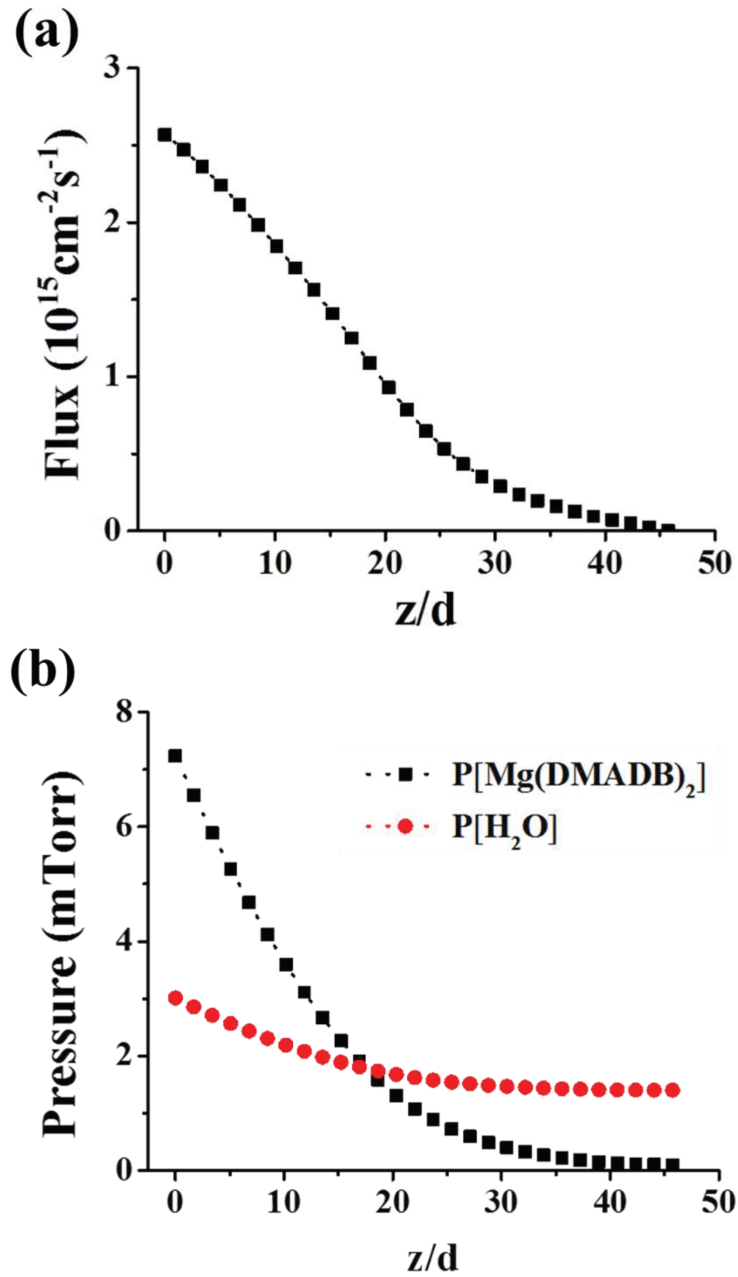

Figure 2.4. The calculated molecule flux (a) and pressure distributions (b) for MgO coating in a macrotrench at 220°C with P[Mg(DMABD)$_2$] = 7.5 mTorr and P[H_2O] = 3.0 mTorr.

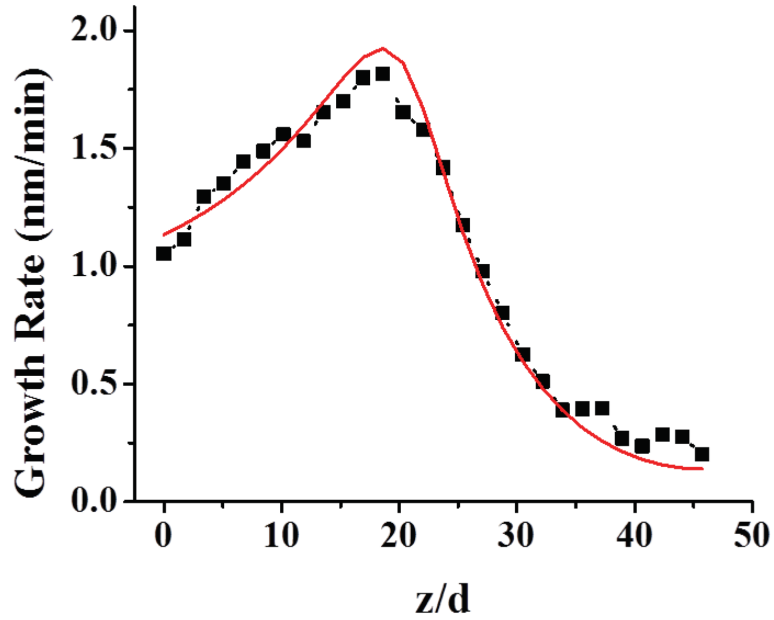

Figure 2.5. Comparison between simulated coating profile (solid red line) and experiment (solid black squares), for MgO macroscopic trench coating with P[Mg(DMABD)$_2$] = 7.5 mTorr and P[H_2O] = 3.0 mTorr, at 220°C.

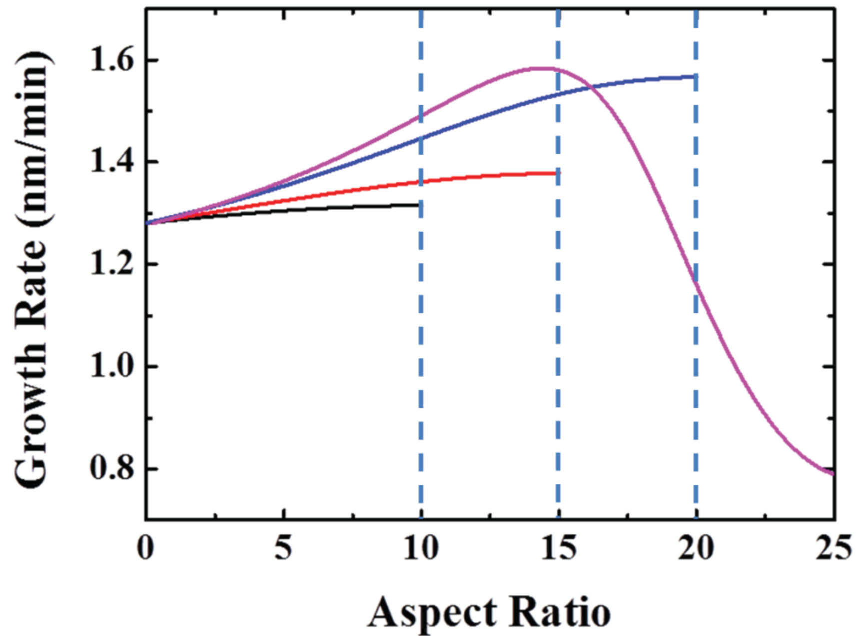

Figure 2.6. Simulated coating profiles using the growth rate equation and diffusivities in the previous section with Mg(DMADB)$_2$ and H_2O pressures of 7.5 mTorr and 3.4 mTorr, respectively, for trenches of AR = 10, 15, 20 and 25 (broken lines).

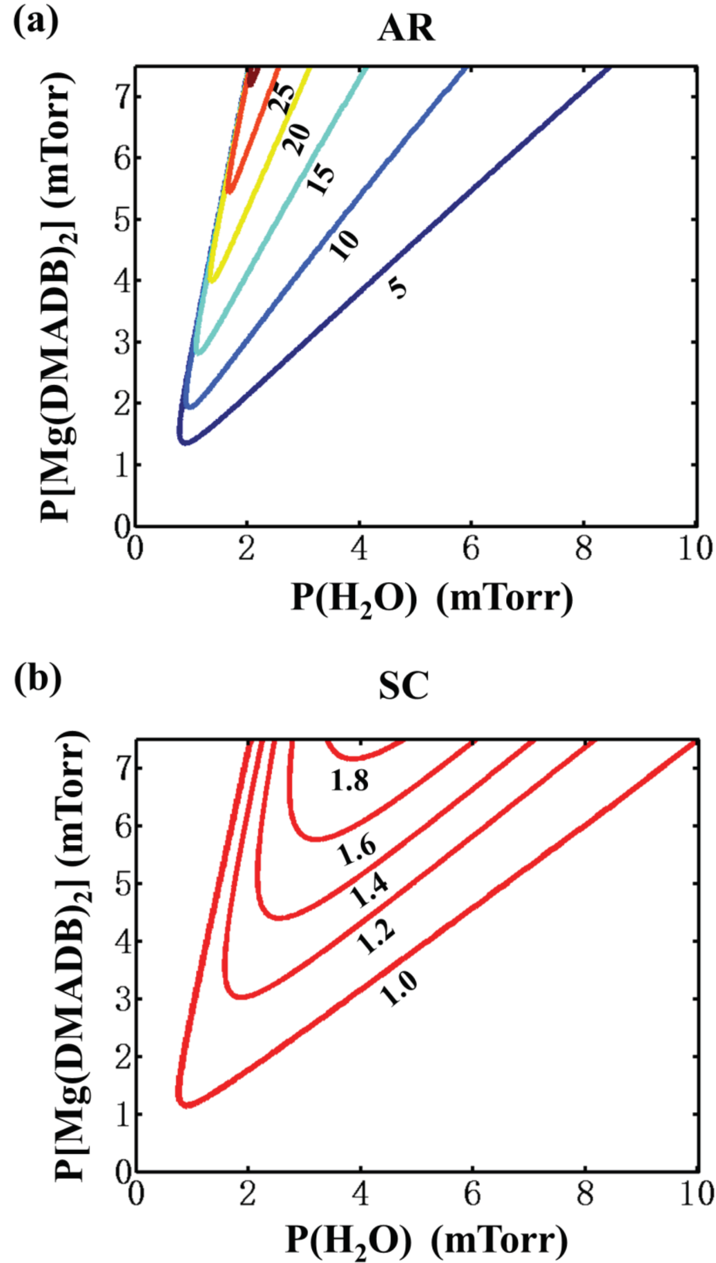

Figure 2.7. The (a) aspect ratio (AR), and (b) step coverage (SC) for trench coating with various $Mg(DMADB)_2$ and H_2O pressures that can afford super-conformality, using simulated growth rates for MgO at 220°C. For each $Mg(DMADB)_2$ and H_2O pressure combination, the maximum aspect ratio of the trench that can be super-conformally coated is given by the left figure, then the corresponding step coverage is determined by the corresponding point in the right figure.

CHAPTER 3

CRITICAL CONDITION FOR FILLING: SUPER-CONFORMAL COATING TO AFFORD TAPERED SIDEWALLS

3.1 Introduction

Many nanoscale device designs incorporate deep recesses (features) that must be filled with a second material during the manufacturing process. Examples include metallization [1] and shallow trench isolation (STI) [2] in integrated circuits, microelectromechanical systems (MEMS) [3], and optical waveguides [4]. As device designs advance, the feature size is typically reduced and the aspect ratio (AR) increased [5], which make the filling process more difficult to achieve. With incomplete filling, a trapped void space or "seam" of low-density material is left along the centerline of the feature; these defects are highly undesirable as they decrease the property of interest, often the electrical or thermal conductivity. As addressed in Chapter 1, to achieve complete filling for these applications, the deposition process must be highly conformal, or even super-conformal, i.e., the growth rate *increases* from the feature opening to the bottom.

Highly conformal coatings can be grown by chemical vapor deposition (CVD) or by atomic layer deposition (ALD). Previous studies have shown – qualitatively – that to achieve complete filling without void formation, the feature must be fabricated with an inwardly angled sidewall [6,7]. The problem with parallel sidewalls is that the width

decreases and the aspect ratio increases as coating builds up on the opposite faces; transport of the precursor species to the bottom of the feature drops to negligibly small rates, creating the void or seam that cannot be filled [7-10]. However, it would be a major device design and manufacturing constraint to require that all features have a specified taper angle on the sidewalls.

Super-conformal coating methods can produce inward-angled sidewalls starting with a feature whose sidewalls are parallel or even angled slightly outward; thus, complete filling can be achieved over a range of design geometries and manufacturing tolerances. In Chapter 2, we report a new super-conformal coating method for two-component CVD at low substrate temperature. This is distinct from other reported methods that afford super-conformal coating [11-19].

However, filling is a dynamic process in which the feature shape and aspect ratio continuously evolve. A coating condition that affords super-conformal growth for the *initial* feature geometry is not guaranteed to afford the same behavior all the way through the filling process. We are not aware of any previous study that derived a set of critical conditions sufficient to predict when complete filling can or cannot be achieved. Such a theoretical framework would be invaluable – it would afford limits on allowable device dimensions according to the performance of super-conformal coating processes. Here, for the first time, we quantitatively analyze the super-conformal coating profile for inward-tapered wall shape for filling, and derive critical conditions for complete filling, namely, limits on the sidewall taper angle and the feature aspect ratio. We consider two alternate formalisms for particle transport in the feature: (i) molecular diffusion is

mathematically convenient but, as we will show, underestimates the precursor fluxes at large depths; and (ii) ballistic transport between solid angle elements in the feature is computationally intensive but provides a significantly more accurate (and encouraging) answer to the present problem.

We present results for a generalized two-component super-conformal CVD process, and then for the specific case of MgO growth using $Mg(DMADB)_2$ precursor with H_2O as the co-reactant, for which we have experimental data. The starting case is a trench with parallel sidewalls, which is progressively transformed into a V-shape by the super-conformal deposition process. *The critical condition for success is that the growth remains super-conformal all the way to the bottom of the apex, as opposed to reaching a peak rate at intermediate depth and then declining towards the bottom.* The diffusion-reaction formalism predicts a void space at the bottom of the feature, whereas the experimental result is complete filling. By contrast, the ballistic transport formalism predicts complete filling. Detailed analysis shows that long-range transport events – particles that are emitted from the walls at glancing angles and arrive at great depths in the feature – make the critical difference. Such events are not accounted for in the diffusion model, which represents all transport events using a single valued, average transport distance between collisions.

3.2 Model Assumptions

In the diffusion-reaction model and ballistic transport models discussed below, we make the following assumptions:

1. Inter-molecular collisions can be neglected because the feature sizes range from nm to μm, which is much smaller than the mean free path of ~ one cm under a total pressure of ~ mTorr; therefore gas phase diffusivity can be described using Knudsen's equation [20].
2. The gas molecule distribution does not have cross-sectional variance at the same depth. In diffusion model, we will only consider the gas molecule concentration change in its depth.
3. Surface diffusion of growth species is negligible, and has no effect on the coating profile. (This assumption does not rule out local effects such as smoothing.)
4. The source of gas molecules outside the trench is spatially homogeneous and constant as a function of time.
5. The distribution of gas molecules is in steady state. In the diffusion model, the time differential is zero. In the ballistic model, steady state is assured as follows: in cases where the sticking probability is a function of flux, enough computational cycles are performed to reach convergence; in cases with a constant sticking probability, the distribution is calculated directly using the matrix method, as discussed below.
6. The re-emission of flux from trench wall follows cosine law. There is a report showing that when the adsorption surface has roughness or even micro-structures, the re-emission of adsorbed molecules follows a cosine law [21].
7. The inward-tapered trench shape is assumed to have a linear change in width as a function of depth, which is the essential result with two-molecule superconformal CVD (Chapter 2).

3.3 Diffusion-reaction Model

3.3.1 Model Description

Under the above assumptions, the transport of gas molecules inside the feature consists of line-of-sight trajectories, wall collisions, and reaction to form film or reemission in a cosine distribution about the local normal, continuing until all molecules have either been consumed or lost back out the opening of the feature. The net transport of molecules is calculated using the diffusion approximation. We consider conditions (partial pressures of precursor and co-reactant) that afford super-conformal growth, as described in Chapter 2. Superconformal growth progressively converts the parallel sidewalls of a rectangular trench to an inward-inclined shape (Fig. 3.1).

Conservation of mass requires that the decrease in the flux of molecules down the axis of the feature equal the consumption rate on the sidewalls to deposit film:

$$d[J(z) \times A(z)] = -C(z) \times R(z) \times dz / \sin\theta \qquad (1)$$

where J(z) and A(z) are the flux and cross-sectional area at depth z, C(z) is the circumference of the trench, and R(z) is the reaction rate, in units of molecules / [second×area]. For a trench with length much larger than the width,

$$\frac{A(z)}{C(z)} = w(z)/2 \qquad (2)$$

where w(z) is the width of trench at depth z.

Equations (1) and (2), together with Fick's first law, and the Knudsen gas phase diffusivity

$$D_k(z) = \frac{1}{3} w(z)\bar{v} \quad (3)$$

describe the pressure distribution for this inward-inclined sidewall:

$$\begin{cases} J(z) = -\frac{D_k(z)}{kT}\frac{dP}{dz} \\ \frac{d[J(z)\times w(z)]}{dz} = -2R/\sin\theta \end{cases} \quad (4)$$

When the width decrease is a linear function of depth, and the angle between the sidewall and the cross-sectional plane is θ, then:

$$\frac{dw(z)}{dz} = 2\cot\theta \quad (5)$$

Combining equations (3), (4), and (5):

$$\frac{D_0}{kT}\frac{d^2P}{d\left[{}^{z}/_{w(z)}\right]^2} - 2\cot\theta\frac{D_0}{kT}\frac{dP}{d\left[{}^{z}/_{w(z)}\right]} = {}^{2R}/_{\sin\theta} \quad (6)$$

where D_0 is the normalized diffusivity, defined as D_k / w(z), which is a constant according to Equation (3). When θ is equal to 90°, this equation reverts to the form for a rectangular trench.

For a feature under molecular flow conditions, the coating profile is a function of the AR but independent of the absolute dimensions. This is the case because wall collisions determine the transport kinetics, and are statistically equivalent for features of the same shape but different sizes. Similarly, in Equation (6) the steady state pressure

profile inside an inward-tapered trench is a function of the ratio of depth over width, here called the effective position, P_{eff}. Accordingly, we define the effective aspect ratio, AR_{eff}, as the integral of the depth increment over the local width, from the opening to the bottom of the feature (Eq. 7). This quantity will be used to describe the pressure and growth rate profiles in a feature with inward-tapered sidewalls (Eq. 6), and facilitates comparison between features. For features with the same θ angle and AR_{eff}, the coating profile will not depend on the absolute dimensions.

For an inward-tapered trench with depth L_0 and opening size W_0, the AR_{eff} and P_{eff} (Fig. 3.2) are:

$$\begin{cases} AR_{eff} = \int_0^{L_0} \frac{dz}{w(z)} = \frac{\tan\theta}{2} \ln\left(\frac{\tan\theta/2}{\tan\theta/2 - L_0/W_0}\right) \\ P_{eff}(\mathrm{z}) = \int_0^{z} \frac{dz}{w(z)} = \frac{\tan\theta}{2} \ln\left(\frac{\tan\theta/2}{\tan\theta/2 - z/W_0}\right) \end{cases} \quad (7)$$

After solving for the steady state pressure distribution as a function of P_{eff}, this equation is used to translate the P_{eff} and AR_{eff} into the normalized position P_{nom} and the normalized aspect ratio AR_{nom}, which are z/W_0 and L_0/W_0, respectively, in order to evaluate the conformality of the coating. According to this equation, the AR_{eff} increases to infinity when the inward-tapered trench becomes 'V' shaped and the depth z reaches the very apex, because the width goes to zero. This mathematical issue does not occur in reality because the apex cannot be infinitely small. We assume that the smallest possible apex can be approximated by a flat region with a width 0.01 that of the opening. The justification is that at this scale, local effects such as surface roughness and smoothing dominate the shape. For example, a V-shaped trench with a 100 nm opening is assumed

to have a 1 nm wide bottom. For a taper angle of θ = 88°, AR_{nom} = 14.3, but AR_{eff} = 66 (Fig. 3.3).

The boundary condition for the diffusion-reaction model (Eq. 6) is:

$$\begin{cases} P(0) = P_0 \\ -\frac{D_0}{kT}\frac{dP}{d\left[{z}/{w(z)}\right]}\Bigg|_{z=L} = R(L) \end{cases} \tag{8}$$

where the first condition sets the pressure at the opening equal to that of the gas source, and the second requires the flux at the trench bottom to equal the consumption rate by wall reactions across the bottom.

With equation (6) and boundary conditions (8), the pressure profile for an inward-tapered trench can be solved. After converting between pressure and flux, $F = P/\sqrt{2\pi mkT}$ [22] and cancelling like terms, the diffusion-reaction equation is:

$$\frac{d^2F}{d\left[{z}/{w(z)}\right]^2} - 2\cot\theta\frac{dF}{d\left[{z}/{w(z)}\right]} = \frac{3}{2}\frac{R}{\sin\theta} \tag{9}$$

with boundary conditions:

$$\begin{cases} F(0) = F_0 \\ -\frac{4}{3}\frac{dF}{d\left[{z}/{w(z)}\right]}\Bigg|_{z=L} = R(L) \end{cases} \tag{10}$$

Consider the example of an inward-tapered trench with an AR_{nom} of 10 (Fig. 3.4.a). This is a relevant situation: will continued growth under super-conformal or conformal conditions lead to seam-free filling? We will show that the diffusion and ballistic models

give results that are slightly, but significantly, different. For simplicity, assume a constant sticking probability S per wall collision, such that the reaction rate $R = S \times F$. As the taper angle θ decreases from 90° to 87.5°, the AR_{eff} increases to ~ 24 and the gas pressure at the bottom falls (Fig. 3.4.b). However, the gas transport is not simply a function of AR_{eff} due to the θ terms in Equation (9). We illustrate the difference for an AR of 24: the drop in gas pressure is *smaller* in an inward-tapered trench than in a rectangular one (Fig. 3.4.c), which helps the filling process.

3.3.2 Analysis of Critical Condition for Filling

For a feature with inward-tapered sidewalls, either superconformal or conformal coating conditions can afford complete filling[6,7]. However, the effective AR and taper angle θ evolve in a significantly different manner for those two cases. Here we calculate the evolution under the assumption that the coating thickness evolves geometrically. For example, consider a rectangular trench with AR = 9 that is partially filled under superconformal conditions (SC = 2) in order to taper the sidewalls to an angle of θ = 88.8° (Fig. 3.5.a), and the corresponding AR_{eff} increases to 20 (Fig. 3.5.c, red dot). Filling is then completed without void or seam formation using superconformal (SC = 2) or conformal (SC = 1) growth (Fig. 3.5.b, left and right, respectively). Under continued super-conformal growth, AR_{eff} increases to ~ 80, and θ decreases slightly to 88.3° as the flat bottom converts to an apex; then the AR_{eff} *falls* because the θ value continuously decreases. By contrast, for conformal growth AR_{eff} increases to ~ 110 and remains constant because the V-shape has a constant θ value (Fig. 3.5.c). If the filling method is switched to conformal growth at an earlier stage, the AR_{eff} and θ for the V shape would be

even larger. Thus, successful filling requires high performance by the coating processes: in the tapering stage, the super-conformal growth must extend to the bottom of trench with increasing AR_{eff}, which is aggressive but possible (Chapter 2); this helps to reduce the θ and AR_{eff} for the critical V shape. Then, in the filling stage the growth needs to remain super-conformal, or not less than conformal.

3.3.3 Diffusion-reaction Model of Filling

In a super-conformal process, the growth rate increases with depth in the feature up to a critical depth, and then falls. For seam-free filling, the critical depth (the peak growth rate) must not occur before the apex of the V shape. We derive the maximum depth for super-conformal MgO growth using the kinetic parameters (Chapter 2) for 7.5 and 3.0 mTorr partial pressures of $Mg(DMADB)_2$ and H_2O, respectively, at a temperature of 220 °C [23]. The maximum AR_{eff} for super-conformal coating increases from 20 when θ = 90° to ~ 90 when θ = 80° (Fig. 3.6.a).

Further insight can be gained using Eq. 7 to translate the maximum AR_{eff} into AR_{nom}, vs. θ (Fig. 3.6.b). With decreasing θ, the position of the peak growth rate approaches and then reaches the apex of the V shape (Fig. 3.6.c). We assume that defect-free filling will occurs when AR_{nom} for super-conformal growth is ≥ 0.99 that of the V shaped trench. In the diffusion model, this is the case for θ ≤ 86°, and larger values of θ are predicted to produce a defect along the centerline.

In contrast to this prediction, we have obtained complete MgO filling after a tapering stage that gave θ = 87.5° (Fig. 3.7, left). At this angle, the peak growth rate is predicted to occur at 85 – 90 % of the maximum depth of the V-shape, which is marginal.

This discrepancy between theory and experiment, although seemingly minor, is a crucial because the goal is to develop a robust criterion for defect-free filling. In fact, this discrepancy motivated us to re-examine the transport kinetics in deep features, discussed next.

3.4 Ballistic Transport

The diffusion model is known to underestimate the transport of molecules to great depths in a high AR feature [24]. This occurs because the Knudsen diffusivity assumes a single mean free path between wall collisions [20], whereas in reality, molecules that are emitted at glancing angles to the centerline of the feature will travel long distances without collision. A ballistic transport model therefore provides more accurate solutions to the critical problem of filling the apex of the V without void or seam formation.

As an illustration, for a bottomless rectangular trench with AR = 100 and a constant sticking probability S = 0.01, we simulate a delta function source of particles in the middle. The steady-state flux distributions for the diffusion and ballistic transport models are similar between positions 0 (the middle) to 7 or 8 (trench widths) (Fig. 3.8.a). Beyond that distance, the flux in the ballistic transport model is everywhere higher. At a distance of 50, for example, the flux predicted by the ballistic model is 3-4 orders of magnitude larger than that in the diffusion model (Fig. 3.8.b).

The present ballistic simulation differs from previous reports in several respects: (i) we consider inward-tapered walls, as required to afford defect-free filling; and (ii) we perform calculations under two-component, super-conformal growth conditions, which

were not known until our recent discovery [23]; (iii) we simulate the coating profile for AR_{nom}, up to 100, which is far larger than in previous studies of shallow features [24].

3.4.1 Model Description

The particle transport is calculated in 3 dimensions, then the results are projected onto a 2 dimensional cross-section. This is valid when the feature, e.g. a trench, is very long compared with its width W_0 and depth L_0, such that it can be considered semi-infinite (Fig. 3.9). For an arbitrary position i inside the trench, the total receiving flux is the sum of direct flux from outside the trench and the re-emitted flux from all other positions inside the trench that falls onto this position:

$$f_{total,i} = f_{d,i} + f_{r,i} \tag{11}$$

The direct flux $f_{d,i}$ depends on the position i, and is a constant for a defined trench shape, given a stable and uniform source distribution outside the trench. The re-emitted flux $f_{r,i}$ approaches steady state after many cycles of wall collisions and re-emission. To calculate the direct and re-emitted flux that falls onto position i, the contributions from every small area at the trench opening, and from every other position on the trench walls need to be summed up. Below, for the derivation of f_{ik}, $f_{r,i}$, and q_{ik}, we adopt the formulae and notation by Cale [25].

3.4.2 Direct Flux

For the direct flux, the gas outside the trench is regarded as an uniform and isotropic source at the trench opening; the emission across the plane of the opening

follows a cosine law [26]. From an arbitrary position k in the trench opening (Fig. 3.9), the flux that falls onto position i obeys:

$$f_{ik} = e_k \cos(\Omega_{ki})\, K_{ik} \frac{1}{\pi} \frac{\cos(\Omega_{ik})}{S_{ik}^2} \quad (12)$$

where the e_k is the total equivalent emission flux from position k. Ω_{ki} is the angle between connection of ki and k's normal. K_{ik} stands for visibility between the two positions, which equals 1 if k and i are visible to each other, otherwise 0. For our analysis here for filling of V-shape trench, K_{ik} is constantly 1. Similarly, Ω_{ik} is the angle between connection of ki and i's normal, and S_{ik} stands for the length of connection of ik. So, the last term gives the solid angle of unit area at position i to position k, and $1/\pi$ is the normalization factor. The total direct flux to position i is then:

$$f_{d,i} = \sum_k f_{ik} \quad (13)$$

As the source is uniform, the emission flux e_k is the same for all other opening positions. If we define the term q_{ik} as

$$q_{ik} = \frac{1}{\pi} K_{ik} \frac{\cos \Omega_{ik} \cos \Omega_{ki}}{S_{ik}^2} \quad (14)$$

Then, this q_{ik} term gives the fraction of emission flux from position k that hits position i, and the total direct flux to position i is an integration over all such positions on the trench opening surface:

$$f_{d,i} = \iint (e * q_{ik}) dA_k \quad (15)$$

Setting the origin at the center of the trench opening, we derived the formula for the direct flux to position i (y_i, z_i):

$$f_{d,i} = \frac{1}{2} e \times (z_0 - z_i)\{[-y_i \cos\alpha_i + (z_0 - z_i)\sin\alpha_i] \times M + \cos\alpha_i (N + y_i \times M)\} \tag{16}$$

where

$$M = \frac{y_0 - y_i}{(z_0 - z_i)^2 \sqrt{(y_0 - y_i)^2 + (z_0 - z_i)^2}} + \frac{y_0 + y_i}{(z_0 - z_i)^2 \sqrt{(y_0 + y_i)^2 + (z_0 - z_i)^2}}$$

$$N = \frac{1}{\sqrt{(y_0 + y_i)^2 + (z_0 - z_i)^2}} - \frac{1}{\sqrt{(y_0 - y_i)^2 + (z_0 - z_i)^2}}$$

Here α_i is the angle between position i's normal and the y-axis (equals zero for a rectangular trench), z_0 is the z coordinate for the opening surface (equals zero before deposition), and y_0 is the y coordinate for the trench edge at the opening.

3.4.3 Re-emitted Flux

The re-emission from an arbitrary position j inside the trench also follows a cosine distribution with respect to the local normal, as confirmed by numerical simulation for re-emission after multiple reflections in surface micro-structures [21]. The total re-emitted flux to position i is:

$$f_{r,i} = \iint (e_j * q_{ij}) dA_j \tag{17}$$

where A_j is a small area at arbitrary position j located on the trench sidewall or bottom. However, as the re-emitting flux e_j varies varies with position, and would change

as it approaches steady-state after multiple cycles of collision and re-emission, the calculation has to discretize the positions inside trench to a series of nodes.

As the trench is symmetric along the x axis, the results can be projected onto the y-z plane [25]. Then, discretizing the positions along the cross-sectional shape of the trench, the re-emitting flux that hits position *i* follows:

$$f_{r,i} = \sum_{j \neq i} e_j * q_{ij}' * l_j \tag{18}$$

where q_{ij}' is integration of q_{ij} over the *x* axis, and l_j is the length of section *j*.

Some fraction of the total flux impinging on position *i* is consumed by surface reaction to form film, and the rest is re-emitted:

$$e_i = f_{total,i} - r_i \tag{19}$$

3.4.4 Matrix Notation and Calculation for Steady-state Distribution

Based on the model described above, we develop a computationally efficient approach, which is to group the direct and reemitted fluxes for all nodes of the trench into vectors, and use a matrix to represent the transport probability between every pair of nodes:

$$F = E * Q + F_d \tag{20}$$

$$E = F - R \tag{21}$$

where *F* is a vector of receiving flux for all nodes, *E* is a vector of product of emission flux and node length, $e*l$, *Q* is the matrix of the transmission probability, q_{ij}', F_d

is a vector of direct flux, and R is the vector for the reaction rate, which can be a function of receiving flux.

The initial conditions for the model are:

$$\begin{cases} F_{t0} = F_d \\ E_{t0} = 0 \\ R_{t0} = f(F_{t0}) \end{cases} \quad (22)$$

where $F_{t0,}$ the initial receiving flux vector equals the direct flux vector (Eq. 16); E_{t0} , the initial emitting flux vector, equals zero; and the initial reaction vector R_{t0} is calculated based on $F_{t0.}$ Afterwards, the E and F can be re-calculated with each other according to Eqs. 20 and 21, until a self-consistent solution is found. When this group of equations achieves steady-state, the stable flux distribution is represented by F.

3.4.5 Constant Sticking Probability Case

In the limit of low pressure (low flux) reaction conditions, the flux and reaction rate are related by a constant sticking probability, which is the ratio of reacted flux over the total received flux:

$$R = F * S \quad (23)$$

The following self-consistent equation represents the steady-state:

$$F = F * (1 - S) * Q + F_d \quad (24)$$

Solving this equation – which implicitly contains the infinite series of internal re-emissions – we obtain:

$$F = \frac{F_d}{[1-(1-S)\cdot Q]} \tag{25}$$

Thus, *in the case of constant sticking probability, the stable flux distribution can be derived from a single equation*.

As a test of the ballistic transport model, we consider the steady-state flux distribution in a rectangular trench with AR = 10 under condition of zero sticking probability. The walls are divided into 800 nodes. Thermodynamic equilibrium requires that the flux to all surfaces be identical, no matter the incident flux distribution. The flux predicted after $2*10^5$ iterations is constant with an error of 0.5 %, which we deem acceptable (Fig. 3.10). This is the maximum possible error level for our model, considering that with higher sticking probabilities, fewer cycles of calculation are needed to reach the steady-state. The direct flux distribution at the entrance is, as expected, half that outside the trench because the each sidewall edge is exposed only to half the solid angle of the source volume.

3.5 Comparison Between the Diffusion and Ballistic Models

3.5.1 For a Constant Sticking Probability

The flux profile is calculated using the diffusion and the ballistic models, for constant sticking probabilities of 0.001, 0.01 or 0.1, in a rectangular trench of AR = 10 (Fig. 3.11, left) and in a V-shaped trench with θ = 88° (Fig. 3.11, right). For the latter, the AR_{nom} is 14.3 (Fig. 3.11). At large depth and small sticking probability (0.01 or 0.001), the flux predicted by the ballistic model is consistently higher than that by the diffusion model. This difference is particularly pronounced at the bottom of the V-shaped trench,

where the magnitude of flux is crucially important for defect-free filling. We stress that the diffusion formalism makes an unphysical assumption – constant scattering length – that is removed in the ballistic model. For this reason, we maintain that the higher fluxes are correct, and that the filling problem is more tractable than would be assumed under a diffusion simulation.

3.5.2 For Super-conformal Coating Conditions

For a wide variety of coating conditions, the sticking probability is pressure (flux) dependent because adsorption is governed by a kinetic competition for surface sites [23]. The super-conformal process (Chapter 2) takes advantage of this competition, in combination with different pressure drop gradients for the two components, to afford an increasing growth rate at depth. We first discuss how this complex dependence is handled within the diffusion and ballistic models. Note that a constant sticking probability – growth rate linearly proportional to flux – obtains only in the absence of kinetic competition. Here, sticking probability should be understood to mean a particular steady-state solution for the ratio of reaction rate to incident flux at a given depth in the feature, not a constant.

To illustrate the flux dependence, we perform calculations for the MgO CVD system using the first-order reaction model of Chapter 2 under super-conformal coating conditions, namely P(Mg(DMADB)$_2$) = 7.5 mTorr and P(H_2O) = 3.0 mTorr at a growth temperature of 220°C. At these starting pressures, the sticking probability = 0.002 for the Mg precursor, comparable in magnitude to the constant sticking probabilities discussed above. One physical complication, as discussed in Chapter 2, is that the molecules exhibit

an adsorption residence time on the growth surface. This is a distinct, weaker effect than the strong interaction of molecules onto binding sites on the film surface. This residence time adds to the molecular flight time and reduces the transport rate of the molecules in the feature by the factor:

$$K = \frac{\frac{w}{\bar{v}}}{\frac{w}{\bar{v}} + \tau_0} \tag{26}$$

where K = 0.055 and 0.038 for H_2O and $Mg(DMADB)_2$, respectively. In the diffusion model we adopt the diffusivity given by in Eq. 10 in Chapter 2, which equals the Knudsen diffusivity multiplied by the factor K. In the ballistic model all flux terms are multiplied by K; accordingly, to keep the growth rate unchanged, the adsorption coefficients are divided by K. (The rate constants k_{des} and k_r remain unchanged, and the pressure P are converted into fluxes within the k_{ads} term.) Following the procedure introduced earlier (Eqs. 20-22), convergence is reached in about $1.5*10^5$ computational cycles.

The models predict somewhat different MgO coating profiles as a function of the taper angles (Fig. 3.12). For a rectangular trench, θ = 90°, the positions of the peaks are essentially identical. As the taper angle θ is reduced (the features becomes more V-shaped), the ballistic model consistently predicts a deeper position for the peak growth rate than the diffusion model due to differences in the flux gradient. For θ = 89°, the peak still occurs above the bottom of the feature and a void space would be formed. For θ = 88°, the peak position is very close to the apex, and it may be viable (in view of the assumed bottom boundary condition) to produce void-free filling. When θ = 87°, the

diffusion model predicts a peak growth rate appreciably above the bottom, while the ballistic model predicts that the reaction rate is still increasing at the bottom.

In summary, for MgO CVD system, the normalized depth of the peak growth rate approaches unity at taper angles about 2 degrees higher in the ballistic model than in the diffusion model (Fig. 3.13). With θ increased from 86° to 88°, the maximum AR_{nom} for complete filling almost doubles, from 7.2 to 14.3. The increased θ predicted by the ballistic model is consistent with our experimental observation that complete filling can be achieved in a rectangular trench (AR 9:1 and depth over opening ratio = 11.5) that had been tapered to θ = 87.5° (Fig. 3.7).

An important question is whether the quantitative behavior exhibited by the MgO super-conformal system represents, at least qualitatively, the possibilities for void-free filling in other systems? Our response is a definite yes, based on the following considerations:

1. Super-conformal coating behavior (Chapter 2) is predicted to occur for a variety of other CVD precursors based on the reported negative differential in growth rate vs. source or co-reactant pressure, combined with a difference in the transport rates of the precursor and co-reactant due to their molecular weights.

2. The mathematical criteria for filling derived in this Chapter are general and easily extended to other systems using the diffusion model as a first estimate. The ballistic transport effect then assures that the filling of deep positions in the feature will

be better than predicted using the diffusion approximation. And of course, researchers so inclined can perform ballistic transport simulations directly.

3.6 Conclusions

We describe the opportunities and limits for filling deep features under conditions that avoid the formation of a void or seam along the centerline. To fill a rectangular trench, the sidewalls must first be tapered using conditions that afford a super-conformal thickness profile; then filling can be completed using either super-conformal or conformal conditions. Within the diffusion-reaction formalism, we derive the concept of effective AR to describe the partial pressure distribution and the reaction (growth) rate profile. For example, at a constant depth/opening ratio of 10, the effective AR increases with sidewall tapering angle θ, which decreases the precursor pressure at the bottom. We also derive the particle transport within the feature using a ballistic simulation. This approach correctly accounts for collisionless, long-range trajectories and predicts that defect-free filling will occur with less sidewall tapering than in the diffusion model. We model the super-conformal CVD of MgO as a function of sidewall taper. The ballistic transport model predicts complete filling, in agreement with experiment, whereas the diffusion model predicts seam formation. The trends found in this work are general, and the computational methodology can be used to predict the performance of any system for which the rate coefficients for the growth process are known.

3.7 References

1. P. J. Ireland, "High aspect ratio contacts: A review of the current tungsten plug process", *Thin Solid Films* **304,** 1-12 (1997).

2. M. Nandakumar, A. Chatterjee, S. Sridhar, K. Joyner, M. Rodder, I. C. Chen, and Ieee, *Shallow trench isolation for advanced ULSI CMOS technologies* (1998).

3. F. Ayazi and K. Najafi, "High aspect-ratio combined poly and single-crystal silicon (HARPSS) MEMS technology", *Journal of Microelectromechanical Systems* **9,** 288-94 (2000).

4. A. Saynatjoki, T. Alasaarela, A. Khanna, A. Tervonen, and S. Honkanen, "Mode properties of ALD filled slot waveguides," in *Silicon Photonics V*; *Vol. 7606*, edited by J. A. Kubby and G. T. Reed (2010).

5. *International Technology Roadmap for Semiconductors* (2009).

6. A. Saynatjoki, T. Alasaarela, A. Khanna, L. Karvonen, P. Stenberg, M. Kuittinen, A. Tervonen, and S. Honkanen, "Angled sidewalls in silicon slot waveguides: conformal filling and mode properties", *Optics Express* **17,** 21066-76 (2009).

7. X.-Y. Li, G.-T. Li, S. Ren, and D.-Y. Qiao, "Void-free trench isolation based on a new trench design", *Microsystem Technologies-Micro-and Nanosystems-Information Storage and Processing Systems* **19,** 757-61 (2013).

8. H. Schenk, P. Durr, D. Kunze, H. Lakner, and H. Kuck, "A resonantly excited 2D-micro-scanning-mirror with large deflection", *Sensors and Actuators a-Physical* **89,** 104-11 (2001).

9. C. Chang, T. Abe, and M. Esashi, "Trench filling characteristics of low stress TEOS/ozone oxide deposited by PECVD and SACVD", *Microsystem Technologies-Micro-and Nanosystems-Information Storage and Processing Systems* **10,** 97-102 (2004).

10. R. Abdolvand, H. Johari, G. K. Ho, A. Erbil, and F. Ayazi, "Quality factor in trench-refilled polysilicon beam resonators", *Journal of Microelectromechanical Systems* **15,** 471-8 (2006).

11. T. P. Moffat, D. Wheeler, M. D. Edelstein, and D. Josell, "Superconformal film growth: Mechanism and quantification", *IBM J. Res. Dev.* **49,** 19-36 (2005).

12. D. Josell, D. Wheeler, and T. P. Moffat, "Gold superfill in submicrometer trenches: Experiment and prediction", *Journal of the Electrochemical Society* **153,** C11-C8 (2006).

13. D. Josell, C. Burkhard, Y. Li, Y. W. Cheng, R. R. Keller, C. A. Witt, D. R. Kelley, J. E. Bonevich, B. C. Baker, and T. P. Moffat, "Electrical properties of superfilled sub-micrometer silver metallizations", *J. Appl. Phys.* **96,** 759-68 (2004).

14. H. Kim, H. B. R. Lee, and W. J. Maeng, "Applications of atomic layer deposition to nanofabrication and emerging nanodevices", *Thin Solid Films* **517,** 2563-80 (2009).

15. B. C. Baker, C. Witt, D. Wheeler, D. Josell, and T. P. Moffat, "Superconformal silver deposition using KSeCN derivatized substrates", *Electrochem. Solid State Lett.* **6,** C67-C9 (2003).

16. T. P. Moffat, J. E. Bonevich, W. H. Huber, A. Stanishevsky, D. R. Kelly, G. R. Stafford, and D. Josell, "Superconformal electrodeposition of copper in 500-90 nm features", *Journal of the Electrochemical Society* **147,** 4524-35 (2000).

17. Y. Au, Y. B. Lin, and R. G. Gordon, "Filling narrow trenches by iodine-catalyzed CVD of copper and manganese on manganese nitride barrier/adhesion layers", *Journal of the Electrochemical Society* **158,** D248-D53 (2011).

18. S. G. Pyo, S. Kim, D. Wheeler, T. P. Moffat, and D. Josell, "Seam-free fabrication of submicrometer copper interconnects by iodine-catalyzed chemical vapor deposition", *J. Appl. Phys.* **93,** 1257-61 (2003).

19. D. Josell, S. Kim, D. Wheeler, T. P. Moffat, and S. G. Pyo, "Interconnect fabrication by superconformal iodine- catalyzed chemical vapor deposition of copper", *Journal of the Electrochemical Society* **150,** C368-C73 (2003).

20. J. R. Welty, *Fundamentals of Momentum, Heat, and Mass Transfer*, 5 ed. (Wiley, Hoboken, N. J., 2008).

21. R. Feres and G. Yablonsky, "Knudsen's cosine law and random billiards", *Chemical Engineering Science* **59,** 1541-56 (2004).

22. J. A. Venables, *Introduction to Surface and Thin Film Processes* (Cambridge University Press, United Kingdom, 2000).

23. W. B. Wang, N. N. Chang, T. A. Codding, G. S. Girolami, J. R. Abelson, "Superconformal chemical vapor deposition of thin films in deep features", *Journal of Vacuum Science & Technology A* **32,** 051512 (2014).

24. M. K. Jain, T. S. Cale, and T. H. Gandy, "Comparison of LPCVD film conformalities predicted by ballistic transport-reaction and continuum diffusion-reaction models", *Journal of the Electrochemical Society* **140,** 242-7 (1993).

25. T. S. Cale and G. B. Raupp, "A unified line-of-sight model of deposition in rectangular trenches", *Journal of Vacuum Science & Technology B* **8,** 1242-8 (1990).

26. R. G. Leon I. Maissel, *Handbook of Thin Film Technology* (McGraw-Hill, 1983).

3.8 Figures

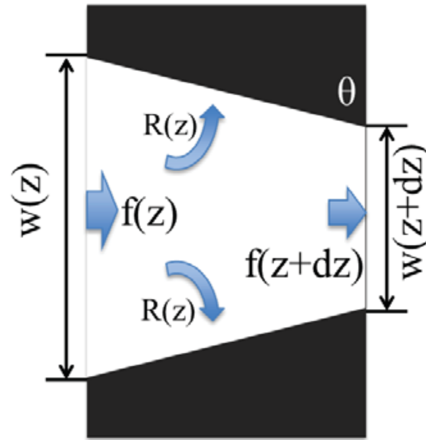

Figure 3.1. Schematic showing of a segment of inward-inclined sidewall trench with tilting angle θ. Both the flux and the trench width are decreasing when gas molecules transport through this segment, and the decreased amount is equal to the consumption by reaction on the sidewall, whose length is dz / sinθ.

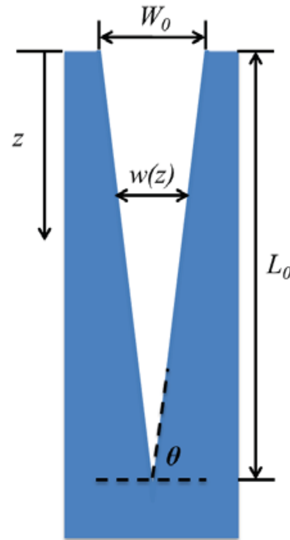

$$P_{eff} = \int_0^z \frac{dz}{w(z)} = \frac{\tan\theta}{2} \ln\left(\frac{\tan\theta/2}{\tan\theta/2 - z/W_0}\right)$$

Figure 3.2. The effective position for a V-shape trench with wall incline angle θ equals the integral of the depth increment over the local width. The formula blows up for $z = L_0$, but that mathematical singularity is not present in the ballistic transport formulation (below).

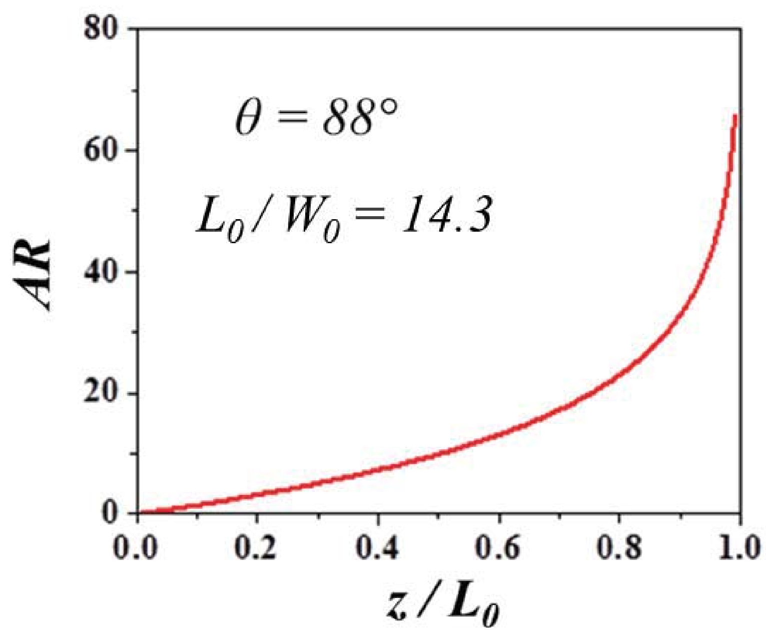

Figure 3.3. The effective AR vs. depth up to 99% of the apex at L_0, for a V-shaped trench with $\theta = 88°$.

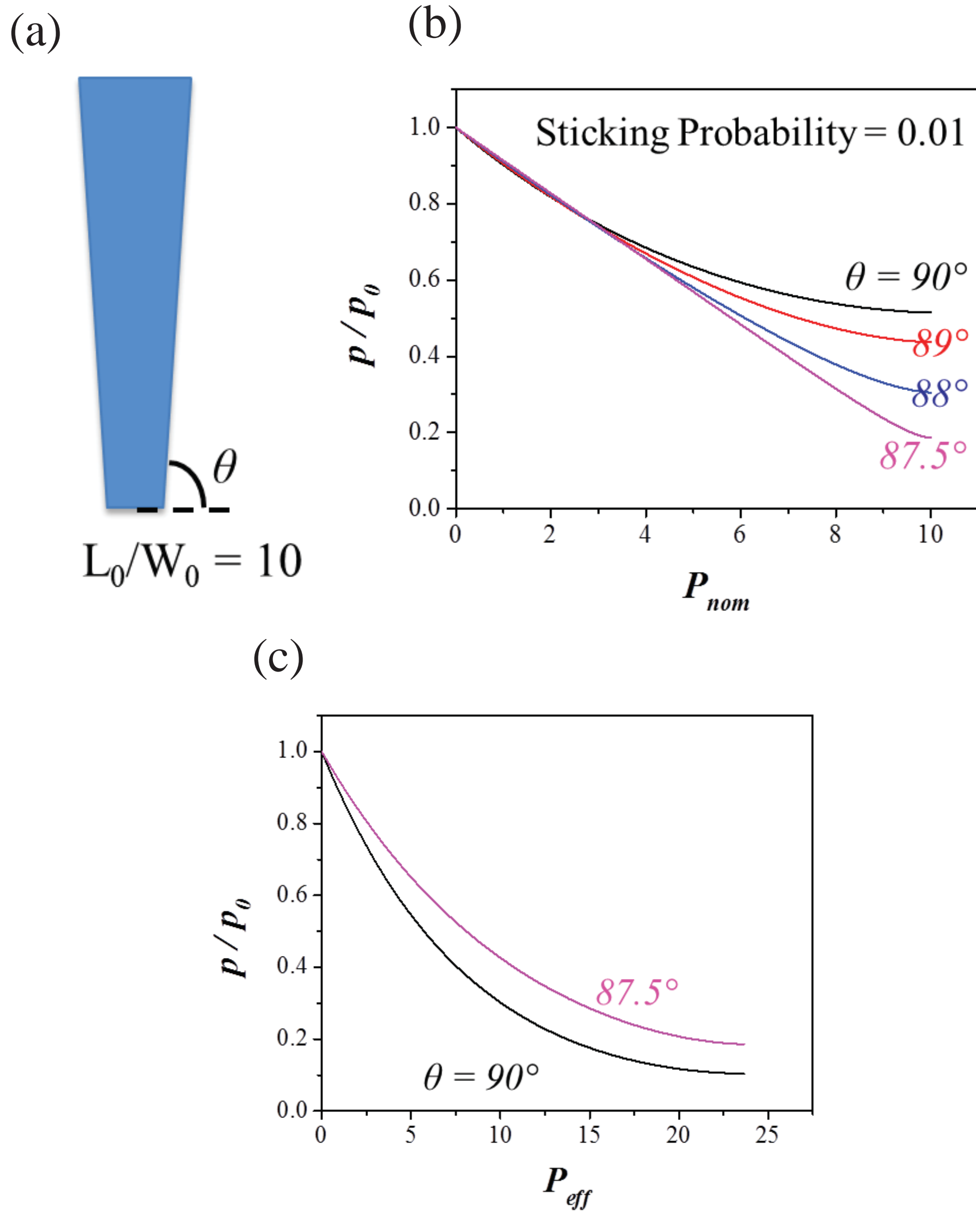

Figure 3.4. (a) Schematic of a trench with inward-tapered sidewalls for $L_0/W_0 = 10$; the taper angle θ_s can vary. (b) During film growth, the decrease in precursor pressure vs. depth in the trench as a function of taper angle θ_s, for a wall reaction probability of 0.01. (c) Pressure drop profiles for an effective AR 24 with taper angle $\theta_s = 87.5°$ or 90°.

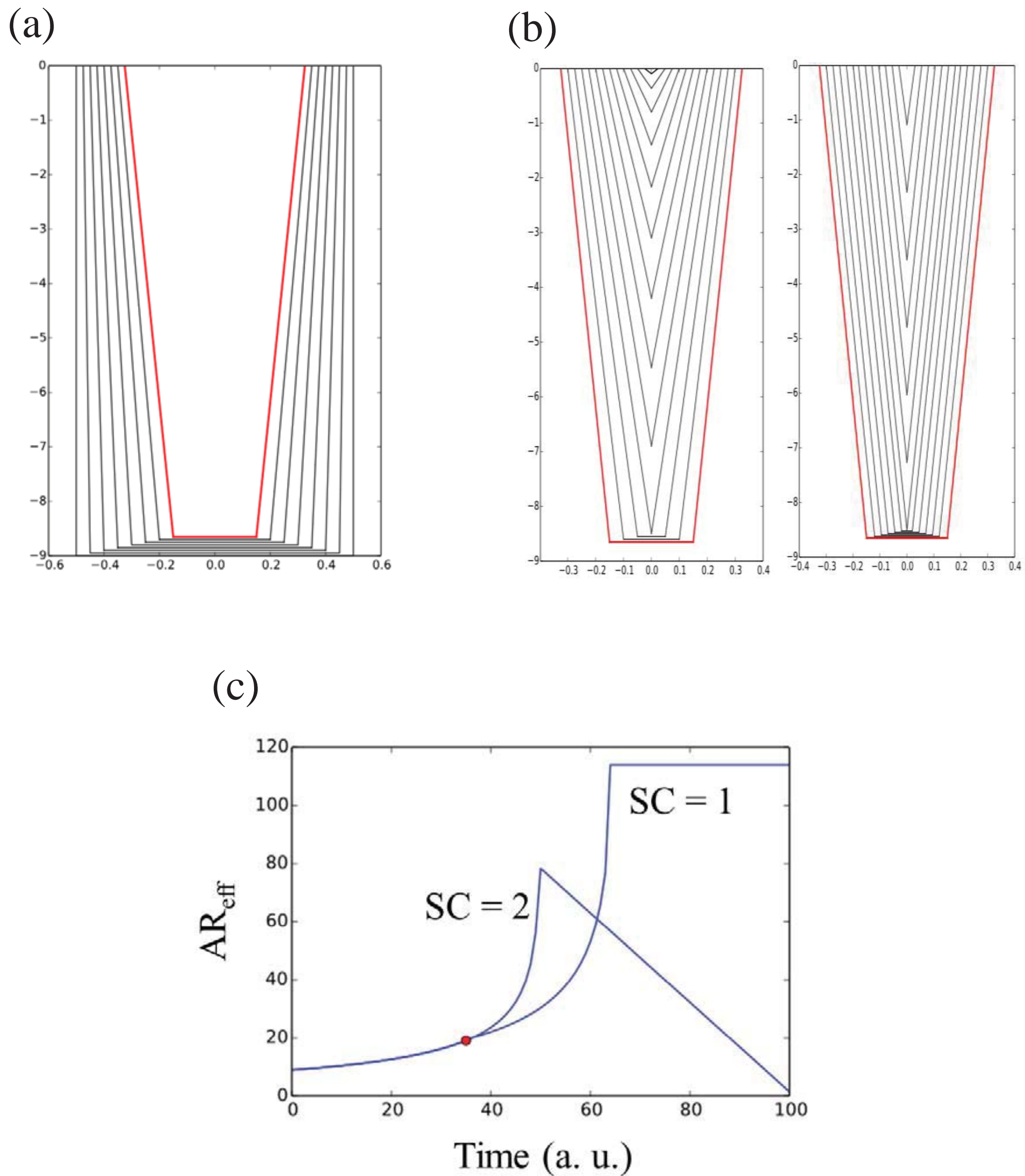

Figure 3.5. Simulated trench coating profiles with increment in coating thickness; note the different length scales for the width and depth (see text for details). (a) Conversion of a rectangular trench with AR = 9 to one with taped sidewalls using super-conformal coating with SC = 2. (b) Continued filling of the trench in a. using super-conformal coating (SC = 2, left), or conformal coating (SC = 1, right), up to complete filling. (c) The effective AR for the conditions in b. throughout the filling process. The red dot indicates the effective AR after the first stage (a).

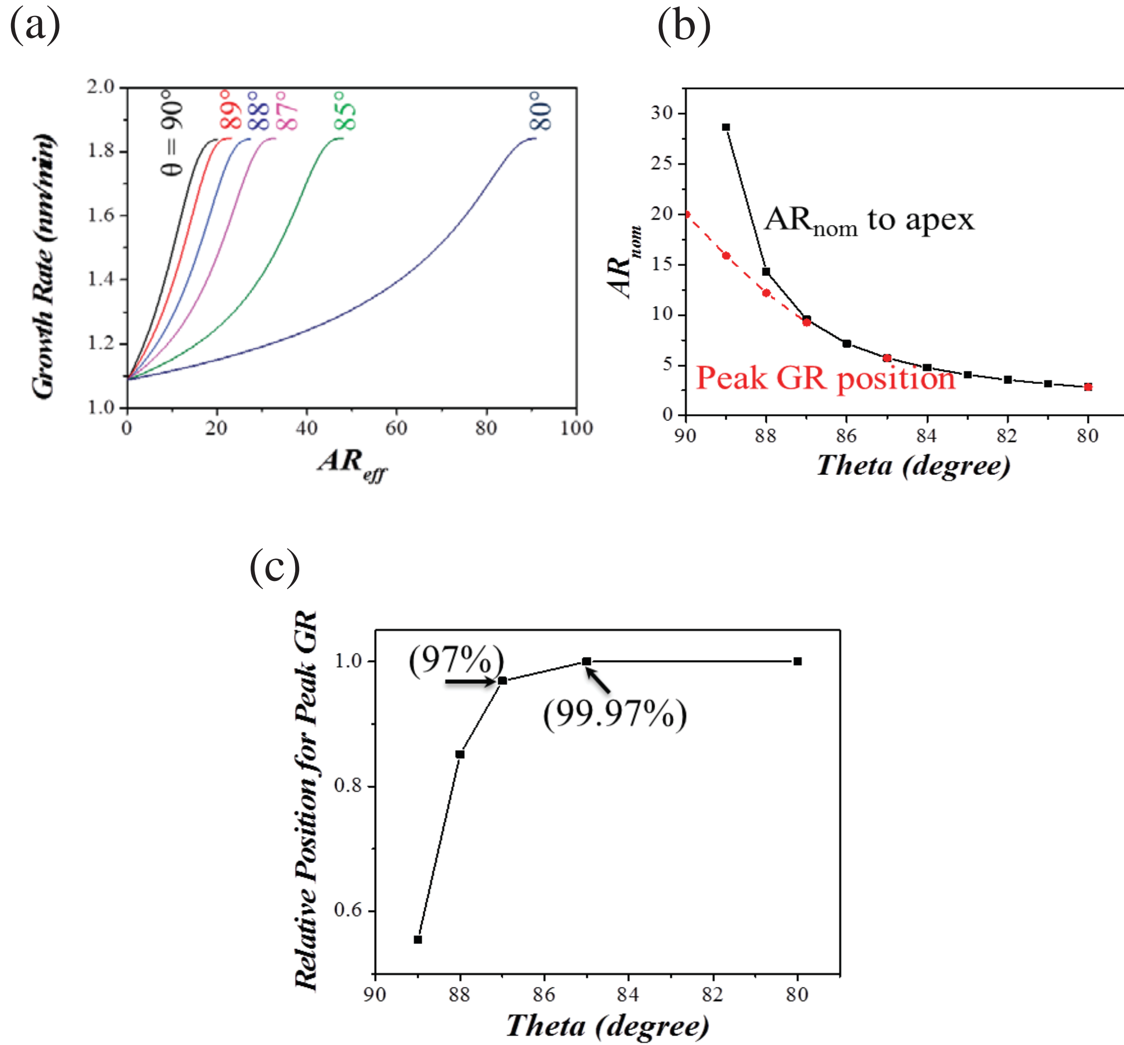

Figure 3.6. (a) Calculated maximum effective ARs in which super-conformal coating can occur in a V-shape trench as a function of θ_s. Kinetic parameters correspond to CVD of MgO using co-reactants Mg(DMADB)$_2$ (7.5 mTorr) and H_2O (3.0 mTorr) at 220 °C. (b) Comparison between normalized position for peak growth rate (as converted from AR_{eff} using Eq. 7) and the normalized AR for a V-shaped trench with different θs. (c) The maximum relative position for peak growth rate down to the apex of the V-shape trenches. Values ≥ 99 % can afford seam-free filling, hence a taper angle ≤ 86° is required.

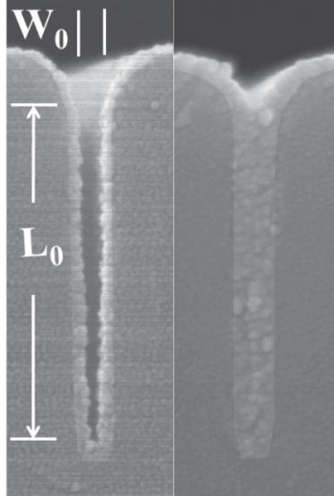

Figure 3.7. SEM cross-sectional images of a trench with AR = 9 at two stages of filling with MgO under super-conformal conditions. A V-shaped coating (left) leads to complete filling (right).

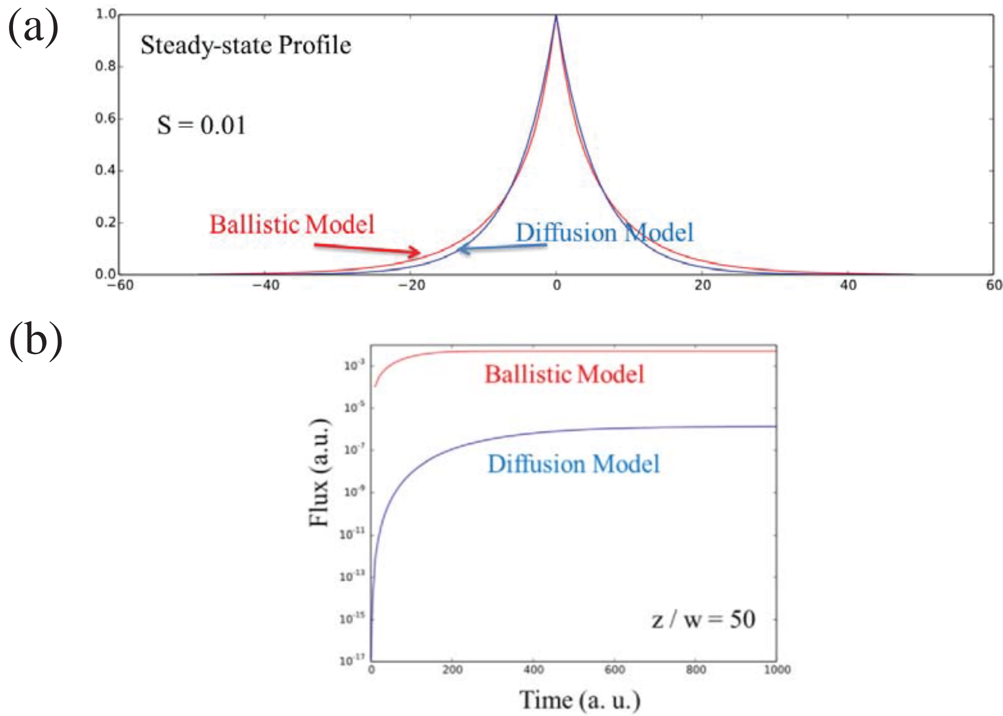

Figure 3.8. (a) Comparison between diffusion-reaction model and ballistic transport model for estimation of steady-state flux distribution for a bottomless rectangular trench with AR of 100. It is assumed that emission is a delta function at position 0, and sticking probability is a constant, 0.01. (b) Time evolution of the flux values at z/w = 50 by the two models, showing 3-4 orders of magnitude larger value by ballistic transport model at steady state.

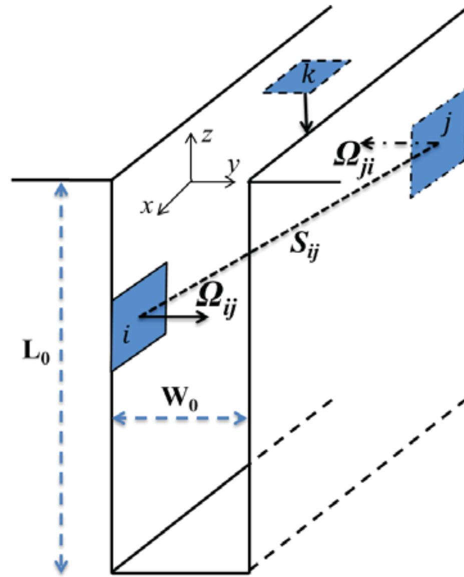

Figure 3.9. Coordinate system xyz for a rectangular trench with width W_0, depth L_0, and infinite length. In the calculations, the 3-dimensional fluxes are projected onto a 2-dimensional cross-section. The flux falling on position *i* is found by integration over all elements connected to *i* by a solid angle. Representative small areas on the sidewall and the opening surface are labeled as j and k; arrows indicate the local normal directions. Ω_{ij} and Ω_{ji} are the angles formed by the connection between *i* and *j* with respect to the local normals. S_{ij} is the length of the connection between *i* and *j*.

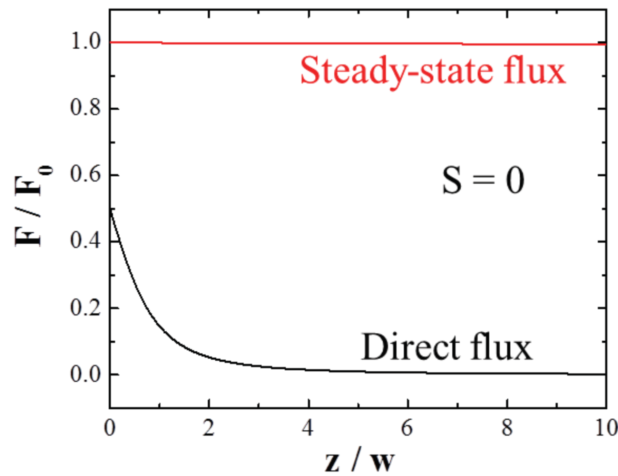

Figure 3.10. Ballistic transport simulation of the direct flux and steady-state flux distributions in a rectangular trench with AR = 10, under the condition of zero sticking probability. The result that the steady-state flux is almost unity everywhere indicates that the ballistic model includes enough particle trajectories to approach the thermodynamic limit.

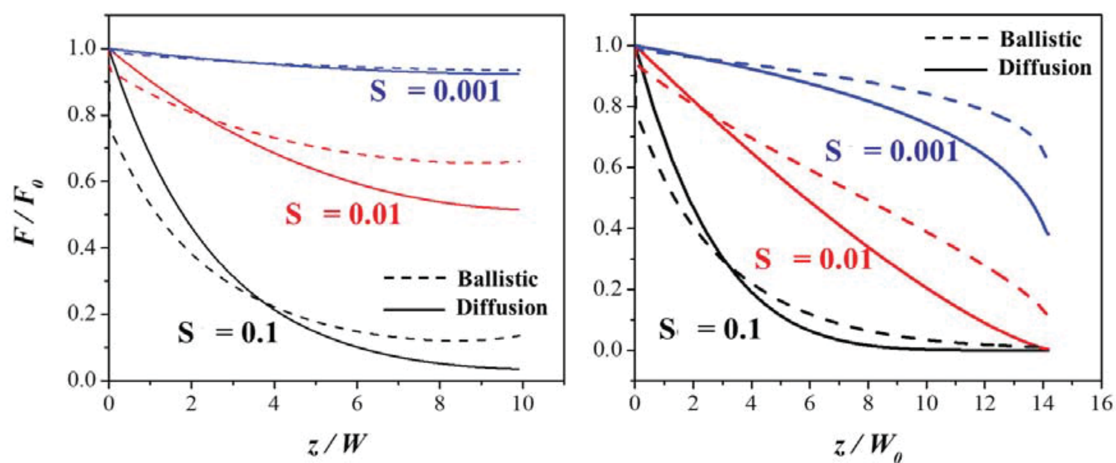

Figure 3.11. Normalized particle fluxes calculated using the diffusion-reaction model or the ballistic transport-reaction model inside a trench of AR =10 for θ = 90° (left) or 88° (right), for sticking probability S = 0.1, 0.01, or 0.001. At large z, the diffusion model underestimates the local flux and thus the possibility of seam-free filling.

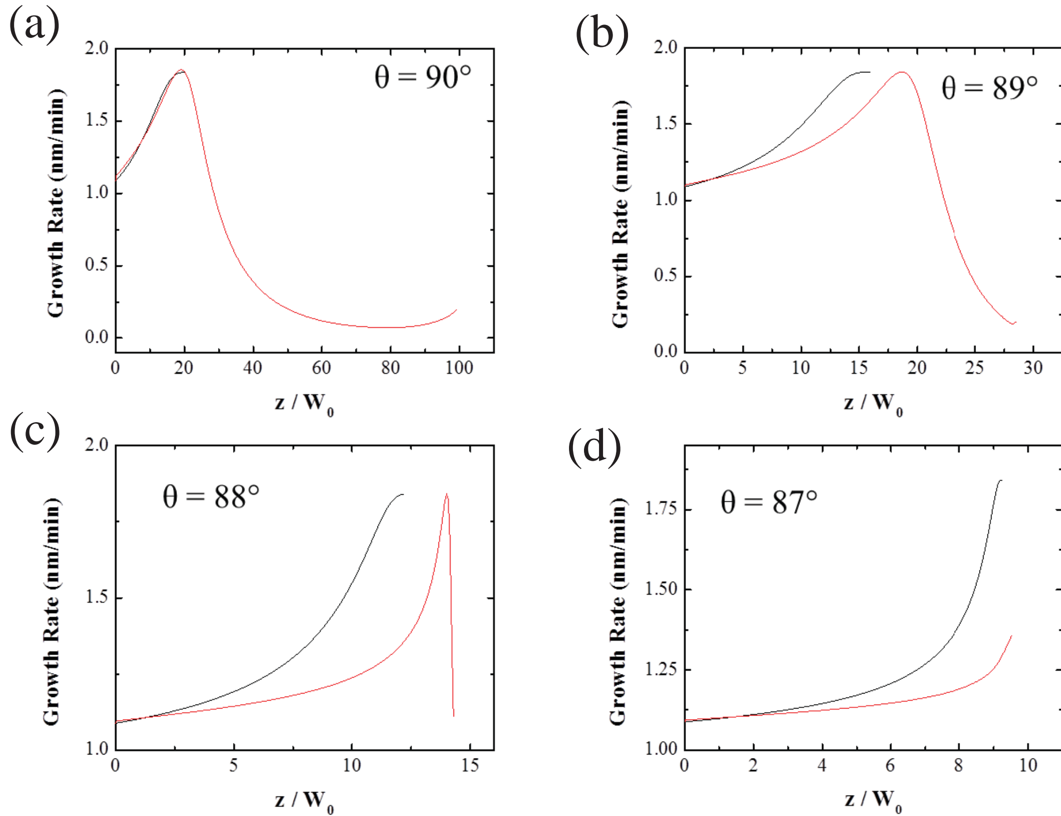

Figure 3.12. Comparison of the growth rate profiles using two-molecule CVD model for MgO with P[Mg(DMADB)$_2$] = 7.5 mTorr and P(H_2O) = 3.0 mTorr, at growth temperature 220°C, as described in Chapter 2. The growth rate profiles are estimated by diffusion reaction model (black line) and ballistic transport model (red line), for rectangular trench (a), and for V-shape trench with θ = 89° (b), 88° (c), and 87° (d). The fluxes in ballistic transport model are adjusted by the factor K, as discussed in text. For the diffusion-reaction model, the maximum depth for super-conformal coating is set as a boundary condition (deeper profiles are not shown). For θ = 90°, AR = 100 is used to illustrate the challenge of filling very deep features.

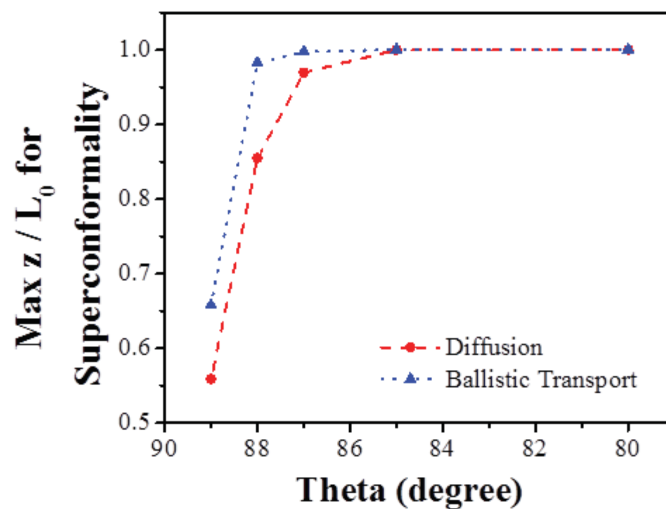

Figure 3.13. Summary plot for MgO CVD system: the maximum depth for super-conformal growth as a function of taper angle θ predicted by the diffusion-reaction model or the ballistic transport-reaction model. The diffusion approximation requires $\theta \leq 86°$; the more accurate ballistic simulation requires $\theta \leq 88°$ which is significantly easier to achieve experimentally.

CHAPTER 4

RE OXIDE CVD WITH RE(DMADB)$_3$ PRECURSORS AND WATER

4.1 Introduction

Rare earth (RE) oxides have been actively studied for various applications, such as serving as potential substitute for SiO_2 gate dielectric [1-7] or as optical coatings [8], due to their high dielectric constants (~12-14) [9,10], high break-down voltage [11], and outstanding transparency across a wide range of frequencies [12]. RE doping is also very important in illumination applications, because of their unique electronic energy level structures [13-19].

To manufacture RE oxide films, the method typically utilized is physical vapor deposition (PVD). There are reports of thermal or e-beam evaporation of RE oxide powder onto various substrates [20-22], and the resultant film is amorphous or crystalline [3], depending on the conditions used. However, PVD is not good at coating for structures with AR larger than ~ 7 [23]. ALD and CVD provide a solution for uniform coating on 3-dimensional structures. A series of RE precursors with 2,2,6,6-tetramethyl-3,5-heptanedione (thd) ligand is commercially available, and their CVD or ALD growth behavior with ozone or oxygen plasma as the oxygen source has been reported [24-34]. For several RE elements, there are also carbon- or nitrogen- coordinated precursors available for reaction with water as co-reactant [24,35-38].

Recently, the group of Prof. G. S. Girolami synthesized new precursors for every lanthanide element except Eu and Yb using the DMADB ligand [39]. These precursors are promising to afford RE oxide films by CVD method using water as co-reactant, similar to results for the Mg and Ti analogues [40]. Here we report the growth and film properties for the Tm, Er, and Y compounds; we expect that the other precursors will have similar properties.

4.2 Experiment

The chamber is a cold wall CVD system, equipped with spectroscopic ellipsometry, as introduced in Chapter 1. The substrate is single-side polished n-type Si (100) covered with native oxide. After ultrasonic cleaning with acetone, isopropyl alcohol and DI water, the substrate is dried with flowing N_2 then loaded into the chamber. The precursors used are $Y(DMADB)_3$, $Er(DMADB)_3$, and $Tm(DMADB)_3$ [39]. These molecules are stored in separate glass containers in the form of fine powders showing greenish, pink, and white colors under sunlight for Tm, Er, and Y, respectively. The precursors can be stored in room temperature for months without noticeable degradation. Ar (flow rate 20-50 sccm) is used as a carrier gas for RE precursors (but not for the Mg compound). The precursor delivery line inside the growth chamber is 7 cm away and perpendicular to the substrate, to increase the local flux. Deionized (DI) water is injected as a background pressure of 0.1 - 0.7 mTorr (not as a directed flux), to serve as the oxygen source. During growth, the Er, Tm, and Y precursor containers are heated to 110 °C. The substrate temperature ranges from 200 – 550 °C. Er doping into Y_2O_3, and Tm doping into MgO are obtained by co-flowing the precursors for dopant and host material.

Film thickness and microstructure are studied with SEM, and film composition is determined by RBS.

4.3 Result and Discussion

4.3.1 Growth Kinetics

The CVD for these oxides is flux limited due to the low vapor pressure of the precursor molecules. We determined the reaction without and with the co-reactant present. At substrate temperatures above 300 °C the $Y(DMADB)_3$ precursor self-decomposes on the surface, forming a compound of Y, B, and possibly N. Adding H_2O has almost no effect on the high temperature reaction rate. Below 300 °C, the self-decomposition rate is undetectable with in-situ SE. In the presence of water at substrate temperatures of 200 – 300 °C, oxide film is deposited at a rate of ~ 0.2 Å/min.

For the Er and Tm compounds, self-decomposition is not detected at substrate temperatures up to 550 °C. In the presence of water, neither precursor initially reacts on the Si substrate, presumably due to very slow nucleation at low precursor flux. However, if a MgO layer is first deposited on the substrate, then erbium oxide and thulium oxide can be deposited, with no nucleation delay, at a rate of ~ 0.2 Å/min for all substrate temperatures.

4.3.2 Film Morphology

Cross-sectional SEM images reveal a uniform (featureless) structure for a 20 nm thick yttrium oxide film deposited at 300 °C, and for a 30 nm thick Er oxide film on MgO

layer deposited at 270 °C (Fig. 4.2). At higher growth temperatures, the surface of Er oxide becomes rough, presumably due to crystallization and faceting.

4.3.3 Film Composition

For Er and Y oxide films, XPS reveals a B content up to ~ 10 at. % when a low water pressure (< 0.5 mTorr) is used. For Tm oxide, as the Tm 4d peak is located at the same position as the B 1s peak, the B content level cannot be accurately determined. Other possible impurities, including C and N, are not detectable. For yttrium oxide deposition, at a water pressure ≥ 0.5 mTorr, the B content decreases to ≤ 5 at. %. The compositions for Y and O are ~ 57 at. % and 39 at. %, respectively, consistent with a film stoichiometry of Y_2O_3.

4.3.4 RE Doping

Since these precursors as based on the same DMADB ligand, it is plausible that doping RE atoms into oxide hosts will be straightforward. The doping of Tm into MgO and of Er into Y_2O_3 have been studied.

Tm doping in MgO is realized by co-flow of $Tm(DMADB)_3$ and $Mg(DMADB)_2$ in the presence of H_2O at 320 °C. In the middle of the deposition, the Tm precursor is switched off for 3 minutes out of total growth time of 10 minutes. In-situ ellipsometry reveals film thicknesses, from the substrate up, of 60 nm with Tm co-flowing, 50 nm without, and 50 nm with Tm co-flow again. The Tm concentration profile has peak values at the top surface and at the substrate interface (Fig. 4.3). Tm in MgO exhibits an apparent solubility limit of about 0.04 at. % as measured independently by RBS.

Er doping into Y_2O_3 is realized by co-flowing $Er(DMADB)_3$ and $Y(DMADB)_3$ together with water. Er has a similar atomic size as Y, and the oxides for these two elements shares the same crystalline structure [41], hence, the oxides are mutually soluble over the entire composition range [42]. To control the Er density, the precursor container temperature is varied. When both precursor containers are heated to 110 °C, the Er:Y ratio in the mixed oxide is ~ 1:1 according to RBS. When Er precursor is at room temperature, and the Y precursor maintained at 110 °C, the Er:Y ratio is ~ 1:2.7 (Fig. 4.4). To utilize Er as a luminescent center, its concentration should be further reduced to ~ 0.1 – 2 at. % [41]. This can be accomplished by decreasing the carrier gas flow rate or the source temperature for the Er precursor.

4.4 Conclusion

A series of $RE(DMADB)_3$ precursors that were recently invented are tested for CVD growth with water as the co-reactant at 200 - 300 °C. Yttrium oxide and erbium oxide have been successfully deposited onto Si (100) substrate and onto MgO, respectively, at a similar growth rate around 0.2 nm/min. The yttrium oxide is found to have the composition of Y_2O_3, contaminated with ~ 4.4 at. % of B when a water $\geq$ 0.5 mTorr is used. With lower water pressures, the B composition increases, up to 10 at. %. The doping of Tm into MgO, and Er into Y_2O_3 is achieved by co-flowing the precursors for dopant and oxide host. The doping level of Tm in MgO is limited by its solubility, which is about 0.04 at. %, as evaluated by SIMS and RBS. Er doping in Y_2O_3 is achieved with varying Er:Y ratio of 1:1 to 1:2.7, by changing the sublimation of the Er precursor.

4.5 References

1. M. Roeckerath, J. M. J. Lopes, E. D. Ozben, C. Urban, J. Schubert, S. Mantl, Y. Jia, and D. G. Schlom, "Investigation of terbium scandate as an alternative gate dielectric in fully depleted transistors", *Appl. Phys. Lett.* **96** (2010).

2. R. Thomas, P. Ehrhart, M. Luysberg, M. Boese, R. Waser, M. Roeckerath, E. Rije, J. Schubert, S. Van Elshocht, and M. Caymax, "Dysprosium scandate thin films as an alternate amorphous gate oxide prepared by metal-organic chemical vapor deposition", *Appl. Phys. Lett.* **89** (2006).

3. J. Kwo, M. Hong, A. R. Kortan, K. L. Queeney, Y. J. Chabal, R. L. Opila, D. A. Muller, S. N. G. Chu, B. J. Sapjeta, T. S. Lay, J. P. Mannaerts, T. Boone, H. W. Krautter, J. J. Krajewski, A. M. Sergnt, and J. M. Rosamilia, "Properties of high kappa gate dielectrics Gd_2O_3 and Y_2O_3 for Si", *Journal of Applied Physics* **89,** 3920-7 (2001).

4. M. Leskela and M. Ritala, "Rare-earth oxide thin films as gate oxides in MOSFET transistors", *Journal of Solid State Chemistry* **171,** 170-4 (2003).

5. L. Niinisto, J. Paivasaari, J. Niinisto, M. Putkonen, and M. Nieminen, "Advanced electronic and optoelectronic materials by Atomic Layer Deposition: An overview with special emphasis on recent progress in processing of high-k dielectrics and other oxide materials", *Physica Status Solidi a-Applied Research* **201,** 1443-52 (2004).

6. G. Scarel, E. Bonera, C. Wiemer, G. Tallarida, S. Spiga, M. Fanciulli, I. L. Fedushkin, H. Schumann, Y. Lebedinskii, and A. Zenkevich, "Atomic-layer deposition of Lu_2O_3", *Appl. Phys. Lett.* **85,** 630-2 (2004).

7. C. Zhao, T. Witters, B. Brijs, H. Bender, O. Richard, M. Caymax, T. Heeg, J. Schubert, V. V. Afanas'ev, A. Stesmans, and D. G. Schlom, "Ternary rare-earth metal oxide high-k layers on silicon oxide", *Appl. Phys. Lett.* **86** (2005).

8. S. Thakur, N. K. Sahoo, M. Senthilkumar, and R. B. Tokas, "Optical properties and morphological changes in gadolinia films deposited under ambient substrate temperature conditions", *Optical Materials* **27,** 1402-9 (2005).

9. A. Feteira, L. J. Gillie, R. Elsebrock, and D. C. Sinclair, "Crystal structure and dielectric properties of $LaYbO_3$", *J. Am. Ceram. Soc.* **90,** 1475-82 (2007).

10. S. P. Pavunny, R. Thomas, A. Kumar, N. M. Murari, and R. S. Katiyar, "Dielectric properties and electrical conduction of high-k $LaGdO_3$ ceramics", *Journal of Applied Physics* **111** (2012).

11. S. P. Pavunny, R. Thomas, N. M. Murari, J. Schubert, V. Niessen, R. Luptak, T. S. Kalkur, and R. S. Katiyar, "Structural and electrical properties of lanthanum gadolinium oxide: ceramic and thin films for high-k application", *Integr. Ferroelectr.* **125,** 44-52 (2011).

12. M. P. Singh, C. S. Thakur, K. Shalini, S. Banerjee, N. Bhat, and S. A. Shivashankar, "Structural, optical, and electrical characterization of gadolinium oxide films deposited by low-pressure metalorganic chemical vapor deposition", *Journal of Applied Physics* **96,** 5631-7 (2004).

13. H. Zhou, G. Wu, N. Qin, and D. Baow, "Dual enhancement of photoluminescence and ferroelectric polarization in Pr^{3+}/La^{3+}-codoped bismuth titanate thin films", *J. Am. Ceram. Soc.* **93,** 2109-12 (2010).

14. A. Polman, "Erbium implanted thin film photonic materials", *Journal of Applied Physics* **82,** 1-39 (1997).

15. M. Ishii, T. Ishikawa, T. Ueki, S. Komuro, T. Morikawa, Y. Aoyagi, and H. Oyanagi, "The optically active center and its activation process in Er-doped Si thin film produced by laser ablation", *Journal of Applied Physics* **85,** 4024-31 (1999).

16. K. Takahei and A. Taguchi, "Efficient er luminescence-centers formed in gaas by metalorganic chemical-vapor-deposition with oxygen codoping", *Japanese Journal of Applied Physics Part 1-Regular Papers Short Notes & Review Papers* **33,** 709-11 (1994).

17. A. Conde-Gallardo, M. Garcia-Rocha, I. Hernandez-Calderon, and R. Palomino-Merino, "Photoluminescence properties of the Eu^{3+} activator ion in the TiO_2 host matrix", *Appl. Phys. Lett.* **78,** 3436-8 (2001).

18. S. Bachir, C. Sandouly, J. Kossanyi, and J. C. RonfardHaret, "Rare earth-doped polycrystalline zinc oxide electroluminescent ceramics", *Journal of Physics and Chemistry of Solids* **57,** 1869-79 (1996).

19. S. Lange, V. Kiisk, V. Reedo, M. Kirm, J. Aarik, and I. Sildos, "Luminescence of RE-ions in HfO_2 thin films and some possible applications", *Optical Materials* **28,** 1238-42 (2006).

20. T. Wiktorczyk, "Rare earth oxide films: their preparation and characterization", *Optica Applicata* **31,** 5-33 (2001).

21. H. Ono and T. Katsumata, "Interfacial reactions between thin rare-earth-metal oxide films and Si substrates", *Appl. Phys. Lett.* **78,** 1832-4 (2001).

22. V. Mikhelashvili, G. Eisenstein, and F. Edelmann, "Characteristics of electron-beam-gun-evaporated Er_2O_3 thin films as gate dielectrics for silicon", *Journal of Applied Physics* **90,** 5447-9 (2001).

23. J. E. Crowell, "Chemical methods of thin film deposition: Chemical vapor deposition, atomic layer deposition, and related technologies", *J. Vac. Sci. Technol. A* **21,** S88-S95 (2003).

24. M. Putkonen, M. Nieminen, J. Niinisto, and L. Niinisto, "Surface-controlled deposition of Sc_2O_3 thin films by atomic layer epitaxy using beta-diketonate and organometallic precursors", *Chem. Mat.* **13,** 4701-7 (2001).

25. M. Putkonen, T. Sajavaara, L. S. Johansson, and L. Niinisto, "Low-temperature ALE deposition of Y_2O_3 thin films from beta-diketonate precursors", *Chem. Vapor Depos.* **7,** 44-50 (2001).

26. E. P. Gusev, E. Cartier, D. A. Buchanan, M. Gribelyuk, M. Copel, H. Okorn-Schmidt, and C. D'Emic, "Ultrathin high-K metal oxides on silicon: processing, characterization and integration issues", *Microelectronic Engineering* **59,** 341-9 (2001).

27. T. T. Van and J. P. Chang, "Surface reaction kinetics of metal beta-diketonate precursors with O radicals in radical-enhanced atomic layer deposition of metal oxides", *Applied Surface Science* **246,** 250-61 (2005).

28. M. Nieminen, M. Putkonen, and L. Niinisto, "Formation and stability of lanthanum oxide thin films deposited from beta-diketonate precursor", *Applied Surface Science* **174,** 155-65 (2001).

29. H. Molsa and L. Niinisto, "Deposition of cerium dioxide thin-films on silicon substrates by atomic layer epitaxy", in *Metal-Organic Chemical Vapor Deposition of Electronic Ceramics*; *Vol. 335*, edited by S. B. Desu, D. B. Beach, B. W. Wessels, and S. Gokoglu (1994), p. 341-50.

30. J. Paivasaari, M. Putkonen, and L. Niinisto, "Cerium dioxide buffer layers at low temperature by atomic layer deposition", *J. Mater. Chem.* **12,** 1828-32 (2002).

31. J. Paivasaari, M. Putkonen, and L. Niinisto, "A comparative study on lanthanide oxide thin films grown by atomic layer deposition", *Thin Solid Films* **472,** 275-81 (2005).

32. A. Kosola, J. Paivasaari, M. Putkonen, and L. Niinisto, "Neodymium oxide and neodymium aluminate thin films by atomic layer deposition", *Thin Solid Films* **479,** 152-9 (2005).

33. J. Niinisto, N. Petrova, M. Putkonen, L. Niinisto, K. Arstila, and T. Sajavaara, "Gadolinium oxide thin films by atomic layer deposition", *Journal of Crystal Growth* **285,** 191-200 (2005).

34. J. Paivasaari, M. Putkonen, T. Sajavaara, and L. Niinisto, "Atomic layer deposition of rare earth oxides: erbium oxide thin films from beta-diketonate and ozone precursors", *Journal of Alloys and Compounds* **374,** 124-8 (2004).

35. J. Niinisto, M. Putkonen, and L. Niinisto, "Processing of Y_2O_3 thin films by atomic layer deposition from cyclopentadienyl-type compounds and water as precursors", *Chem. Mat.* **16,** 2953-8 (2004).

36. B. S. Lim, A. Rahtu, and R. G. Gordon, "Atomic layer deposition of transition metals", *Nature Materials* **2,** 749-54 (2003).

37. R. G. Gordon, J. Becker, D. Hausmann, and S. Suh, "Vapor deposition of metal oxides and silicates: Possible gate insulators for future microelectronics", *Chem. Mat.* **13,** 2463-4 (2001).

38. D. H. Triyoso, R. I. Hegde, J. Grant, P. Fejes, R. Liu, D. Roan, M. Ramon, D. Werho, R. Rai, L. B. La, J. Baker, C. Garza, T. Guenther, B. E. White, and P. J. Tobin, "Film properties of ALD HfO_2 and La_2O_3 gate dielectrics grown on Si with various pre-deposition treatments", *Journal of Vacuum Science & Technology B* **22,** 2121-7 (2004).

39. S. R. Daly, D. Y. Kim, and G. S. Girolami, "Lanthanide N,N-dimethylaminodiboranates as a new class of highly volatile chemical vapor deposition precursors", *Inorganic Chemistry* **51,** 7050-65 (2012).

40. W. B. Wang, Y. Yang, A. Yanguas-Gil, N. N. Chang, G. S. Girolami, and J. R. Abelson, "Highly conformal magnesium oxide thin films by low-temperature chemical vapor deposition from $Mg(H_3BNMe_2BH_3)_2$ and water", *Appl. Phys. Lett.* **102** (2013).

41. R. Salhi, R. Maalej, M. Fourati, Y. Guyot, O. Chaix-Pluchery, L. Rapenne, C. Jimenez, and J.-L. Deschanvres, "Influence of deposition conditions on the optical properties of erbium-doped yttrium oxide films grown by aerosol-UV assisted MOCVD", *Journal of Luminescence* **131,** 2311-6 (2011).

42. T. T. Van, J. R. Bargar, and J. P. Chang, "Er coordination in Y_2O_3 thin films studied by extended x-ray absorption fine structure", *Journal of Applied Physics* **100** (2006).

4.6 Figures

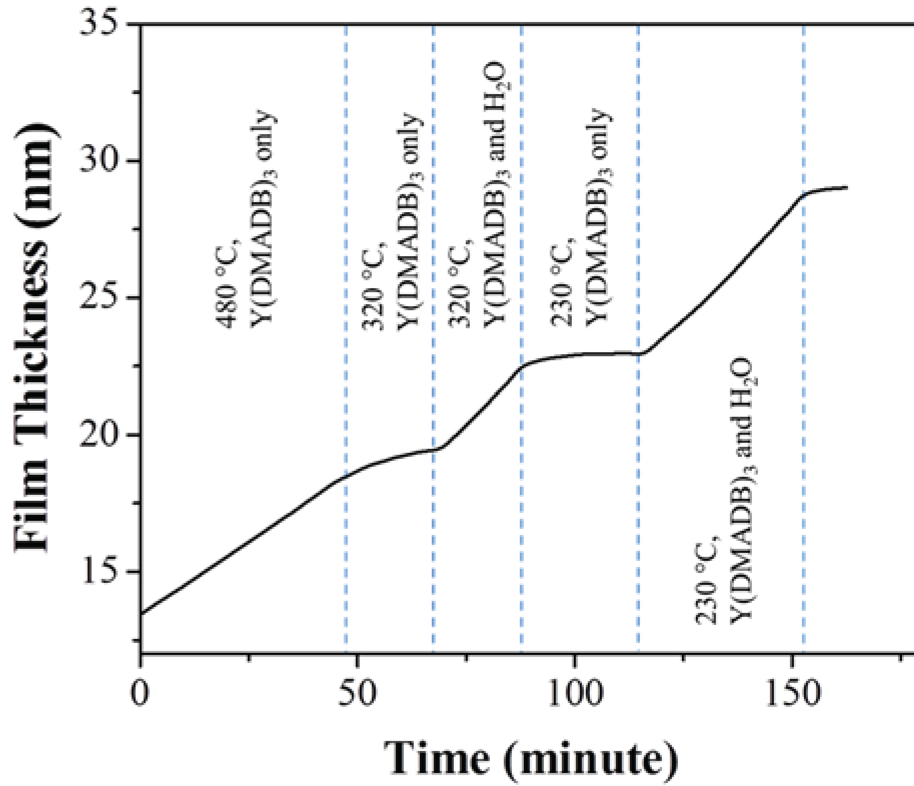

Figure 4.1. Growth of film from $Y(DMADB)_3$ without and with water co-reactant at different temperatures on a Si (100) substrate. $Y(DMADB)_3$ self decomposes slowly at 320 and rapidly at 480 °C. At 230 and 320 °C, $Y(DMADB)_3$ reacts with water to afford film at ~ 0.2 nm/minute.

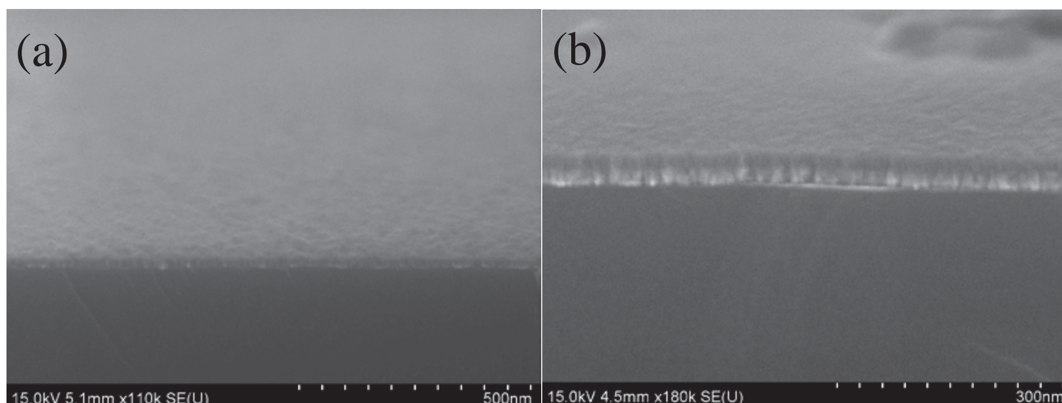

Figure 4.2. Cross-sectional SEM images for (a) Y oxide on Si(100) substrate, and (b) Er oxide on MgO on Si(100) substrate.

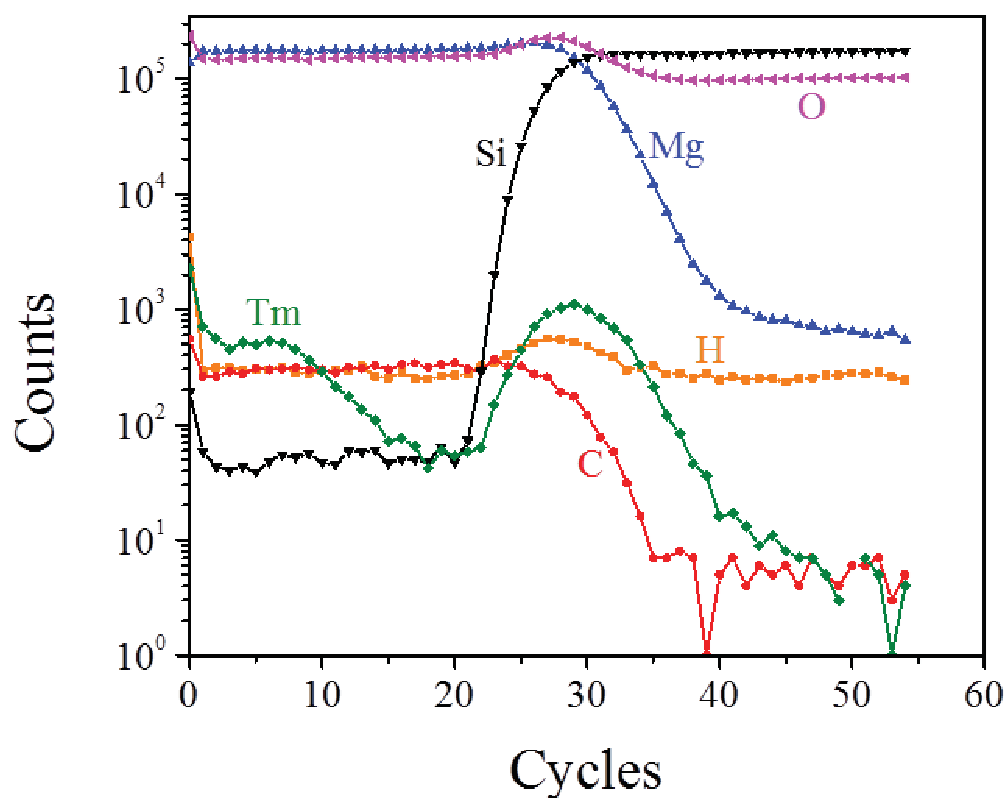

Figure 4.3. SIMS for MgO with layers of Tm doping. Real-time spectroscopic ellipsometry during film growth indicated, from the Si substrate up, layer thicknesses of 60 nm with $Tm(DMADB)_3$ co-flow, 50 nm without, and 50 nm with co-flow again. Tm in MgO exhibits an apparent solubility limit of about 0.04 at. % as measured independently by RBS.

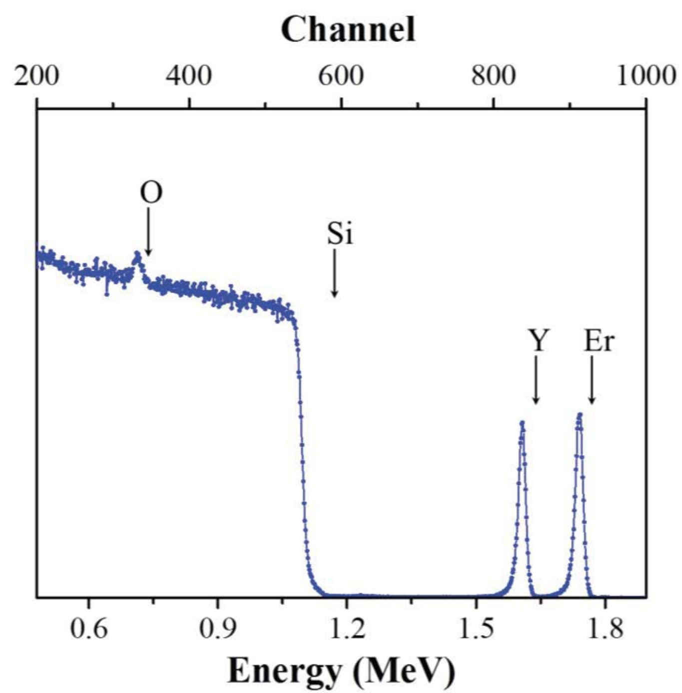

Figure 4.4. RBS spectrum for Er doping into Y_2O_3, deposited on a Si(100) substrate, with surface energy positions noted. Based on the integrated area covered by the peaks, the Er : Y ratio is 1 : 2.7.

CHAPTER 5

CVD OF TiO_2 THIN FILMS AT LOW-TEMPERATURE FROM $Ti(DMADB)_2$ AND WATER

5.1 Introduction

Titanium dioxide, TiO_2, is a useful material owing to its photocatalytic properties and exceptional chemical stability in aqueous environments [1]. When irradiated with ultraviolet light, it is able to split water and generate H_2 [2-7], to degrade organic pollutants in water purification processes [8-10], to act as a self-cleaning surface [11-13], and to perform other useful catalytic reactions [14]. Photocatalytic activity with visible light can be achieved by coating TiO_2 with dyes [15] or doping it with various heteroatoms [16]. In addition, the high dielectric constant of the rutile phase, ~ 80, makes TiO_2 an attractive capacitor [17] and gate dielectric [18] material.

TiO_2 coatings can be deposited by sol-gel [19], magnetron sputtering [20], chemical vapor deposition (CVD) [21], and atomic layer deposition (ALD) [22,23] processes. We focus on the latter two because they are most amenable to conformal deposition. Interestingly, the catalytic properties of TiO_2 are often enhanced if it is prepared as a mixture of the anatase and rutile phases rather than as a single phase material [24-27]. The ability of various CVD and ALD precursors to afford mixed phase TiO_2 has been investigated as a function of film thickness [26], co-reactant pressure [28], and temperature (Table 5.1). For example, the precursors $TiCl_4$ and TiI_4 afford mixed

phase films at ~ 325°C; for most other precursors, the deposition temperature to obtain mixed phase films (as opposed to amorphous or single-phase material) is typically ~ 600-700°C.

Here I report the deposition of TiO_2 films by CVD from a recently synthesized precursor, $Ti(DMADB)_2$, where DMADB = *N*,*N*-dimethylaminodiboranate ($H_3BNMe_2BH_3^-$) [29]. This precursor is a solid with a vapor pressure of 0.01 - 0.1 Torr at 25°C (estimated by comparison of the sublimation rate with those of other volatile compounds). The magnesium analog $Mg(DMADB)_2$ reacts cleanly with water under CVD conditions to form MgO with liberation H_2 and volatile *N*,*N*-dimethylaminodiborane ($B_2H_5NMe_2$) [30]. I will show that a similar reaction of $Ti(DMADB)_2$ with water affords an attractive, halogen-free route for the growth of high quality TiO_2 films at temperatures as low as 150°C, and mixed phase oxide at 350 - 450°C, similar to $TiCl_4$ and TiI_4.

5.2 Experiment

The $Ti(DMADB)_2$ precursor is synthesized as previously described [29].

Film deposition is carried out in a cold wall high vacuum system [31] with a base pressure of 10^{-8} Torr, most of which is H_2 [32]. The substrates are single crystalline n-type Si (100) covered with ~ 2 nm of native oxide and heated directly by passage of a dc current. The precursor and water are stored in separate glass tubes and enter the chamber through separate stainless steel tubes that are nearly perpendicular to and 7 cm away from the substrate holder. Both source containers are kept at room temperature during deposition. No carrier gas is used with the precursor. A capacitance manometer measures

the average total pressure inside the chamber, which is lower than the effective pressures of reactants that effuse from the tubes and impinge on the substrate surface.

Film thickness is measured in-situ by spectroscopic ellipsometry. The reference dielectric function is determined by ex-situ variable angle spectroscopic ellipsometry on identically-prepared material. Ellipsometry values are within ± 5 % of those measured by post-growth SEM. The film phases are determined using XRD in the θ-2θ geometry. The film stoichiometry is analyzed by RBS and the impurity content by XPS and AES. The XPS spectra are energy calibrated using the C 1s peak at 284.6 eV.

5.3 Results and Discussion

5.3.1 Composition

The composition of films grown from the $Ti(DMADB)_2$ precursor depends on the deposition conditions. When no water is used as a co-reactant, the precursor decomposes on the growth surface at temperatures > 300°C to afford deposits containing mostly titanium and boron. With sufficient water partial pressure, high purity TiO_2 can be obtained. For representative conditions, e.g., a precursor pressure of ~ 0.01 mTorr, a water pressure of 2.0 mTorr, and a growth temperature of 350°C, the total content of B, C and N is < 1 at. % (Fig. 5.1, inset).

A strong C 1s peak is seen for the air-exposed surface, but disappears after Ar^+ sputtering, indicating that the bulk is carbon-free. Peaks due to B, C and N are undetectable on a survey scan. In high resolution spectra, very weak signals for the N 1s and B 1s peaks are observed, accounting for no more than 0.5 at. % each. The O 1s

binding energy is 529.9 eV, and the Ti $2p_{1/2}$ and $2p_{3/2}$ peaks have binding energies of 464.2 and 458.5 eV, respectively. The XPS data agree very well with the reported values for TiO_2 but not with those for other oxidation states [33]. Additional small features in high-resolution scans indicate trace amounts of suboxides or defect states (Supplementary Materials).

5.3.2 Growth Kinetics

At a substrate temperature of 150-450 °C, the growth rate is ~ 1.2 nm/min and is only weakly temperature dependent. However, with increasing water partial pressure, the growth rate steadily decreases (Fig. 5.2). The reduction of the growth rate at higher water pressures is attributed to a shift of the competitive adsorption equilibria on the growth surface to a water-rich condition, away from the ratio that affords maximum rate [34]. This behavior has the advantage that it can lead to films that are highly conformal [34]. We previously reported a kinetic study of competitive adsorption and its effect on growth rate for a similar system, the growth of MgO films using $Mg(DMADB)_2$ and H_2O; for that system, the data fit well to a first-order adsorption-reaction model [35].

5.3.3 Microstructure and Crystallinity

Films deposited at 400 °C are continuous and dense (Fig. 5.3). The surface roughness results from crystallization and faceting at this growth temperature.

TiO_2 films deposited at 350 and 450°C show preferred orientations for the anatase (004) and rutile (210) planes, indicated by the major peaks at 38° and 44° (Fig. 5.4). The rutile to anatase ratio increases at higher growth temperature. Additional small peaks occur in positions corresponding to reported suboxides [36], but a precise match is not

obvious; we interpret that preferred orientation or defect states are responsible. Overall, the data indicate that CVD from Ti(DMADB)$_2$ and H_2O affords mixed phase TiO_2 films at a relatively low temperatures, 350-450°C. Similar results can be achieved using $TiCl_4$ or TiI_4 as the precursor [37,38], but the current method has the advantage of avoiding the presence of halogens.

5.4 Conclusion

A recently synthesized precursor, Ti(DMADB)$_2$, reacts with H_2O to afford TiO_2 films by CVD at modest temperatures. With sufficient water pressure, the films are stoichiometric with a total impurity content < 1 at. %. Films grown at substrate temperatures of 350-450°C consist of a mixture of anatase and rutile; the rutile content increases with temperature. The film growth rate is weakly dependent on temperature, and the pressure dependence of the growth rate is consistent with competitive adsorption of the Ti precursor and water on the growth surface. The Ti(DMADB)$_2$ - H_2O system may be of technological interest due to the ready formation of mixed phase material at low temperature from a highly volatile halogen-free precursor.

5.5 References

1. A. Enesca, L. Andronic, A. Duta, and S. Manolache, "Optical properties and chemical stability of WO_3 and TiO_2 thin films photocatalysts", *Romanian Journal of Information Science and Technology* **10,** 269-77 (2007).

2. A. Fujishima and K. Honda, "Electrochemical photolysis of water at a semiconductor electrode", *Nature* **238,** 37-+ (1972).

3. D. A. Tryk, A. Fujishima, and K. Honda, "Recent topics in photoelectrochemistry: achievements and future prospects", *Electrochim. Acta* **45,** 2363-76 (2000).

4. M. Ni, M. K. H. Leung, D. Y. C. Leung, and K. Sumathy, "A review and recent developments in photocatalytic water-splitting using TiO_2 for hydrogen production", *Renew. Sust. Energ. Rev.* **11,** 401-25 (2007).

5. J. H. Park, S. Kim, and A. J. Bard, "Novel carbon-doped TiO_2 nanotube arrays with high aspect ratios for efficient solar water splitting", *Nano Lett.* **6,** 24-8 (2006).

6. G. K. Mor, K. Shankar, M. Paulose, O. K. Varghese, and C. A. Grimes, "Enhanced photocleavage of water using titania nanotube arrays", *Nano Lett.* **5,** 191-5 (2005).

7. S. U. M. Khan, M. Al-Shahry, and W. B. Ingler, "Efficient photochemical water splitting by a chemically modified n-TiO_2", *Science* **297,** 2243-5 (2002).

8. J. M. Herrmann, "Heterogeneous photocatalysis: fundamentals and applications to the removal of various types of aqueous pollutants", *Catal. Today* **53,** 115-29 (1999).

9. W. Zhao, W. H. Ma, C. C. Chen, J. C. Zhao, and Z. G. Shuai, "Efficient degradation of toxic organic pollutants with Ni_2O_3/TiO_2-xBx under visible irradiation", *J. Am. Chem. Soc.* **126,** 4782-3 (2004).

10. H. Lachheb, E. Puzenat, A. Houas, M. Ksibi, E. Elaloui, C. Guillard, and J. M. Herrmann, "Photocatalytic degradation of various types of dyes (Alizarin S, Crocein Orange G, Methyl Red, Congo Red, Methylene Blue) in water by UV-irradiated titania", *Appl. Catal. B-Environ.* **39,** 75-90 (2002).

11. A. Fujishima, X. T. Zhang, and D. A. Tryk, "TiO_2 photocatalysis and related surface phenomena", *Surf. Sci. Rep.* **63,** 515-82 (2008).

12. T. Watanabe, A. Nakajima, R. Wang, M. Minabe, S. Koizumi, A. Fujishima, and K. Hashimoto, "Photocatalytic activity and photoinduced hydrophilicity of titanium dioxide coated glass", *Thin Solid Films* **351,** 260-3 (1999).

13. I. P. Parkin and R. G. Palgrave, "Self-cleaning coatings", *J. Mater. Chem.* **15,** 1689-95 (2005).

14. X. Chen and S. S. Mao, "Titanium dioxide nanomaterials: synthesis, properties, modifications, and applications", *Chemical Reviews* **107,** 2891-959 (2007).

15. B. Oregan and M. Gratzel, "A low-cost, high-efficiency solar-cell based on dye-sensitized colloidal TIO_2 films", *Nature* **353,** 737-40 (1991).

16. S. Livraghi, M. C. Paganini, E. Giamello, A. Selloni, C. Di Valentin, and G. Pacchioni, "Origin of photoactivity of nitrogen-doped titanium dioxide under visible light", *J. Am. Chem. Soc.* **128,** 15666-71 (2006).

17. S. K. Kim, W. D. Kim, K. M. Kim, C. S. Hwang, and J. Jeong, "High dielectric constant TiO_2 thin films on a Ru electrode grown at 250 degrees C by atomic-layer deposition", *Appl. Phys. Lett.* **85,** 4112-4 (2004).

18. D. A. Deen, J. G. Champlain, and S. J. Koester, "Multilayer HfO_2/TiO_2 gate dielectric engineering of graphene field effect transistors", *Appl. Phys. Lett.* **103,** - (2013).

19. J. G. Yu, X. J. Zhao, and Q. N. Zhao, "Effect of surface structure on photocatalytic activity of TiO_2 thin films prepared by sol-gel method", *Thin Solid Films* **379,** 7-14 (2000).

20. P. Zeman and S. Takabayashi, "Nano-scaled photocatalytic TiO_2 thin films prepared by magnetron sputtering", *Thin Solid Films* **433,** 57-62 (2003).

21. S. Seifried, M. Winterer, and H. Hahn, "Nanocrystalline titania films and particles by chemical vapor synthesis", *Chemical Vapor Deposition* **6,** 239-44 (2000).

22. M. Ritala, M. Leskela, E. Nykanen, P. Soininen, and L. Niinisto, "Growth of titanium-dioxide thin-films by atomic layer epitaxy", *Thin Solid Films* **225,** 288-95 (1993).

23. J. Aarik, A. Aidla, V. Sammelselg, T. Uustare, M. Ritala, and M. Leskela, "Characterization of titanium dioxide atomic layer growth from titanium ethoxide and water", *Thin Solid Films* **370,** 163-72 (2000).

24. R. G. Nair, S. Paul, and S. K. Samdarshi, "High UV/visible light activity of mixed phase titania: A generic mechanism", *Sol. Energy Mater. Sol. Cells* **95,** 1901-7.

25. M. Maeda and T. Watanabe, "Visible light photocatalysis of nitrogen-doped titanium oxide films prepared by plasma-enhanced chemical vapor deposition", *J. Electrochem. Soc.* **153,** C186-C9 (2006).

26. M. L. Kaariainen, T. O. Kaariainen, and D. C. Cameron, "Titanium dioxide thin films, their structure and its effect on their photoactivity and photocatalytic properties", *Thin Solid Films* **517,** 6666-70 (2009).

27. R. Su, R. Bechstein, L. So, R. T. Vang, M. Sillassen, B. Esbjornsson, A. Palmqvist, and F. Besenbacher, "How the anatase-to-rutile ratio influences the photoreactivity of TiO_2", *Journal of Physical Chemistry C* **115,** 24287-92 (2011).

28. D. G. Syarif, A. Miyashita, T. Yamaki, T. Sumita, Y. Choi, and H. Itoh, "Preparation of anatase and rutile thin films by controlling oxygen partial pressure", *Appl. Surf. Sci.* **193,** 287-92 (2002).

29. L. M. Perez, M. B. Hall, C. Beddie, D. Y. Kim, and G. S. Girolami, "INOR 274-Diboranamides: A new class of chelating ligands for transition metals - $M(H_3BNMe_2BH_3)_2$, M = Ti, Cr, Mn, and Mo", *Abstr. Pap. Am. Chem. Soc.* **235,** 274-INOR (2008).

30. W. B. Wang, Y. Yang, A. Yanguas-Gil, N. N. Chang, G. S. Girolami, and J. R. Abelson, "Highly conformal magnesium oxide thin films by low-temperature chemical vapor deposition from $Mg(H_3BNMe_2BH_3)_2$ and water", *Appl. Phys. Lett.* **102** (2013).

31. S. Jayaraman, Y. Yang, D. Y. Kim, G. S. Girolami, and J. R. Abelson, "Hafnium diboride thin films by chemical vapor deposition from a single source precursor", *J. Vac. Sci. Technol. A* **23,** 1619-25 (2005).

32. D. M. Hoffman, *Handbook Of Vacuum Science and Technology* (Academic Press, San Diego, 1998).

33. E. McCafferty and J. P. Wightman, "Determination of the concentration of surface hydroxyl groups on metal oxide films by a quantitative XPS method", *Surf. Interface Anal.* **26,** 549-64 (1998).

34. A. Yanguas-Gil, N. Kumar, Y. Yang, and J. R. Abelson, "Highly conformal film growth by chemical vapor deposition. II. Conformality enhancement through growth inhibition", *J. Vac. Sci. Technol. A* **27,** 1244-8 (2009).

35. W. B. Wang, Noel N. Chang, T. A. Codding, G. S. Girolami, J. R. Abelson, "Superconformal chemical vapor deposition of thin films in deep features", *J. Vac. Sci. Technol. A* **32,** 051512 (2014).

36. T. Ioroi, H. Kageyama, T. Akita, and K. Yasuda, "Formation of electro-conductive titanium oxide fine particles by pulsed UV laser irradiation", *Physical Chemistry Chemical Physics* **12,** 7529-35 (2010).

37. K. Kukli, M. Ritala, M. Schuisky, M. Leskela, T. Sajavaara, J. Keinonen, T. Uustare, and A. Harsta, "Atomic layer deposition of titanium oxide from TiI_4 and H_2O_2", *Chemical Vapor Deposition* **6,** 303-10 (2000).

38. S. Hayashi and T. Hirai, "Chemical vapor-deposition of rutile films", *J. Cryst. Growth* **36,** 157-64 (1976).

39. C. A. Chen, Y. S. Huang, W. H. Chung, D. S. Tsai, and K. K. Tiong, "Raman spectroscopy study of the phase transformation on nanocrystalline titania films prepared via metal organic vapour deposition", *J. Mater. Sci.-Mater. Electron.* **20,** 303-6 (2009).

40. R. Tu and T. Goto, "High temperature stability of anatase films prepared by MOCVD", *Mater. Trans.* **49,** 2040-6 (2008).

41. F. Ando, H. Shimizu, I. Kobayashi, and M. Okada, "Synthesis of $Ti(DPM)_2(OCH_3)_2$ and evaluation of the TiO_2 films prepared by metal-organic chemical vapor deposition", *Jpn. J. Appl. Phys. Part 1 - Regul. Pap. Short Notes Rev. Pap.* **36,** 5820-4 (1997).

42. C. J. Taylor, D. C. Gilmer, D. G. Colombo, G. D. Wilk, S. A. Campbell, J. Roberts, and W. L. Gladfelter, "Does chemistry really matter in the chemical vapor deposition of titanium dioxide? Precursor and kinetic effects on the microstructure of polycrystalline films", *J. Am. Chem. Soc.* **121,** 5220-9 (1999).

5.6 Tables and Figures

Table 5.1. Comparison between TiO2 precursors for CVD (or ALD as labeled).

Precursor and co-reactant	T_{source} (°C)	T_{sub} (°C)	Growth Rate (nm/min)	Impurities (at. %)	T_{sub} and Phase[a]	Ref.
Ti(O-*i*-Pr)$_4$ or Ti(O-*i*-Pr)$_4$/O_2	170	350-1200	0.1-3000	C (< 1) Si (< 1)	350- α 400-A 700-A/R 1000-R	[21]
TiO(acac)$_2$/O_2	170	550-680			550-A 620-A/R 680-R	[39]
Ti(O-*i*-Pr)$_2$(dpm)$_2$/O_2	150	300-900	13-500	C (3)	300-450-A 450-800-A/R	[40]
TiI_4/H_2O_2	105-110	230-490 (ALD)	0.03-0.12 nm/cycle	H (0.05-0.9)	275-A 325-A/R 425-R	[37]

(Table 5.1 cont.)

$Ti(dpm)_2(OCH_3)_2/O_2$	90	350-650	0.5-7.0			[41]
$Ti(O$-*i*-$Pr)_4$	50-60	323-920	0.15-3.3		323-650-A 700-920-R	[42]
$Ti(NO_3)_4$	50-60	159-900	0.3-5.7		159-650-A 700-920-R	[42]
$TiCl_4/H_2O$	20	100-900			100-200- α 300- α /A/R 400-900-R	[38]
$Ti(DMADB)_2/H_2O$	25	150-450	1.0-1.3	B, N ($\leq$ 0.5)	350-450 -A/R	This work

[a] (α = amorphous, A = anatase, R = rutile)

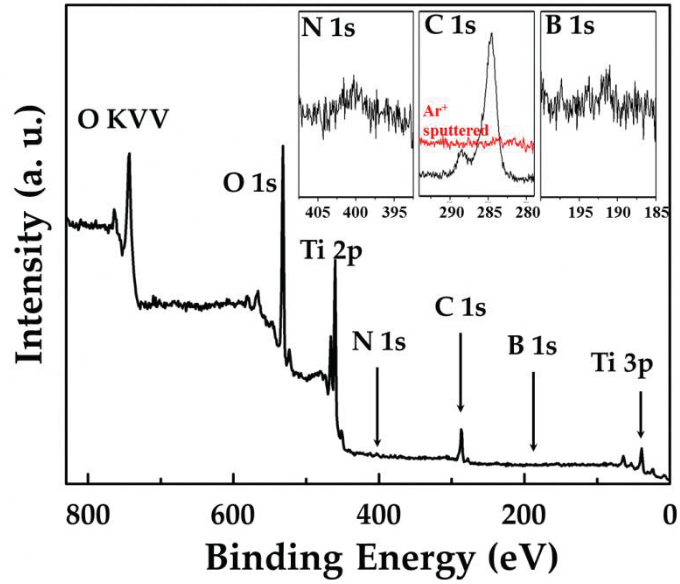

Figure 5.1. XPS survey scan spectra for TiO_2 film grown on Si(100) from $Ti(DMADB)_2$ and water at 350°C. Inset: high resolution scans for N 1s, C 1s (including the spectrum after Ar^+ sputtering), and B 1s regions, respectively.

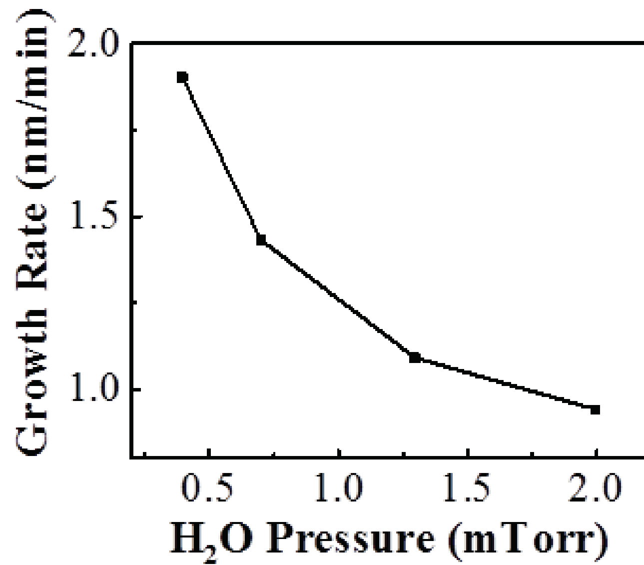

Figure 5.2. TiO_2 growth rate from $Ti(DMADB)_2$ and water as a function of water pressure.

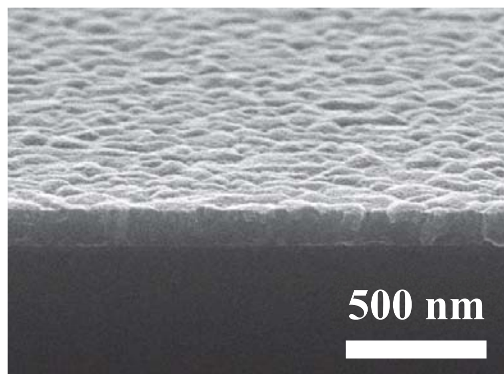

Figure 5.3. Cross-sectional SEM image of a TiO_2 film grown from $Ti(DMADB)_2$ and water at 400 °C.

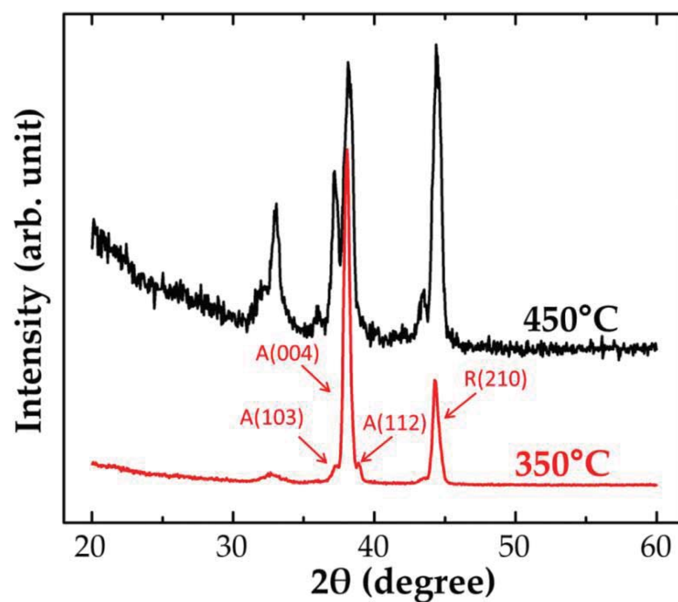

Figure 5.4. XRD for TiO_2 film deposited from $Ti(DMADB)_2$ and water at 350°C (red) and 450°C (black), on Si(100) substrates. The anatase peaks are labeled with A, the rutile peaks with R. The peak at 33° is due to the Si substrate.

Supplemental material:

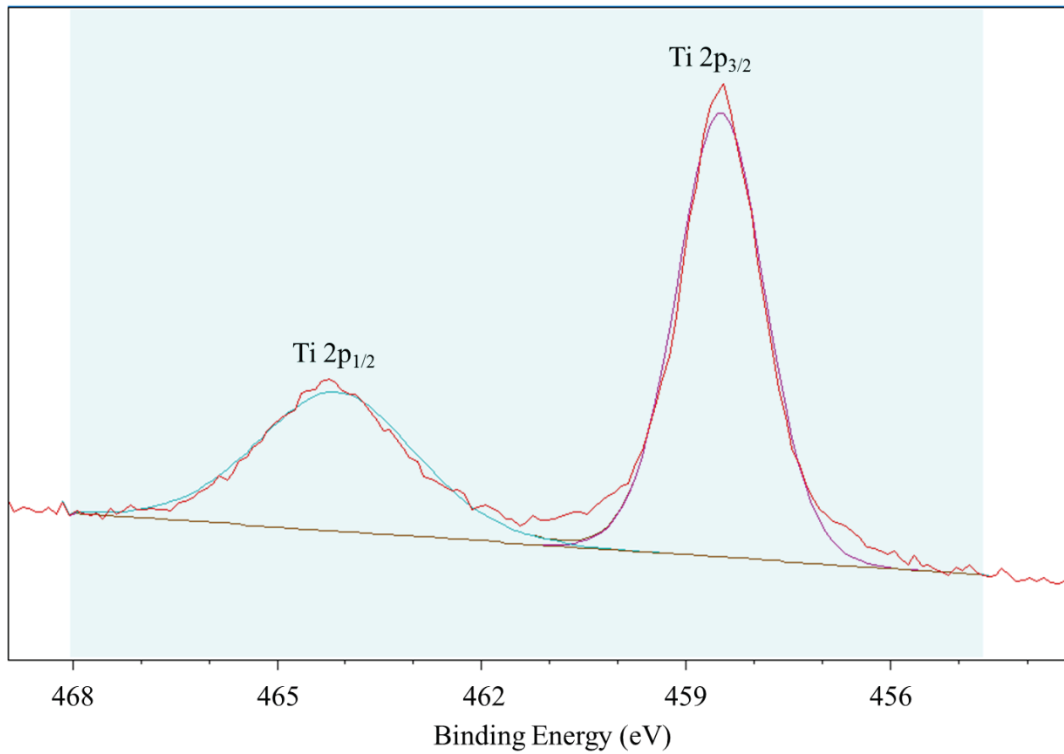

Figure 5.5. High resolution XPS spectrum of the TiO_2 films deposited from $Ti(DMADB)_2$ and water at 350 °C. The Ti 2p peaks, which have been fit to Gaussian line shapes, are centered at 458.5 and 464.2 eV.

CHAPTER 6

ATOMIC LAYER DEPOSITION OF MgO WITH $Mg(DMADB)_2$ AND H_2O

6.1 Introduction

Atomic layer deposition (ALD), makes use of sequential self-terminating surface reactions between two components to afford highly conformal coatings [1-3]. ALD can coat very high AR features, provided that gas dosing is performed long enough for each component to diffuse into and saturate the wall surfaces [2]. In addition, ALD provides digital control of the coating thickness, via the number of dosing cycles, which makes it widely used in the integrated circuit industry [4].

MgO has a wide band-gap (7.8 eV) and high secondary electron yield coefficient; it is widely used as the barrier layer in magnetic tunnel junctions [5,6], and as the wall in plasma devices [7]. Conformal coating of MgO is required in devices with 3-dimensional structures. Previous studies of MgO deposition by ALD have mostly employed β-diketonate or cyclopentadienyl (Cp)- based precursors. The β-diketonate precursor is not very reactive and requires a strong oxidant, like ozone [8] or hydrogen peroxide [9]. With ozone as the co-reactant, the growth exhibits self-limiting behavior at 225-250 °C, and a rate of ~ 0.27 Å/cycle. With H_2O_2, the growth requires a minimum temperature of 300 °C, and growth rate is lower. Partial decomposition of the precursor has been reported, which introduces carbon impurities into the film. By contrast, the $Mg(Cp)_2$ [10] and $Mg(CpEt)_2$ [11] have comparatively high vapor pressure

and will react with a weak oxidant like H_2O; they afford good properties at a substrate temperature of ~ 250 °C. The growth rate per cycle with these two molecules is a little higher than 1.0 Å/cycle.

Here we explore the performance of a new precursor, $Mg(DMADB)_2$, for conformal MgO growth in ALD mode. This precursor affords excellent films by CVD using H2O as a co-reactant at substrate temperatures of 225-500 °C [12]. It has very high vapor pressure, ~ 0.8 Torr at RT (the highest reported for any Mg-bearing molecule) and a clean reaction pathway with water to liberate H(DMADB), a volatile product. We report that $Mg(DMADB)_2$ and H_2O afford MgO films by ALD at the highest rate (~2.2 Å/cycle) of all Mg precursors.

6.2 Experiment

ALD is carried out in a system of UHV construction described in Chapter 1, but with pneumatic valves in place of the manual valves. The ALD dosing cycles are programmed and controlled by a Labview module. However, the chamber was not designed for ALD and does not have a laminar flow pattern. Thus it is not possible to remove residual molecules using an inert gas purge step at relatively high pressure. In place of a purge step, we pump down the chamber for a relatively long time (7-10 min) after each dosing step to eliminate residual molecules. At shorter pumping times, injected precursor and residual water can be simultaneously present, which deposits additional film by unintentional CVD. The substrate is Si (100) wafer with native oxide. The growth temperature ranges from 165–240 °C.

Both $Mg(DMADB)_2$ and H_2O are kept at room temperature in glass containers. The molecules are regulated by needle valves and enter the chamber through separate stainless steel tubes with inner diameter of 0.41 cm. The inlets point towards the chamber wall in order to avoid

line of sight delivery to the substrate; thus the pressures above the substrate are equal to the average partial pressures measured by a capacitance manometer.

Film thickness and growth rate are estimated using in-situ spectroscopic ellipsometry (SE) at a fixed incident angle of 70°, with WVASE32 as the control-analysis software. SE can detect a film thickness change down to ~ 0.01 monolayer [13,14] and has been used to study the ALD growth of Al_2O_3, HfO_2, Er_2O_3, TiO_2, Ta_2O_5, and TaN_x [1,15-22]. The optical model consists of Si substrate and MgO film as the top layer; the thickness of the MgO is the only fitting parameter. According to AFM study, the film roughness is on the level of 0.5 nm, so in the model the roughness layer is not included. The dielectric constant for a 30 nm film is determined from ex-situ variable angle SE using the Cauchy equation, $n(\lambda) = A + B/\lambda^2 + C/\lambda^4$, which is suitable for dielectric materials [23]. The thickness of this film is also determined by cross-sectional SEM. These calibrations enable in-situ SE to determine MgO film thickness within ± 5%. The average growth rate per cycle is calculated from the thickness increment over multiple cycles. However, the optical properties of the adsorbates are unknown and undoubtedly different from those of MgO. Therefore, during the dosing steps, the instantaneous changes in the SE signal do not represent film thickness, but are (admirably) sensitive to the adsorption of precursor and oxidant, and the removal of ligand groups during the reaction. The cycle-to-cycle shift is, however, due to the real MgO thickness. Post-growth analysis is performed using XPS and RBS. Prior to XPS, the sample surface is cleaned by 3 minutes of Ar^+ sputtering.

6.3 Result and Discussion

6.3.1 Growth Kinetics

An ALD sequence at 200 °C consisting of 180 s $Mg(DMADB)_2$ dose, 400 s pumping, 1 s water dose, and 600 s of pumping strongly modulates the SE signal (Fig. 6.1). The sharp increase at the onset of the $Mg(DMADB)_2$ pulse is due to the species adsorbed on the growth surface; the SE signal saturates in the middle of the pulse at 3.6 mTorr, corresponding to saturation coverage. In the pumping phase after the pulse, the optical thickness decreases by ~ 30% due to the slow desorption of the adsorbates. With longer pumping the optical thickness levels off, showing the stable saturated adsorption. This During the water pulse, the precursors' ligands react with water and desorb, the surface becomes covered with hydroxyl groups, and the net optical thickness decreases. For multiple cycles, the optical response is very consistent; the growth rate is ~ 2.2 Å/cycle (Fig. 6.2).

The growth rate per cycle vs. $Mg(DMADB)_2$ pulse length increases linearly up to 20 s, then more slowly, and saturates for doses over ~ 60 s (Fig. 6.3). The $Mg(DMADB)_2$ dose at saturation is ~ 2.2×10^5 L. The growth rate per cycle vs. water pulse length is saturated even at the shortest pulse used, 1 s, corresponding to a dose of ~ 1.2×10^4 L (Fig. 6.4).

The growth rate is very stable at ~ 2.2 Å/cycle in the temperature range 165-240 °C, using the pulse sequence of Fig. 6.1. Above 210 °C the growth rate increases, reaching 5.9 Å/cycle at 240 °C; thus the nominal ALD temperature window is 165-210 °C.

6.3.2 Film Properties

A 40 nm thick MgO film deposited at 200 °C appears very smooth and featureless in cross-sectional SEM (Fig. 6.6), and the rms roughness of 0.9 nm determined by AFM is comparable to that deposited with CVD [12]. XRD θ-2θ measurements (not shown) give no indication of crystallinity. The amorphous structure is consistent with results for CVD deposition using this precursor [12], and with MgO grown by CVD or ALD using other precursors below 400 °C [24-26].

The refractive indices by variable angle SE are slightly lower than those for bulk MgO[27]. The data are consistent with a physical density 90% of the bulk value, calculated using the Bruggmann effective medium approximation [28].

XPS analysis, based on integrated peak intensities and handbook sensitivity factors, indicates an atomic composition of 53% O, 36% Mg, 9% B and 2% Ar due to sputtering (Fig. 6.8). RBS indicates an atomic ratio Mg/O = 69 ± 1% (Fig. 6.9), in excellent agreement with XPS result of 68%. We interpret that B comes from the precursor ligand via one of two routes: (i) the reaction byproduct H(DMADB), which is inefficiently pumped away under our conditions, may have a non-zero rate of dissociation with the film surface; or (ii) high temperature reactions may occur on the hot filament behind the sample holder, and unknown products reach the growth surface. The large fraction of oxygen, and the shift of the B peak position to 193 eV, are consistent with B incorporation as an oxide. We suggest that future work include high-resolution scans of the O and B peak shapes to resolve this point. Better, of course, would be to eliminate B incorporation by efficient pumping after the ALD dosing cycle or by using a hot-wall reactor without hot spots.

6.4 Conclusion

MgO films have been deposited by ALD using the new, high vapor pressure precursor $Mg(DMADB)_2$ with H_2O as the oxidant in the temperature window 165-210 °C. The growth rate per cycle is ~ 2.2 Å, the highest reported among all magnesium containing ALD precursors. The deposited film is amorphous with a very smooth surface. The film density is 90% that of bulk MgO, and contains ~ 9 at. % B as an impurity, likely in the form of oxide. This B may result from incorporation of a by-product species. We anticipate that a standard hot-wall ALD system with laminar flow of purge gas would reduce or eliminate the B contamination.

6.5 References

1. R. L. Puurunen, "Surface chemistry of atomic layer deposition: A case study for the trimethylaluminum/water process", *J. Appl. Phys.* **97** (2005).

2. S. M. George, "Atomic layer deposition: an overview", *Chem. Rev.* **110,** 111-31 (2010).

3. M. Leskela and M. Ritala, "Atomic layer deposition (ALD): from precursors to thin film structures", *Thin Solid Films* **409,** 138-46 (2002).

4. *International Technology Roadmap for Semiconductors* (2009).

5. S. Yuasa, T. Nagahama, A. Fukushima, Y. Suzuki, and K. Ando, "Giant room-temperature magnetoresistance in single-crystal Fe/MgO/Fe magnetic tunnel junctions", *Nature Materials* **3,** 868-71 (2004).

6. K.-R. Jeon, B.-C. Min, S.-Y. Park, K.-D. Lee, H.-S. Song, Y.-H. Park, Y.-H. Jo, and S.-C. Shin, "Thermal spin injection and accumulation in CoFe/MgO/n-type Ge contacts", *Scientific Reports* **2** (2012).

7. K. S. Nam, H. J. Lee, S. H. Lee, G. H. Lee, Y. S. Song, and D. Y. Lee, "The effect of an atmospheric pressure plasma treated MgO layer on the discharge performance of an AC plasma display panel", *Surface & Coatings Technology* **201,** 2567-72 (2006).

8. T. Hatanpaa, J. Ihanus, J. Kansikas, I. Mutikainen, M. Ritala, and M. Leskela, "Properties of $Mg_2(thd)_4$ as a precursor for atomic layer deposition of MgO thin films and crystal structures of $Mg_2(thd)_4$ and $Mg(thd)_2(EtOH)_2$", *Chem. Mat.* **11,** 1846-52 (1999).

9. M. Putkonen, L. S. Johansson, E. Rauhala, and L. Niinisto, "Surface-controlled growth of magnesium oxide thin films by atomic layer epitaxy", *J. Mater. Chem.* **9,** 2449-52 (1999).

10. M. Putkonen, T. Sajavaara, and L. Niinisto, "Enhanced growth rate in atomic layer epitaxy deposition of magnesium oxide thin films", *J. Mater. Chem.* **10,** 1857-61 (2000).

11. B. B. Burton, D. N. Goldstein, and S. M. George, "Atomic layer deposition of MgO using bis(ethylcyclopentadienyl)magnesium and H_2O", *Journal of Physical Chemistry C* **113,** 1939-46 (2009).

12. W. B. Wang, Y. Yang, A. Yanguas-Gil, N. N. Chang, G. S. Girolami, and J. R. Abelson, "Highly conformal magnesium oxide thin films by low-temperature chemical vapor deposition from $Mg(H_3BNMe_2BH_3)_2$ and water", *Applied Physics Letters* **102** (2013).

13. E. A. Irene, H. G. Tompkins, *Handbook of Ellipsometry* (William Andrew Publishing, New York, 2005).

14. K. Vedam, "Spectroscopic ellipsometry: a historical overview", *Thin Solid Films* **313,** 1-9 (1998).

15. E. Langereis, S. B. S. Heil, H. C. M. Knoops, W. Keuning, M. C. M. van de Sanden, and W. M. M. Kessels, "In situ spectroscopic ellipsometry as a versatile tool for studying atomic layer deposition", *Journal of Physics D-Applied Physics* **42** (2009).

16. E. Langereis, H. C. M. Knoops, A. J. M. Mackus, F. Roozeboom, M. C. M. van de Sanden, and W. M. M. Kessels, "Synthesis and in situ characterization of low-resistivity TaNx films by remote plasma atomic layer deposition", *J. Appl. Phys.* **102** (2007).

17. O. Buiu, Y. Lu, I. Z. Mitrovic, S. Hall, P. Chalker, and R. J. Potter, "Spectroellipsometric assessment of HfO_2 thin films", *Thin Solid Films* **515,** 623-6 (2006).

18. S. B. S. Heil, F. Roozeboom, M. C. M. van de Sanden, and W. M. M. Kessels, "Plasma-assisted atomic layer deposition of Ta_2O_5 from alkylamide precursor and remote O_2 plasma", *Journal of Vacuum Science & Technology A* **26,** 472-80 (2008).

19. S. B. S. Heil, E. Langereis, F. Roozeboom, M. C. M. van de Sanden, and W. M. M. Kessels, "Low-temperature deposition of TiN by plasma-assisted atomic layer deposition", *Journal of the Electrochemical Society* **153,** G956-G65 (2006).

20. J. W. Klaus, A. W. Ott, J. M. Johnson, and S. M. George, "Atomic layer controlled growth of SiO_2 films using binary reaction sequence chemistry", *Applied Physics Letters* **70,** 1092-4 (1997).

21. E. Langereis, S. B. S. Heil, M. C. M. van de Sanden, and W. M. M. Kessels, "Initial growth and properties of atomic layer deposited TiN films studied by in situ spectroscopic ellipsometry," in *Physica Status Solidi C - Conferences and Critical Reviews, Vol 2 , No 12*; *Vol. 2*, edited by M. Stutzmann (2005), p. 3958-62.

22. E. Langereis, S. B. S. Heil, M. C. M. van de Sanden, and W. M. M. Kessels, "In situ spectroscopic ellipsometry study on the growth of ultrathin TiN films by plasma-assisted atomic layer deposition", *J. Appl. Phys.* **100** (2006).

23. F. A. Jenkins, H. E. White, *Fundamentals of Optics*, 3 ed. (McGraw-Hill, Inc., New York, 1957).

24. L. Wang, Y. Yang, J. Ni, C. L. Stern, and T. J. Marks, "Synthesis and characterization of low-melting, highly volatile magnesium MOCVD precursors and their implementation in MgO thin film growth", *Chem. Mat.* **17,** 5697-704 (2005).

25. M. M. Sung, C. G. Kim, J. Kim, and Y. Kim, "Chemical beam deposition of MgO films on Si substrates using methylmagnesium tert-butoxide", *Chem. Mat.* **14,** 826-31 (2002).

26. J. G. Yoon, H. K. Oh, and S. J. Lee, "Growth characteristics and surface roughening of vapor-deposited MgO thin films", *Physical Review B* **60,** 2839-43 (1999).

27. E. D. Palik, *Handbook of Optical Constants of Solids*, 2 ed. (Academic Press, Boston, 1991).

28. D. E. Aspnes, "Local-field effects and effective-medium theory - a microscopic perspective", *American Journal of Physics* **50,** 704-9 (1982).

6.6 Figures

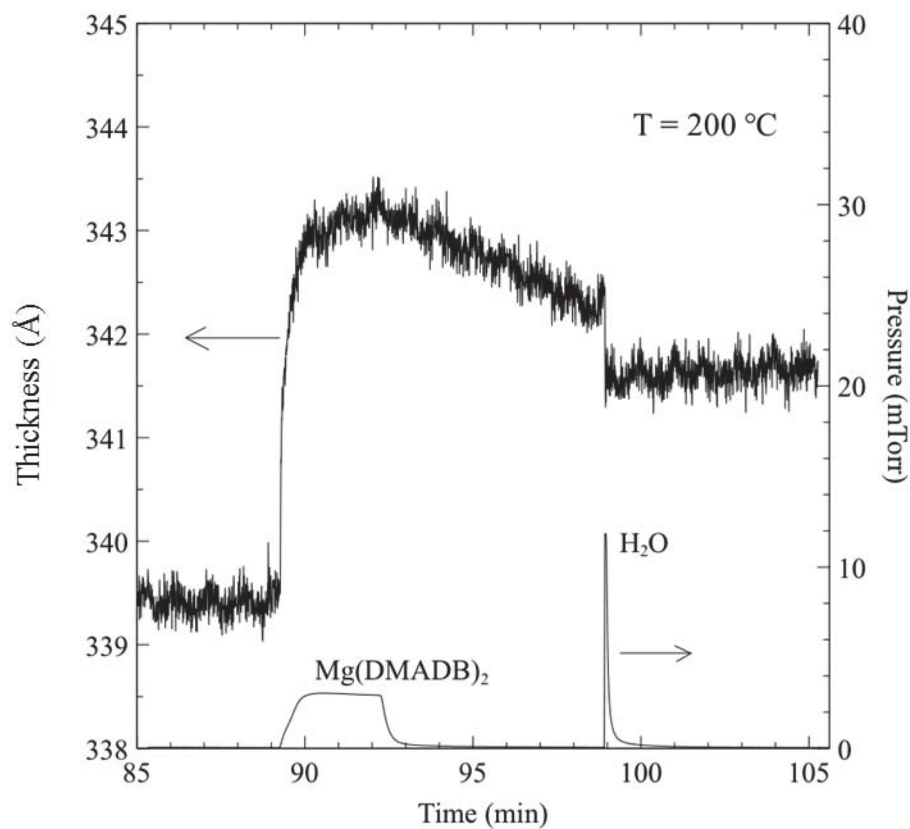

Figure 6.1. Thickness change according to Spectroscopic Ellipsometry, during one MgO ALD cycle at 200°C. Below is the corresponding chamber pressure during each of the dosing and pumping steps. The timing sequence is 180 s $Mg(DMADB)_2$ dose, 400 s pumping, 1 s water dose, and 600 s of pumping.

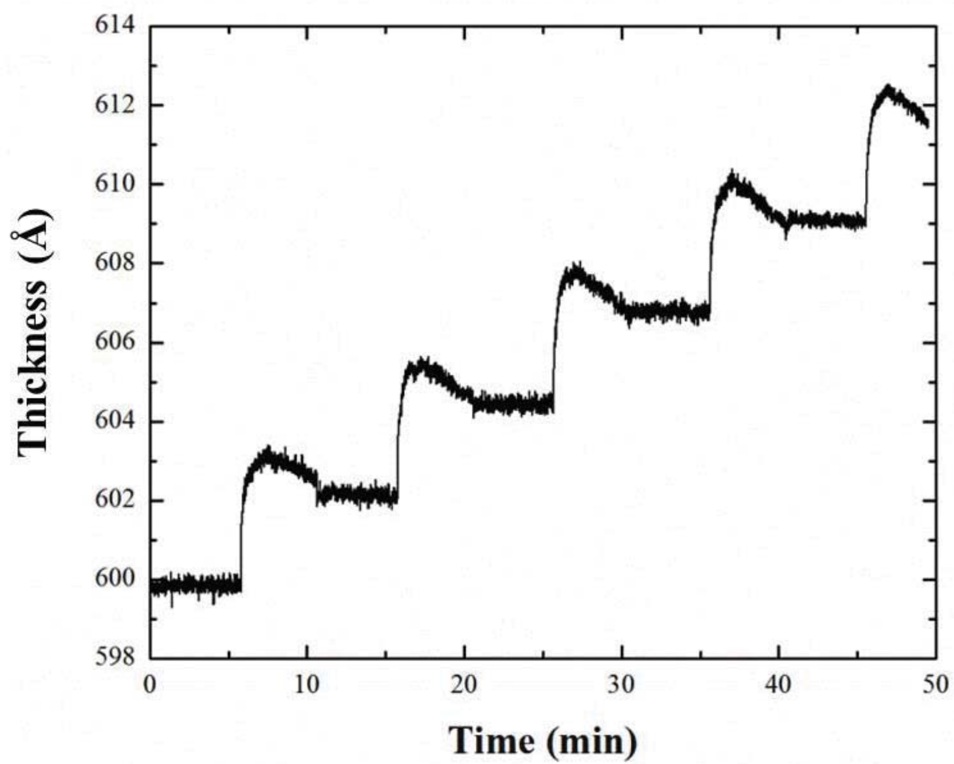

Figure 6.2. The fitted thickness change from in-situ Spectroscopic Ellipsometry for multiple MgO ALD cycles at 200 °C.

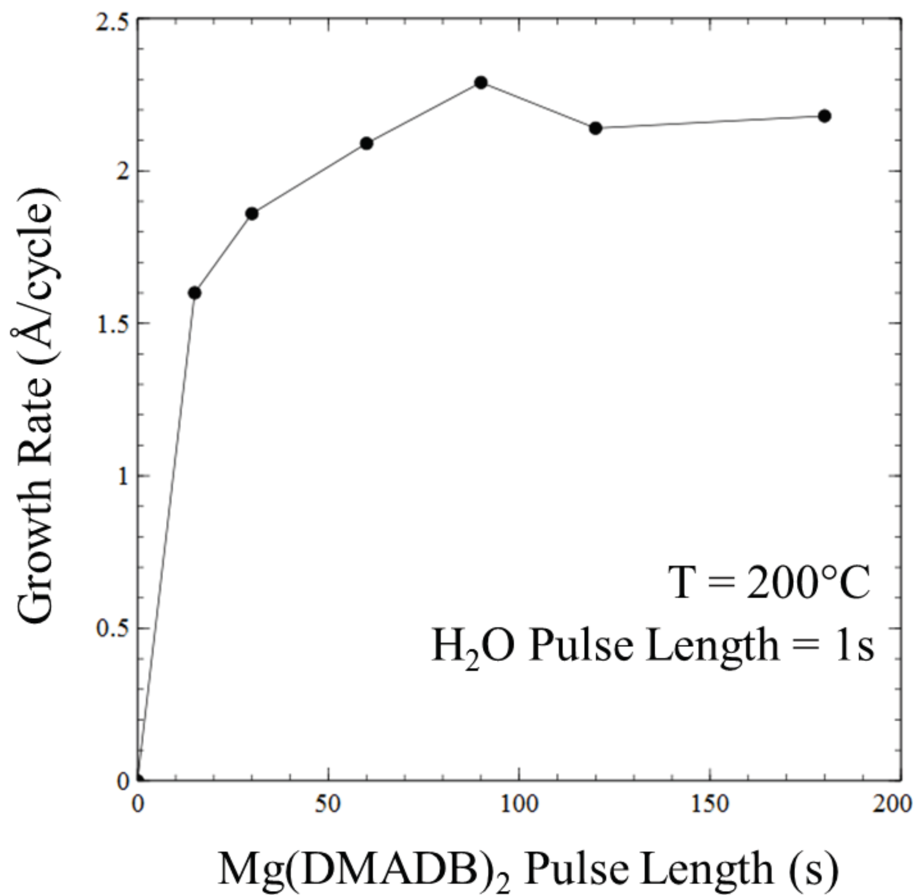

Figure 6.3. The saturation curve for Mg(DMADB)$_2$ with a time sequence of Mg(DMADB)$_2$ x seconds – pumping 400 seconds – water 1 second – pumping 600 seconds, showing the saturated growth rate at 200 °C is about 2.2 Å/cycle.

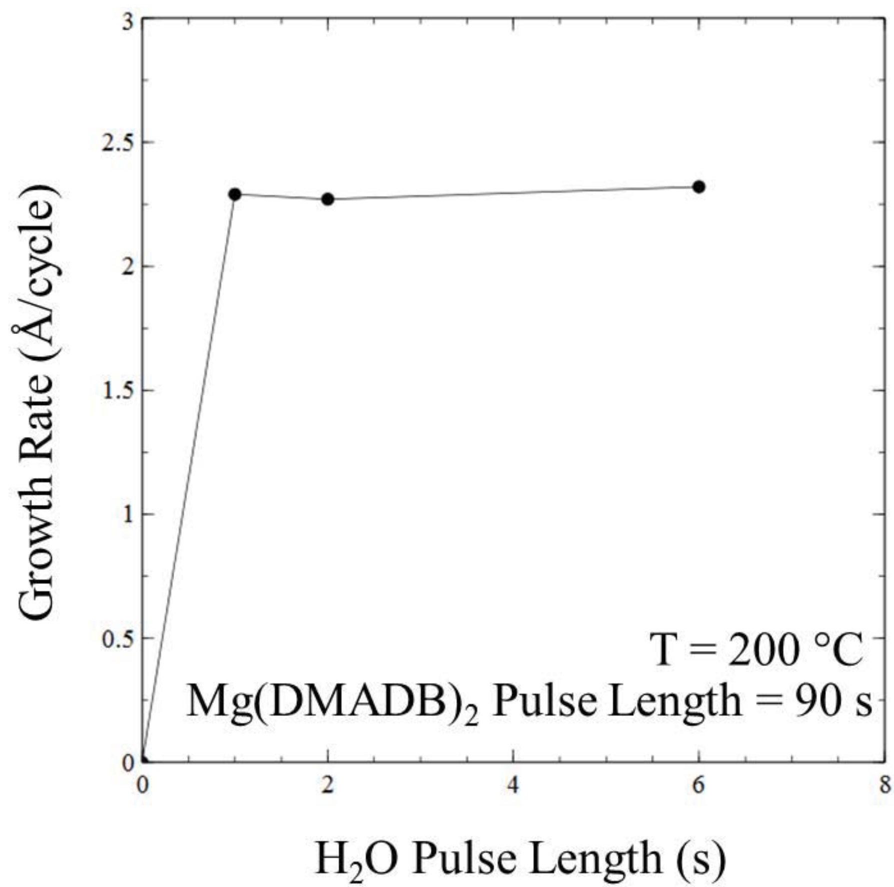

Figure 6.4. At 200 °C, growth rate does not change with varying water pulse length, indicating that water pulse of 1 s is sufficient for saturation.

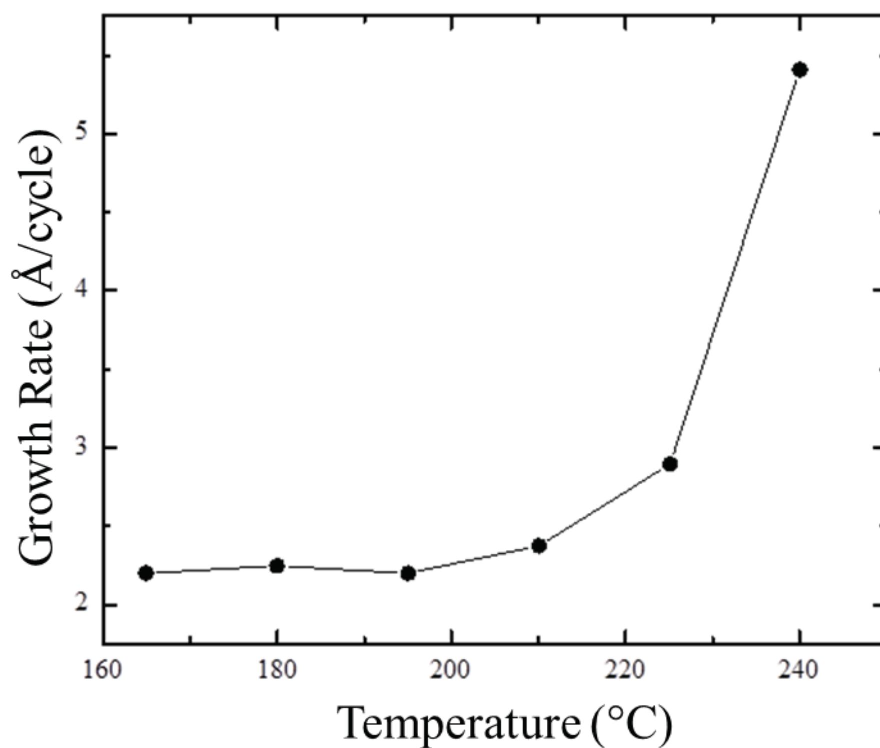

Figure 6.5. Saturation growth rate for Mg(DMADB)$_2$ + H_2O ALD process as a function of substrate temperature, with the ALD cycle composed of Mg(DMADB)$_2$ dosing of 180 s followed by 400 s pumping and 1 s H_2O dosing and 600 s pumping. The growth rate within the temperature window 165-210 °C stabilizes at ~ 2.2Å/cycle.

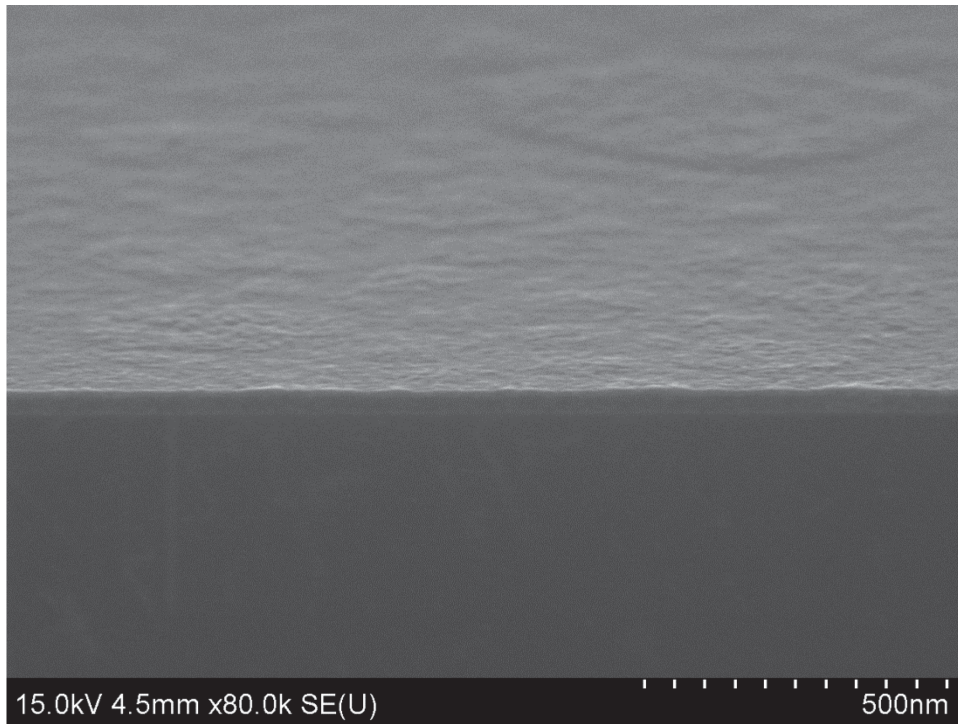

Figure 6.6. Cross-section SEM image for MgO film on Si substrate.

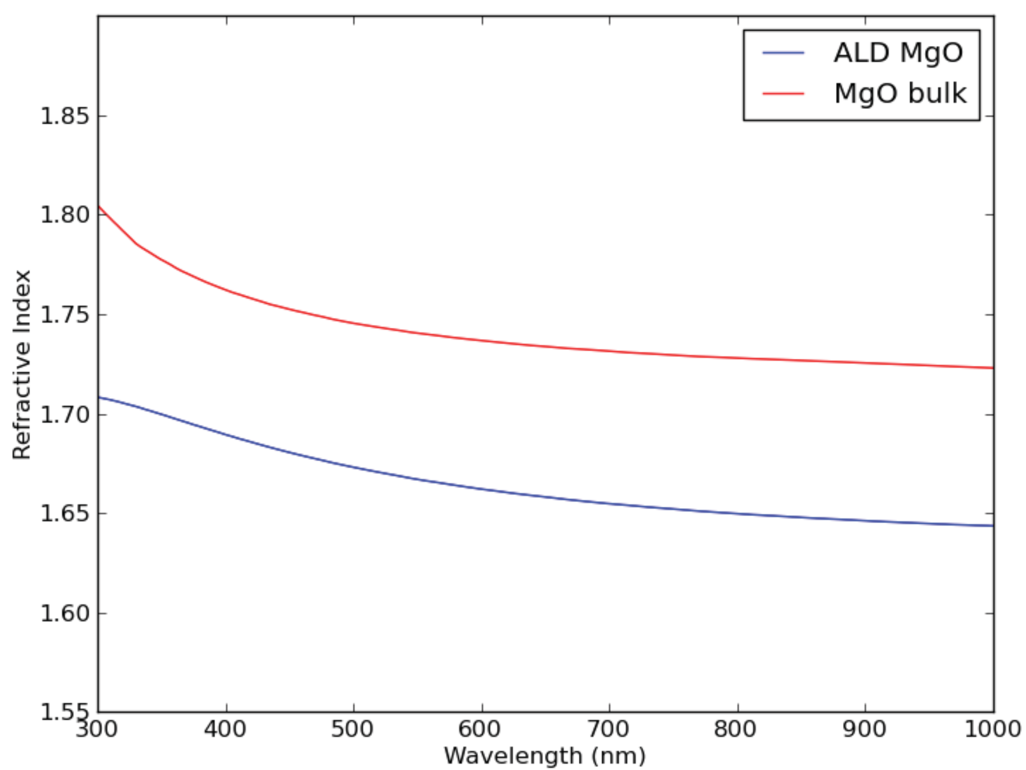

Figure 6.7. Refractive indices for the MgO film deposited with ALD method. For comparison, the refractive indices for bulk MgO is also shown.

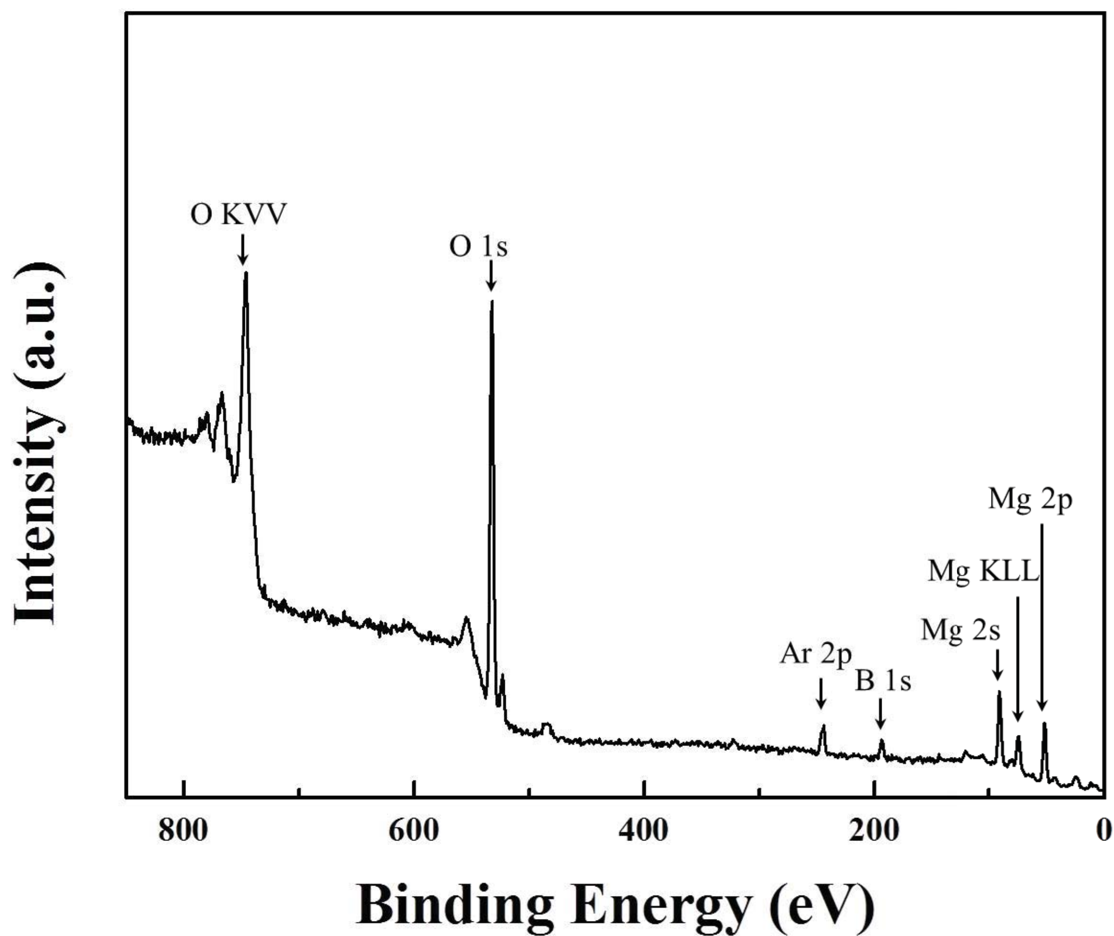

Figure 6.8. XPS spectrum for ALD MgO sample after 2 minutes of sputtering, with all major peaks labeled. Based on the integrated area covered by each peak, and the relative sensitivity factors, the composition of the film is found to be O 52.8%, Mg 35.6%, B 9.3%, and Ar 2.3%.

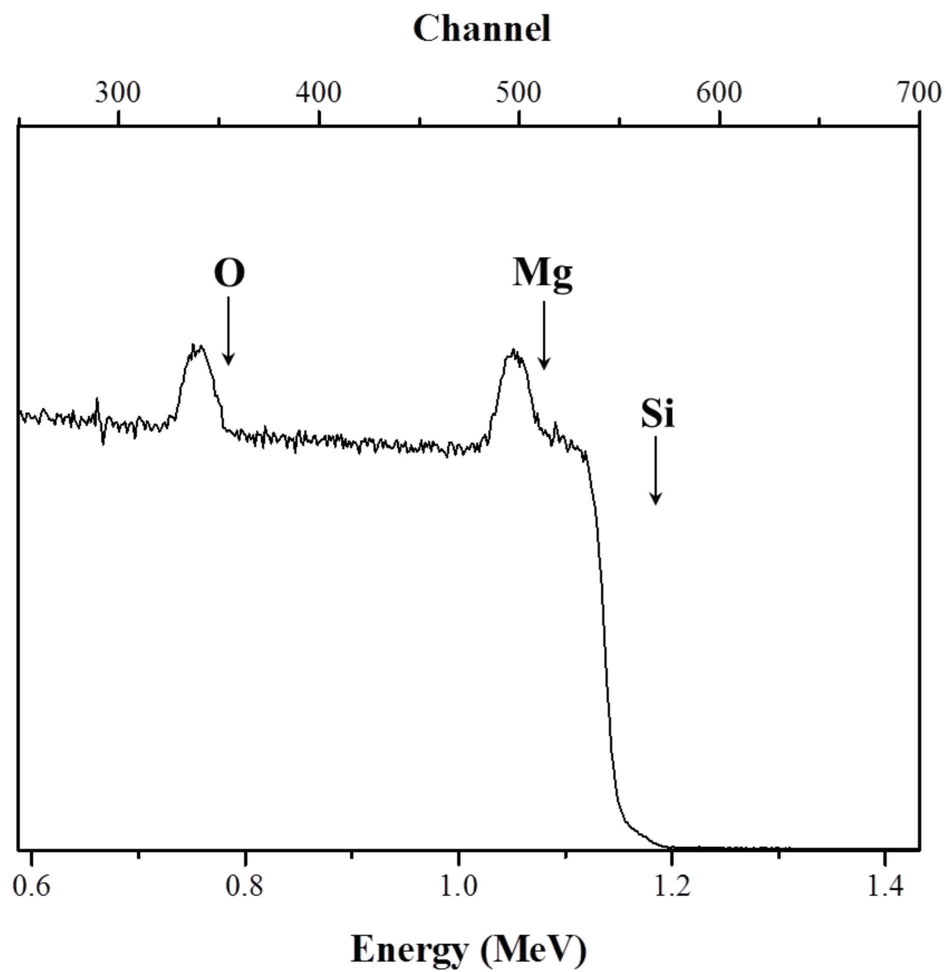

Figure 6.9. RBS spectrum for ALD MgO film; arrows indicate the surface energy position for each element. The integrated peak areas correspond to an atomic composition ratio Mg/O = 69 ± 1%.